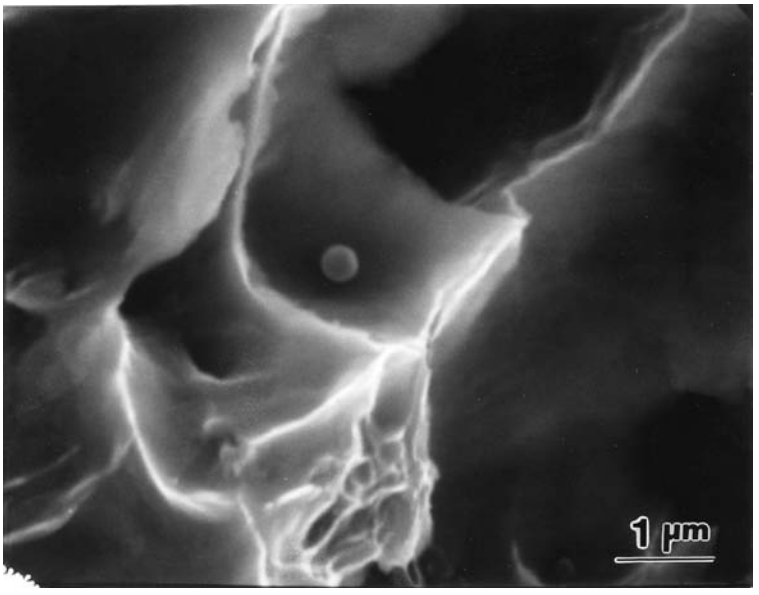

Fig. 8.12 Scanning electron micrograph of dimple fracture resulting from the nucleation, growth, and coalescence of microcavities. The micrograph shows an inclusion, which served as the microcavity nucleation site.

essentially tensile, with the surface perpendicular to the tensile axis. On the sides, the fracture has a strong shear character, and the dimples show the typical "inclined" morphology, i.e., they appear to be elliptical with one side missing. Figure 8.14 shows, in a very schematic fashion, what is thought to occur in the specimen that leads to failure. Voids nucleate and grow in the interior of the specimen when the overall plastic strain reaches a critical level. The voids grow until they coalesce. Initially equiaxial, their shape changes in accordance with the overall stress field. As the voids coalesce, they expand into adjoining areas, due to the stress concentration effect. When the center of the specimen is essentially separated, this failure will grow toward the outside. Since the elastic–plastic constraints change, the plane of maximum shear (approximately 45° to the tensile axis) is favored, and further growth will take place along these planes, which form the sides of the cup. Although it is easy to describe this process in a qualitative way, an analytical derivation is very complex and involves plasticity theory, which is beyond the scope of the text. Figure 8.15 shows the sequence of ductile fracture propagation, with the formation of dimples. The dimples are produced by voids nucleating ahead of the principal crack (Figures 8.15(a) and (b)), which has a blunted tip because of the plasticity of the material. The void ahead of the crack grows (Figure 8.15(c)) and eventually coalesces with the main crack (Figure 8.15(d)). New voids nucleate ahead of the growing crack, and the process repeats itself. Figure 8.16 shows the propagation of ductile fracture in a specimen of AISI 304 stainless steel undergoing extension, as seen in a high-voltage transmission electron microscope. A referential fixed to the material was added to help visualize the progression of the crack. Figure 8.16(a) shows the growth of a void ahead of the tip of the crack, while Figure 8.16(b) shows new voids

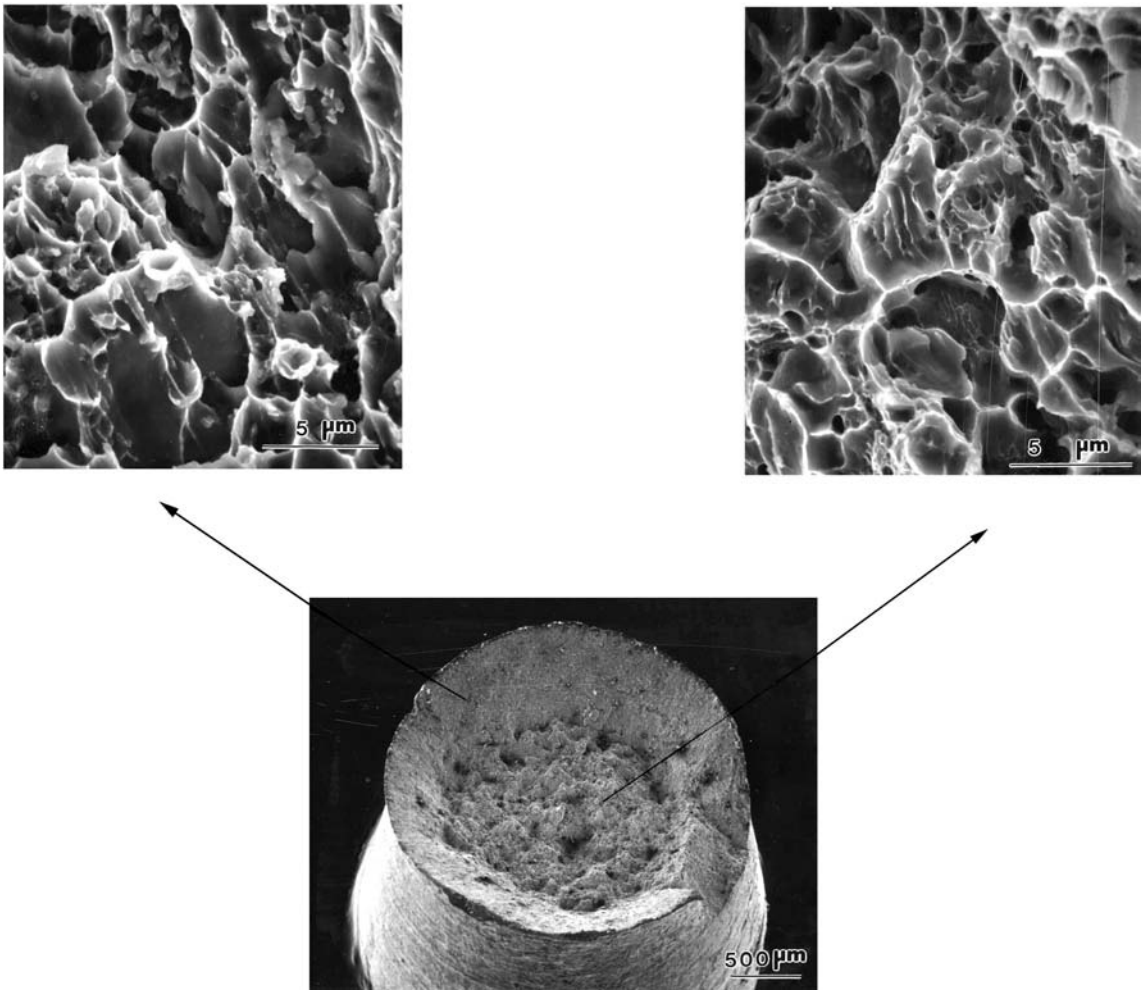

Fig. 8.13 Scanning electron micrographs at low magnification (center) and high magnification (right and left) of AISI 1008 steel specimen ruptured in tension. Notice the equiaxal dimples in the central region and elongated dimples on the shear walls, the sides of the cup.

being nucleated. In Figure 8.16(c), the crack has advanced by joining with these growing voids. New voids have nucleated.

The nucleation and growth of voids is of great importance in determining the fracture characteristics of ductile materials. Many researchers have identified second-phase particles and inclusions as the main sources of voids.[2] Indeed, Figure 8.12 shows dimples, at the bottoms of which second-phase particles can be seen. The size, separation, and interfacial bonding of these particles determine the overall propagation characteristics of ductile cracks and, therefore, the ductility of the material. The role of second-phase particles is illustrated in Figure 8.17. Copper-based alloys with different amounts of second-phase particles (fractions from 0 to 0.24) were tested in tension, and

[2] See, for example, H. C. Rogers, in *Ductility* (Metals Park, OH: ASM, 1967), p. 31; and L. M. Brown and J. D. Embury, in *Microstructure in Design of Alloys*, Vol. 1 (London: Institute of Metals/Iron and Steel Institute, 1973), p. 164.

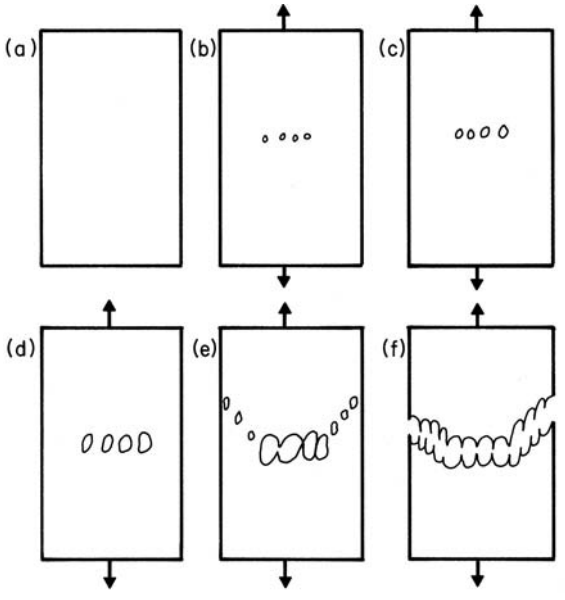

Fig. 8.14 Schematic sequence of events leading to the formation of a cup-and-cone fracture.

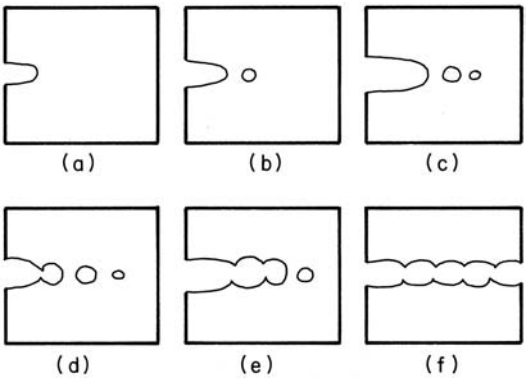

Fig. 8.15 Sequence of events in the propagation of ductile fracture by nucleation, growth, and coalescence of voids.

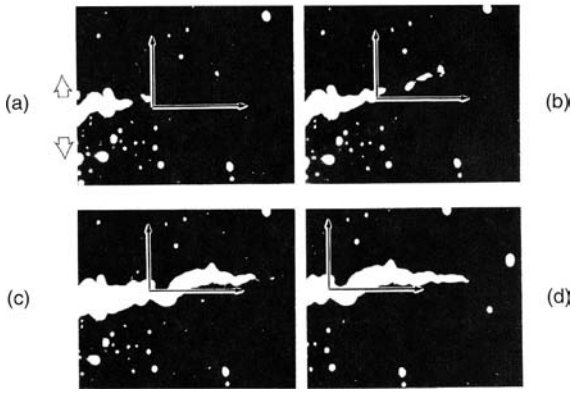

Fig. 8.16 Observation of progression of ductile fracture while specimen is stressed in high-voltage transmission electron microscope. Referential is fixed to material. (Courtesy of L. E. Murr.)

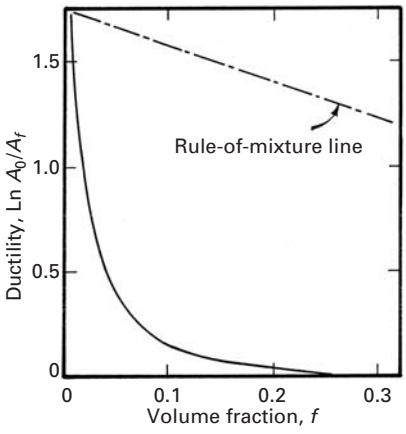

Fig. 8.17 Combined plot of ductility vs. volume fraction of second phase, f, for copper specimens containing various second phases and for notched copper specimens. The dashed line represents the prediction from the law of mixtures, assuming zero ductility for the second-phase particles. (From B. I. Edelson and W. J. Baldwin, Jr., *Trans. ASM*, 55 (1962) 230.)

the ductility of the material was measured. The ductility is given by the reduction in area of the specimens at the fracture point (ln A_0/A_f, where A_0 and A_f are the initial and final cross-sectional areas, respectively). By a simple rule of mixtures, assuming that the second-place particles have zero ductility, one obtains the straight line shown in the figure. However, the effect of second-phase particles is much more drastic, and ductility is reduced to zero at $f = 0.24$. This is a clear indication that second-phase particles play a key role in the propagation of ductile fracture.

Various models have been proposed for void growth. When the growth rate is very low, or the temperature is high (such as in creep) vacancies flow into the void and make it grow. However, at low temperatures and higher strain rates the migration of vacancies cannot account for void growth. A mechanism involving dislocations needs to be considered. In Chapter 4 (Figure 4.26) we studied prismatic loops. These loops consist of a disk of atoms. We assume, for simplicity, a two-dimensional situation shown in Figure 8.18(a). If a prismatic loop moves by glide of the dislocations, the extra disk of matter is carried away and the void diameter increases by b, equal to the Burgers vector. Figure 8.18(a) shows four prismatic loops originating at the void surface and moving out.

It can be shown that the shear stresses at 45° to the surface of a void are maximum. Assuming elastic stresses and if the remote stresses are hydrostatic, the tangential stress at the void surface is:

$$\sigma_\theta = 3\sigma.$$

The radial stress is equal to zero, since normal stresses at a free surface are equal to the external tractions:

$$\sigma_r = 0.$$

The maximum shear stress bisects these two stresses and is therefore at 45°. Its magnitude is:

$$\tau_{\max} = \frac{\sigma_\theta - \sigma_r}{2} = 1.5\sigma.$$

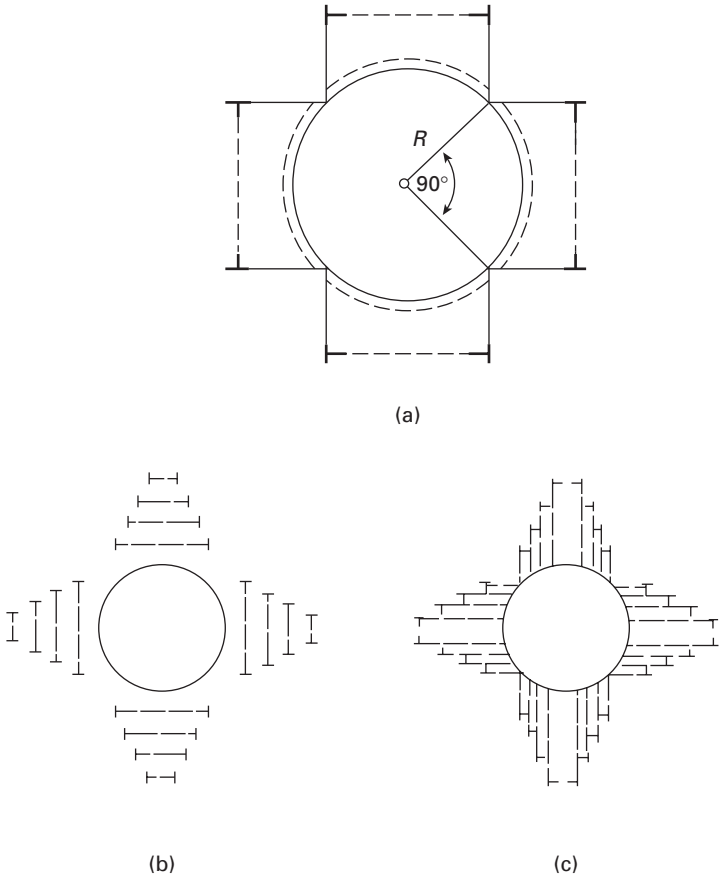

Fig. 8.18 (a) Schematic showing how the emission of four loops starting at 45° to void surface increases void diameter by Burgers vector *b*. Network of (b) prismatic loops and (c) shear loops (dislocation loops) were sequentially emitted from the surface of the growing void and move into the material. (From V. A. Lubarda, M. S. Schneider, D. H. Kalantar, B. R. Remington, and M. A. Meyers, *Acta Mater*. 52 (2004) 1397.)

When this shear stress reaches a critical level, a dislocation can be emitted from the void. Two mechanisms accounting for the generation of the geometrically-necessary dislocations required for void growth are shown in Figure 8.18(b) and (c). Figure 8.18(b) shows successive prismatic loops emitted from a growing void. As the void grows, so does the diameter of the loops. This is a two-dimensional representation, and a full three-dimensional picture would be more complex. Figure 8.18(c) shows shear loops, that can also accomplish the same goal of removing matter from the void surface and extending it. The actual growth of voids is more complex, since the loops interact with each other and their outward motion is therefore impeded. Nevertheless, the net result is that a large density of dislocations is generated around a growing void. Indeed, transmission electron microscopy reveals that voids are surrounded by a highly work-hardened layer.

Before we close this section, it is worth pointing out here that the term "ductility" signifies a material's capacity to undergo plastic deformation. Ductility is not a fundamental property of the material, because the plastic strain before fracture is a function of the state of stress, strain rate, temperature, environment, and prior history of the material. The state of stress is defined by the three-dimensional

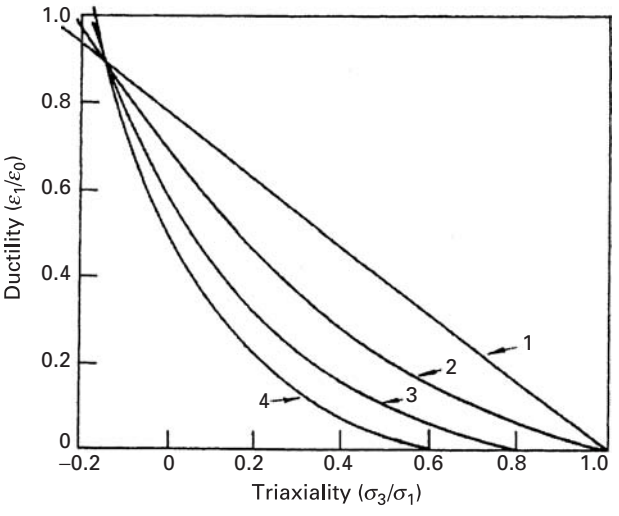

Fig. 8.19 Variation of maximum plastic strain (ductility) with the degree of triaxiality, according to (1) theory of maximum tensile stress failure, (2) plane-strain conditions, (3) von Mises criterion, and (4) power law of plastic strain. (Adapted with permission from M. J. Manjoine, in *Fracture: An Advanced Treatise*, Vol. 3, H. Liebowitz, ed. (New York: Academic Press, 1971), p. 265.)

distribution of normal and shear stresses at a point or by the three principal stresses at a point. (See Chapter 2.) The multiaxial stresses may be obtained by external multiaxial loading, by geometry of the structure or microstructure under load, by thermal stresses, or by volumetric microstructural changes. One can define a simple "triaxiality" factor by the ratio σ_3/σ_1, where $\sigma_1 > \sigma_2 > \sigma_3$ are the principal stresses. If ε_0 is the plastic strain at fracture in uniaxial tension and ε_1 is the maximum principal plastic strain, one can define a ductility ratio as $\varepsilon_1/\varepsilon_0$. This ductility ratio shows, theoretically, a decrease with increasing triaxiality; that is, $\varepsilon_1/\varepsilon_0$ goes to zero as σ_3/σ_1 goes to unity (Figure 8.19). Thus, an increase in the degree of stress triaxiality results in a decrease in the ductility of the material.

The temperature and the strain rate have contrary effects. A high temperature (or a low strain rate) leads to high ductility, whereas a low temperature (or a high strain rate) leads to low ductility.

8.2.3 Brittle, or Cleavage, Fracture

The most brittle form of fracture is cleavage fracture. The tendency for a cleavage fracture increases with an increase in the strain rate or a decrease in the test temperature of a material. This is shown, typically, by a ductile–brittle transition in steel in a Charpy impact test (Figure 8.20). The ductile–brittle transition temperature (DBTT) increases with an increase in the strain rate. Above the DBTT the steel shows a ductile fracture, while below the DBTT it shows a brittle fracture. The ductile fracture needs a lot more energy than the brittle fracture. We deal with these aspects of DBTT in more detail in Chapter 9.

Cleavage occurs by direct separation along specific crystallographic planes by means of a simple rupturing of atomic bonds (Figure 8.21(a)). Iron, for example, undergoes cleavage along its cubic planes (100). This gives the characteristic flat surface appearance

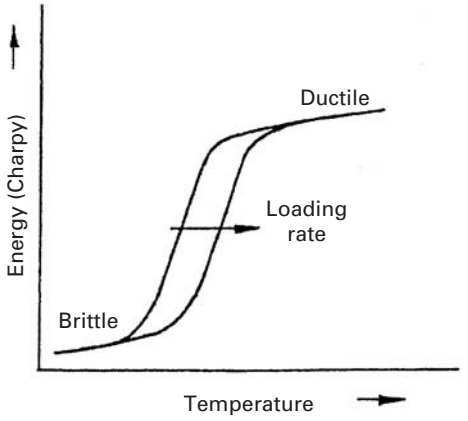

Fig. 8.20 Ductile–brittle transition in steel and the effect of loading rate (schematic).

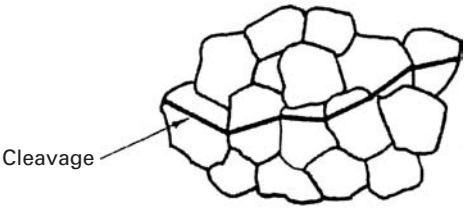

(a)

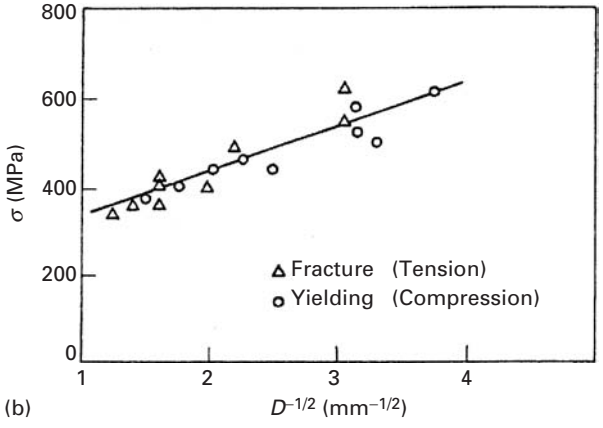

(b)

Fig. 8.21 (a) Propagation of transgranular cleavage. (b) Effect of grain size on fracture and yield stress of a carbon steel at 77 K. (Adapted from J. R. Low, in *Madrid Colloquium on Deformation and Flow of Solids* (Berlin: Springer-Verlag, 1956), p. 60.)

within a grain on the fracture surface. There is evidence that some kind of plastic yielding and dislocation interaction is responsible for cleavage fracture. Low studied the fracture behavior of a low-carbon steel at 77 K, comparing the yield stress in compression (in which case fracture does not occur) with the stress for cleavage in tension. He did this for a number of samples with different grain sizes and obtained the plot shown in Figure 8.21(b). The variation in grain size in both cases followed a Hall–Petch type of relationship, which showed that the controlling mechanism in yielding was also the controlling mechanism for initiating fractures. At 77 K, yielding is closely associated with mechanical twinning. (See Section 5.3.)

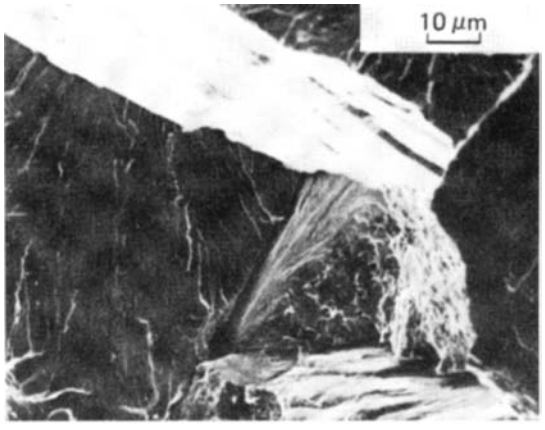

(a)

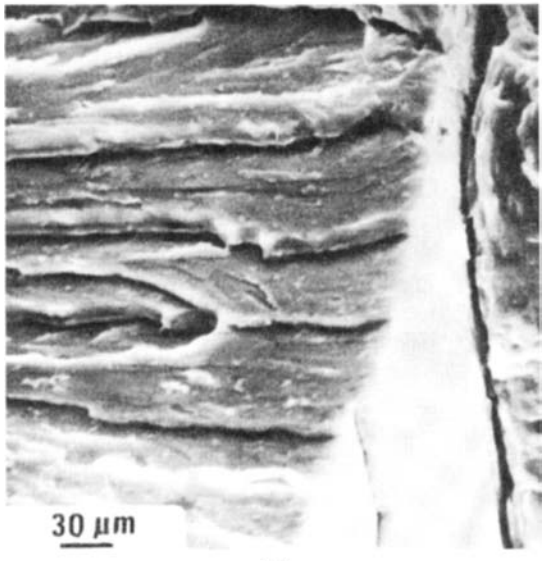

(b)

Fig. 8.22 (a) Cleavage facets in 300-M steel (scanning electron micrograph). (b) River markings on a cleavage facet in 300-M steel (scanning electron micrograph).

Earlier, we mentioned that cleavage occurs along specific crystallographic planes. As in a polycrystalline material, the adjacent grains have different orientations; the cleavage crack changes direction at the grain boundary in order to continue along the given crystallographic planes. The cleavage facets seen through the grains have a high reflectivity, which gives the fracture surface a shiny appearance (Figure 8.22(a)). Sometimes the cleavage fracture surface shows some small irregularities – for example, the river markings in Figure 8.22(b). What happens is that, within a grain, cracks may grow simultaneously on two parallel crystallographic planes (Figure 8.23(a)). The two parallel cracks can then join together, by secondary cleavage or by shear, to form a step. Cleavage steps can be initiated by the passage of a screw dislocation, as shown in Figure 8.23(b). In general, the

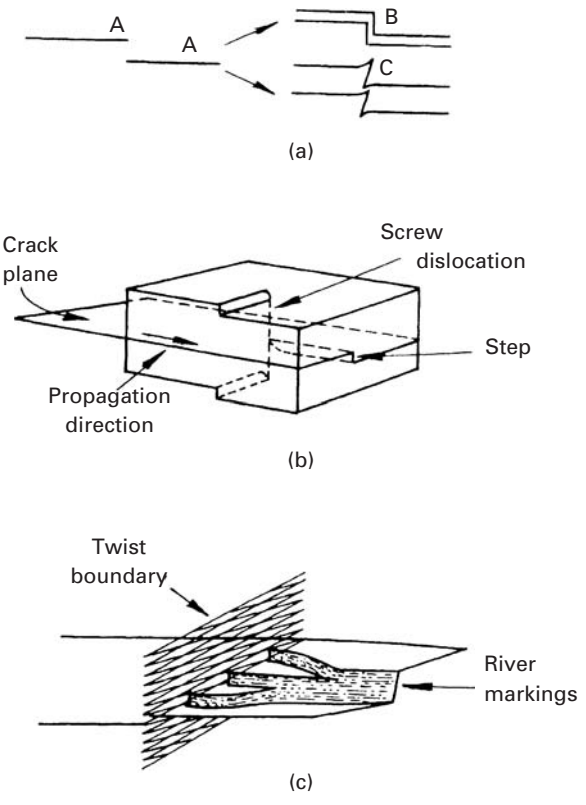

Fig. 8.23 Formation of cleavage steps. (a) Parallel cracks (*A, A*) join together by cleavage (*B*) or shear (*C*). (b) Cleavage step initiation by the passage of a screw dislocation. (c) Formation of river markings after the passage of a grain boundary. (Adapted from D. Broek, *Elementary Engineering Fracture Mechanics*, 3rd ed. (The Hague, Netherlands: Martinus Nijhoff, 1982), p. 33.)

cleavage step will be parallel to the crack's direction of propagation and perpendicular to the plane containing the crack, as this configuration would minimize the energy for the step formation by creating a minimum of additional surface. A large number of cleavage steps can join and form a multiple step. On the other hand, steps of opposite signs can join and disappear. The junction of cleavage steps results in a figure of a river and its tributaries. River markings can appear by the passage of a grain boundary, as shown in Figure 8.23(c). We know that cleavage crack tends to propagate along a specific crystallographic plane. This being so, when a crack passes through a grain boundary, it has to propagate in a grain with a different orientation. Figure 8.23(c) shows the encounter of a cleavage crack with a grain boundary. After they meet, the crack should propagate on a cleavage plane that is oriented in a different manner. The crack can do this at various points and spread into the new grain. Such a process gives rise to the formation of a number of steps that can group together, generating a river marking (Figure 8.23(c). The convergence of tributaries is always in the direction of flow of the river (i.e., "downstream"). This fact furnishes the possibility of determining the local direction of propagation of crack in a micrograph.

Under normal circumstances, face-centered cubic (FCC) metals do not show cleavage. In these metals, a large amount of plastic

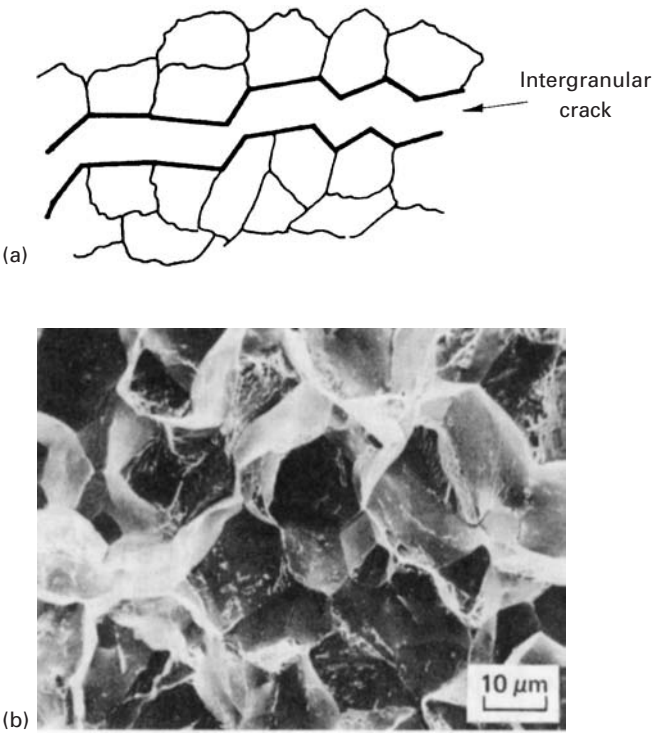

Fig. 8.24 (a) An intergranular fracture (schematic). (b) Intergranular fracture in steel (scanning electron micrograph).

deformation will occur before the stress necessary for cleavage is reached. Cleavage is common in body-centered cubic (BCC) and hexagonal close-packed (HCP) structures, particularly in iron and low-carbon steels (BCC). Tungsten, molybdenum, and chromium (all BCC) and zinc, beryllium, and magnesium (all HCP) are other examples of metals that commonly show cleavage.

Quasi cleavage is a type of fracture that is formed when cleavage occurs on a very fine scale and on cleavage planes that are not very well defined. Typically, one sees this type of fracture in quenched and tempered steels. These steels contain tempered martensite and a network of carbide particles whose size and distribution can lead to a poor definition of cleavage planes in the austenite grain. Thus, the real cleavage planes are exchanged for small and ill-defined cleavage facets that initiate at the carbide particles. Such small facets can give the appearance of a much more ductile fracture than that of normal cleavage, and generally, river markings are not observed.

Intergranular fracture is a low-energy fracture mode. The crack follows the grain boundaries, as shown schematically in Figure 8.24(a), giving the fracture a bright and reflective appearance on a macroscopic scale. On a microscopic scale, the crack may deviate around a particle and make some microcavities locally. Figure 8.24(b) shows an example of this deviation in a micrograph of an intergranular fracture in steel. Intergranular fractures tend to occur when the grain boundaries are more brittle than the crystal lattice. This occurs, for example, in stainless steel when it is accidentally sensitized. This

accident in the heat treatment produces a film of brittle carbides along the grain boundaries. The film is then the preferred trajectory of the crack tip. The segregation of phosphorus or sulfur to grain boundaries can also lead to intergranular fracture. In many cases, fracture at high temperatures and in creep tends to be intergranular.

The ductile–brittle transition temperature of steels and other BCC metals and alloys is significantly affected by grain size. Failure by cleavage (or quasi-brittle crack propagation) and by ductile means are competing mechanisms. When cleavage cracks form and propagate at a greater rate than plastic deformation, the material fails in a brittle manner. It is well known that a reduction in grain size causes a reduction in the ductile-to-brittle transition temperature in steels. Indeed, a reduction in grain size is a very effective means of producing steels that are ductile at low temperature. The explanation of this effect is known as the *Armstrong* criterion[3] and is discussed briefly next.

The yield stress is well represented by the Hall–Petch Equation (see Section 5.4), namely,

$$\sigma_y = \sigma_0 + k_y D^{-1/2}.$$

The temperature effect can be expressed by

$$\sigma_0 = B \exp(-\beta T),$$

where B and β are thermal softening parameters. As T increases, σ_0 decreases. The cleavage stress, on the other hand, is also represented by a Hall–Petch relationship:

$$\sigma_c = \sigma_{0c} + k_c D^{-1/2}.$$

Note that σ_c is not dependent on temperature. Note also that $k_c > k_y$.[4] By setting σ_c equal to σ_y, we can obtain the ductile-to-brittle transition temperature:

$$\sigma_y = \sigma_c,$$
$$T_c = \frac{1}{\beta}[\ln B - \ln\{(k_c - k_y) + \sigma_{0c} D^{1/2}\} - \ln D^{-1/2}].$$

Figure 8.25 shows, in a schematic fashion, how the yield stress of a steel with two grain sizes ($D_1 < D_2$) varies with temperature. The ductile–brittle transition temperatures (DBTT) for the two grain sizes are also marked in the figure. The Armstrong criterion applied to the two grain sizes leads to the prediction:

$$(\text{DBTT})_2^D > (\text{DBTT})_1^D.$$

Thus, the steel with the smaller grain size (D_1) has the lower DBTT. One can see that grain-size reduction is important in increasing both

[3] R. W. Armstrong, *Phil. Mag.*, 9 (1964) 1063.

[4] In Figure 8.21 yielding (by twinning) and fracture (by cleavage) have the same k. This is becuase the Hall–Petch slope for twinning is much higher than the one for slip.

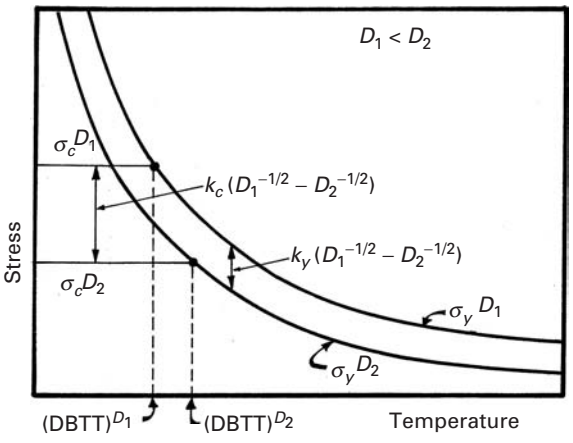

Fig. 8.25 Armstrong criterion showing effect of grain size on ductile-to-brittle transition temperature.

the strength and the range of temperatures over which it is ductile and tough.

Brittle failure of materials is a serious problem. The record of catastrophic brittle failure studies keeps increasing and has encompassed classic examples such as the *Titanic* and the World War II Liberty Ships. In the *Titanic*, rivets containing high levels of sulfur and phosphorus had a high ductile-to-brittle transition temperature and fractured in a brittle fashion, so that entire plates broke loose upon impact of the ship with the iceberg. The Liberty Ships built hurriedly during World War II were made by welding plates. The poor quality of the welds led to brittle failure in cold oceans. This led to the loss of approximately 25% of the 5,000 ships built. The problem of brittle failure is as current today as it was in past centuries, when British soldiers discovered that their cartridges were cracked during monsoon season (a classical example of environmental-assisted cracking). In 2001, the space shuttle fleet was grounded twice; first by the discovery of cracking in the liquid hydrogen flow liners and second by bearing cracks in the crawlers that transport the shuttles to the launch site.[5]

Brittle failure takes many forms, e.g. hydrogen embrittlement, temper embrittlement, stress-corrosion cracking, fatigue failure, irradiation-induced embrittlement, and liquid-metal embrittlement. Some of these will be discussed separately in Chapter 14 (Fatigue) and Chapter 16 (Environmental Effects).

The grain boundary and segregation of undesirable elements to the boundary play a role in many brittle fractures. Minute amounts of additions can completely change the fracture mechanism and morphology. The impurities often segregate to the grain boundaries, changing their strength. A few parts per million (ppm) of impurities are sufficient to decrease the grain boundary cohesion. This is

[5] D. B. Williams, M. Watanabe, C. Li, and V. J. Keast, in *Nano and Microstructural Design of Advanced Materials*, eds. M. A. Meyers, R. O. Richie, and M. Sarikaya (Oxford, U.K.: Elsevier, 2003).

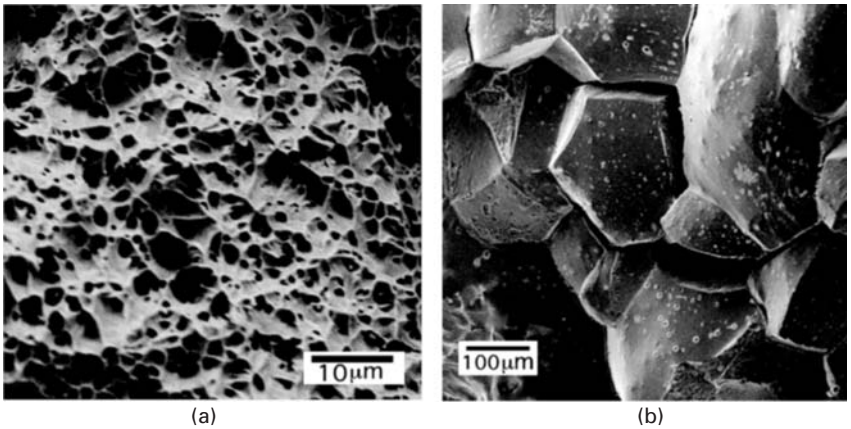

Fig. 8.26 SEM images of the fracture surface of (a) pure Cu and (b) Cu doped with 20 ppm Bi. (From D. B. Williams, M. Watanabe, C. Li, and V. J. Keast, in *Nano and Microstructural Design of Advanced Materials*, (Elsevier, Oxford, 2003).)

illustrated in Figure 8.26. Figure 8.26(a) shows a ductile fracture in copper, characterized by dimples and void nucleation and growth. Figure 8.26(b) shows a fracture surface in copper to which 20 ppm Bi was added. The two morphologies are completely different. The fracture mode in Figure 8.26(b) is intergranular and the material has been dramatically embrittled.

8.3 Fracture in Ceramics

8.3.1 Microstructural Aspects

Ceramics are characterized by high strength and very low ductility. Among the approaches developed to enhance the ductility (and, consequently, the fracture toughness) of ceramics are:

1. The addition of fibers to the ceramic to form a composite, making crack propagation more difficult because of crack bridging, crack deflection, fiber pullout, etc.
2. The addition of a second phase that transforms at the crack tip with a shear and dilational component, thus reducing the stress concentration at the tip of the crack.
3. The production of microcracks ahead of the crack, causing crack branching and distributing the strain energy over a larger area.
4. Careful processing in such a manner that all flaws of a size greater than the grain size are eliminated.

Figure 8.27 shows three toughening mechanisms for ceramics. The addition of fibers renders the propagation of a crack more difficult by one or more of the mechanisms to be explained in Chapter 15, on composites. The addition of a phase that undergoes a transformation is an ingenious strengthening method with great potential. It is described in detail in Chapter 11. Partially stabilized zirconia (zirconia with small additions of yttria) is the phase most commonly added. This phase has a tetragonal structure. At the crack tip, the stress field is such that the transformation from a tetragonal to a monoclinic structure takes place. This transformation produces a volume

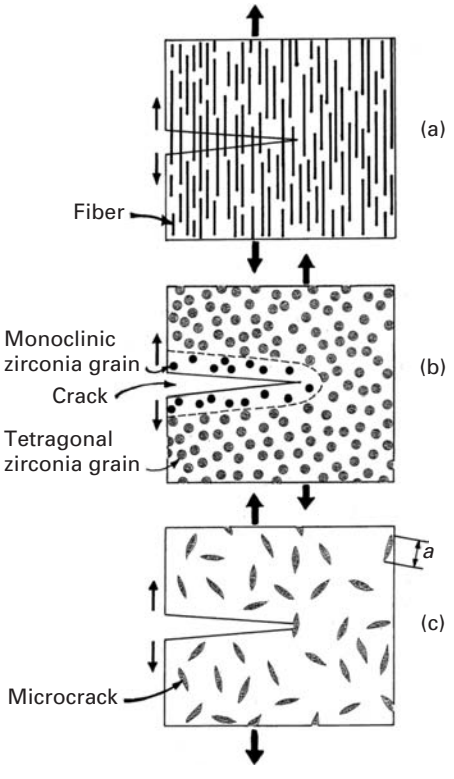

Fig. 8.27 Some toughening mechanisms in ceramics.

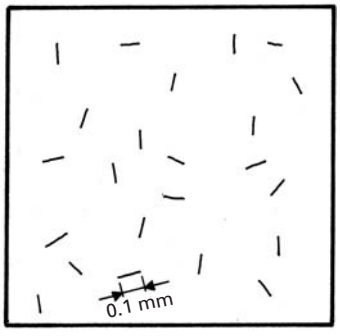

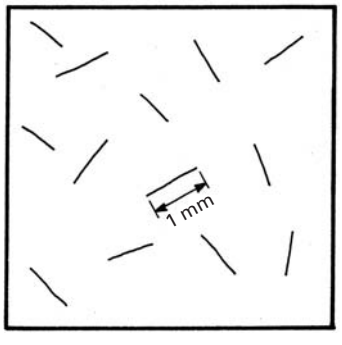

Fig. 8.28 Ceramic with two flaw-size distributions.

expansion and a shear. The dilation (volumetric strain) is approximately 4%, and the shear strain is approximately 0.16. The regions ahead of the crack tip (Figure 8.27(b)) that have the right stress state will undergo the transformation, which has the effect of adding a compressive stress at the crack tip that will tend to close it. Thus, further progression of crack is more difficult. The fracture toughness of alumina with partially stabilized zirconia can be much higher than that of alumina alone. Also, if microcracks are generated around the second-phase particles, they will decrease the stress concentration ahead of the crack tip.

A third mechanism for toughening ceramics is to form microcracks ahead of the main crack. This is shown in Figure 8.27(c). The microcracks have the effect of decreasing the stress intensity factor at the root of the principal crack. An additional effect is that they can lead to crack branching. One single crack branches into several cracks, and the stress required to drive a number of cracks is higher than that required to drive a single crack.

A fourth mechanism for strengthening ceramics is careful processing so as to eliminate, as much as possible, flaws in the material. Figure 8.28 shows identical materials with two flaw-size distributions. Application of the simple equation from fracture mechanics, $K_{Ic} = \sigma\sqrt{\pi a}$, tells us that, for a common ceramic having a fracture toughness of 4 MPa $m^{1/2}$ a reduction in flaw size from 1 to 0.1 mm has the

Table 8.2 Compressive, Tensile, and Flexural Strengths of Ceramics[a]

		Compressive Strength, MPa	Tensile Strength, MPa	Flexural Strength, MPa
Alumina (different purities)	85	1,620	120	290
	90	2,415	140	320
	95	2,411	190	340
	99	2,583	210	340
Aluminosilicate		275	17	62
ZrO_2–Al_2O_3		2,411		
3% Y_2O_3 PSZ [b]		2,962		1,170
Transformation Toughened Zirconia		1,757	350	630
9% MgO Partially Stabilized Zirconia[b]		1,860		690
Reaction-bonded SiC		689	140	255
Pressureless sintered SiC		3,858	170	550
Sintered SiC with free silicon		1,030	165	320
Sintered SiC with graphite		410	35	55
Reaction-bonded Si_3N_4		770		210
Hot-pressed Si_3N_4		3,445		860

[a] Adapted with permission from *Guide to Engineered Materials* (Metals Park, OH: ASM International, 1985), p. 16.
[b] Data are from a variety of commercial sources.

effect of increasing the maximum tensile stress that the ceramic will withstand from 16 to 56 MPa.

In spite of the processes just described to increase the ductility of ceramics, as a rule, ceramics are not very ductile. Their low ductility and relatively low resistance to crack propagation are responsible for the great differential between the compressive and tensile strength of ceramics. In metals, the difference is relatively small, because failure is often initiated only after considerable plastic deformation. The compressive strength of ceramics is close to ten times their tensile stress. This same proportion is also observed in rocks. Table 8.2 shows the compressive and tensile strengths of a number of ceramics.

It is the *inability* of ceramics to undergo plastic deformation that is responsible for the drastic difference in mechanical performance between metals and ceramics. This inability renders ceramics much stronger, but their ability to resist the propagation of cracks is decreased drastically.

The surface morphology of fractures in ceramics tends to present some markedly different features from those appearing in metals. Usually, failure begins at a flaw and propagates slowly. As it accelerates, its energy release rate increases, and there is a tendency for branching; Figure 8.29(a) shows a crack schematically. The origin of the crack is shown by the leftmost arrow. At *0* and *0′* in a brittle material, branching starts, and the crack becomes a multitude of cracks. This is seen most clearly in glass, but is also observed in crystalline

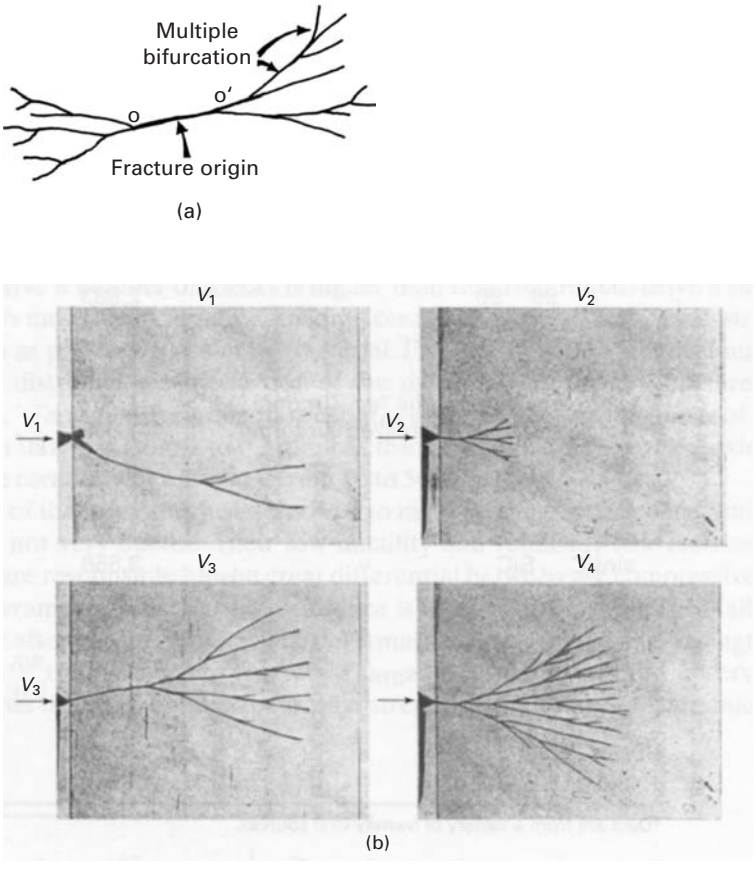

Fig. 8.29 (a) Schematic illustrating a typical crack morphology in the vicinity of the origin, and (b) crack bifurcation in glass from an edge initiated failure, caused by sharp instrument blow on left-hand side; blow velocity $V_1 < V_2 < V_3 < V_4$. (Adapted from H. Schardin, in *Fracture*, eds. B. L. Averbach, D. K. Felbeck, G. T. Hahn, and D. A. Thomas (Cambridge, MA: MIT Press, 1959), p. 297.)

ceramics. Figure 8.29(b) shows a sequence of photographs of crack branching (or bifurcation) in glass. A sharp hammer impacted the left-hand size of the glass at different velocities in Figure 8.29(b). As the velocity (and force) of the blow increase, the extent of bifurcation of the cracks increases. Hence, we can understand how shattering of brittle materials occurs. The student is well aware that a glass or a coffee mug (a ceramic!) will break into more parts if the fall is from a greater height. In Figure 8.29(b), the blow velocities are $V_4 > V_3 > V_2 > V_1$. If one looks at the fracture surface, one can often identify the origin of the failure by a smooth area, called the *mirror* region. At the center of this smooth area, the vestiges of the initial flaw can be seen. This mirror area becomes more irregular as the crack propagates from the initial flaw. This is called the *mist* region. As branching becomes prevalent, the flat, smooth surface becomes markedly irregular, and this region is called the *hackle* region. (These are similar to the ones observed in polymers and shown later on in Figure 8.42.)

When crack branching (bifurcation) starts, the fracture surface becomes increasingly irregular, because, on separation, different fracture planes become interconnected. In ceramics, the flaws are extremely important, and their concentration and size determine the strength of the ceramic. These flaws can be classified into three groups: flaws produced during processing, flaws induced by improper

Table 8.3 Sources of Flaws in Ceramics

Processing	Thermal stresses
	Machining
	Large pores
	Isolated large grains
	Cracked grains
	Inclusions
	Laminations during pressing
Design	Stress concentrations due to sharp corners, holes, improper design, etc.
Service	Impact
	Environmental degradation

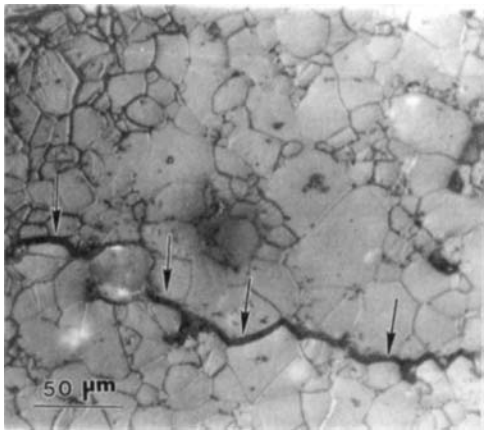

Fig. 8.30 Intergranular crack produced by thermal shock (rapid cooling) of alumina. (See arrows.)

design, and flaws introduced during service. Table 8.3 gives examples of the various flaws. Since the strength of ceramics is determined by the basic equation of fracture mechanics, that is,

$$K_{Ic} = \sigma\sqrt{\pi a},$$

it is essential to take care to eliminate flaws (or reduce their number as much as possible).

Flaws induced during processing can be of various kinds. Thermal stresses are an important source of cracks. Thermal stresses are caused by the anisotropy of thermal expansion coefficients in noncubic ceramics. If the ceramic is rapidly cooled, intense internal stresses are set up, leading to microcracks and even total fragmentation of the object. Figure 8.30 shows an intergranular crack produced by thermal shock in alumina. This piece of alumina was cooled fairly rapidly by quenching it in water, from 1,000 °C. The intergranular crack can be clearly seen. Figure 8.31(a) shows voids in AD85 alumina (85% Al_2O_3, plus a glassy phase). These voids account for approximately 12% of the volume of the material and are a commonly encountered feature of crystalline ceramics. The voids are larger than the individual grains of the material; the micrograph in Figure 8.31(b) reveals the inside of a void, which clearly shows

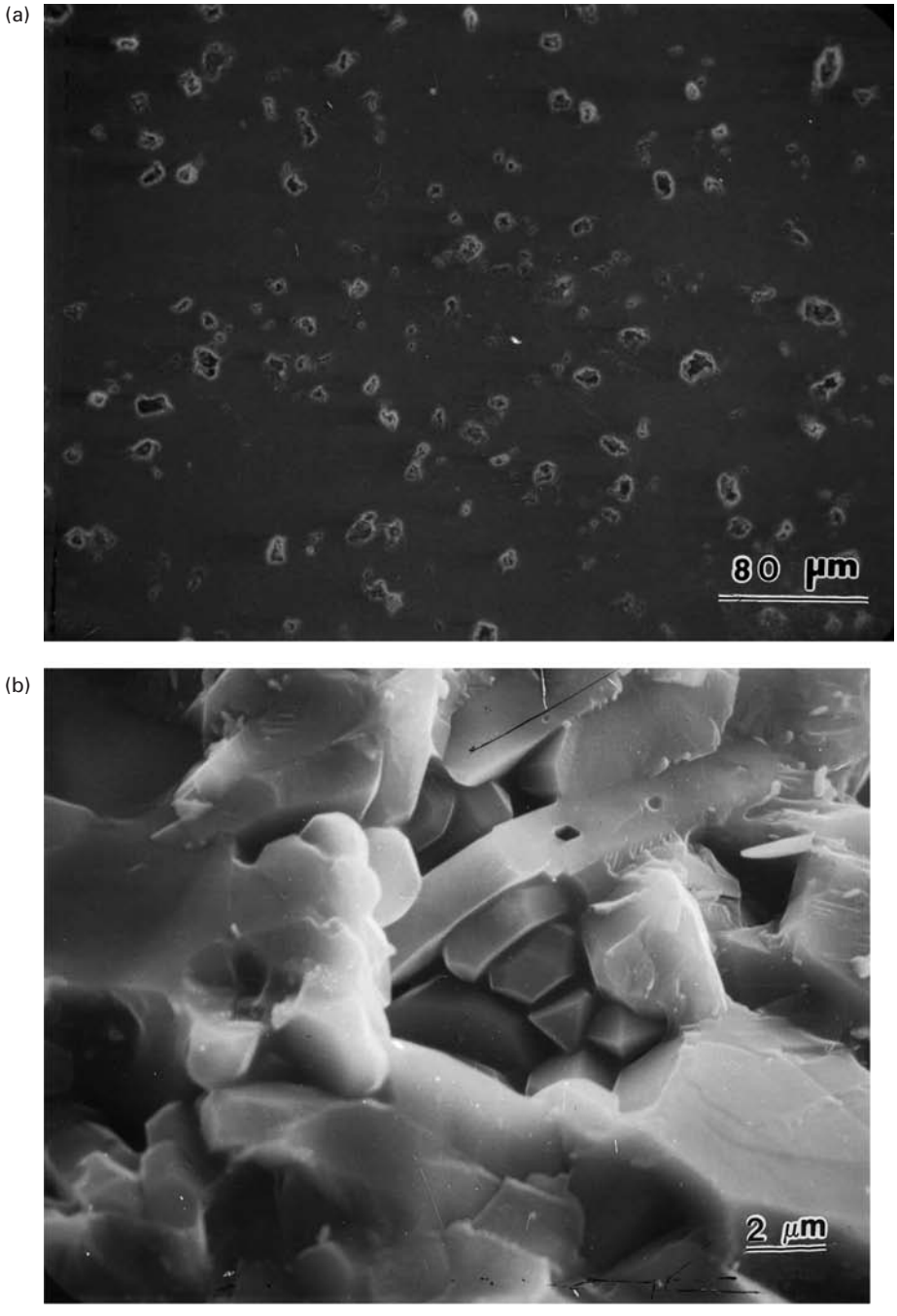

Fig. 8.31 Voids in AD85 alumina. (a) Scanning electron micrograph of sectioned surface at low magnification. (b) Enlarged view of one void. These voids are larger than the grains.

the individual grains. Defects introduced by machining are also elusive, but dangerous, flaws. These flaws are close to the surface. Isolated large grains, cracked grains, and inclusions are other sources of flaws. Inclusions are often the result of contamination during processing. During pressing or subsequent drying, laminations are often formed. During drying, the laminations can become separated from each other.

Table 8.4 Toughness Values for Ceramics[a] (Adapted with permission from *Guide to Engineered Materials* (Metals Park, OH: ASM International), p. 16)

Material	Comments	Toughness, K_c (MPa $m^{1/2}$)[1]
NaCl	Monocrystal	0.4
Soda–lime glass[b]	Amorphous	0.74 DCB
Aluminosilicate glass	Amorphous	0.91 DCB
WC/Co	Composite	13.0
ZnS	Vapor deposited	1.0
Si_3N_4	Hot pressed	5.0
Al_2O_3	MgO doped	4.0
Al_2O_3 (sapphire)	Monocrystal	2.1
SiC	Hot pressed	4.0
SiC–ZrO_2[c]	Hot pressed	5.0
MgF	Hot pressed	0.9
MgO[2]	Hot pressed	1.2
B_4C	Hot pressed	6.0
Si	Monocrystal	0.6
ZrO_2	Ca stabilized	7.6 DCB

[a] Obtained by double torsion measurement technique, except where double cantilever beam test (DCB) is indicated.

[b] Commercial sheet glass.

[c] 20% ZrO_2 14% mullite by weight. ZrO_2 present in monoclinic form; no transformation toughening.

The second category of sources of flaws listed in Table 8.3 consists of flaws introduced during the design of the material. Ceramic components have to be designed in such a manner as to avoid sharp corners that are stress raisers. Rather large stress concentrations can be generated by notches, holes, etc. (See Chapter 7.) Regions of components under tension should be minimized because of the great differences between the compressive and tensile strength of ceramics. Design should maximize compression for this reason. It is also known that a component under compression and having a hole will be subjected to some tension (see Section 7.3.2).

The last category of sources of flaws given in Table 8.3 involves those flaws introduced during service of the material, as a product. The classic example of the flaw introduced by a rock hitting the glass windshield of an automobile is the most common. The small flaw thus created will eventually generate a crack, which, in most cases, will make the windshield unusable after a certain time. Ceramics are subjected to similar effects, by impact or other sources. Another source of flaws in ceramics is the environment, coupled with stresses. Environmentally assisted cracking in ceramics has many similarities with that in metals.

The fracture of ceramics under tensile loading is essentially dictated by linear elastic fracture mechanics. Thus, the concepts K_{Ic}, J_{Ic}, and R curve are all applicable to ceramics. Table 8.4 presents fracture

toughness values for a number of ceramics; they are much lower than those of metals, shown in Table 7.1. The second-highest toughness listed in the table is that for zirconia, approximately 8 MPa $m^{1/2}$. The highest listed is that of WC/Co, which has a small amount of cobalt as a matrix, i.e. a metal matrix composite; this is the reason for the high value of 13 MPa $m^{1/2}$. Zirconia undergoes a tetragonal monoclinic transformation at the tip of the crack, decreasing the stress concentration there. Ceramics with tetragonal zirconia particles can benefit from this transformation. (See Chapter 11.)

Example 8.1

Consider polycrystalline alumina samples with two grain sizes: 0.5 and 50 μm. During cooling, the thermal expansion mismatch produces cracks that have approximate dimensions equal to the grain-boundary facets. If $K_{Ic} = 4$ MN $m^{1/2}$, determine the tensile strength of each sample.

Solution: We assume that the flaw size, i.e., $2a$, is equal to the grain size. Then

$$a_1 = \frac{0.5}{2} \times 10^{-6}\ \text{m},$$
$$a_2 = 25 \times 10^{-6}\ \text{m},$$
$$K_{Ic} = Y\sigma\sqrt{\pi a}.$$

We take the geometric factor Y to be 1.12:

$$\sigma_1 = \frac{K_{Ic}}{Y\sqrt{\pi a}} = \frac{4 \times 10^6}{9.9 \times 10^{-4}} \approx 4\,\text{GPa},$$
$$\sigma_2 = \frac{4 \times 10^6}{9.9 \times 10^{-3}} = 400\,\text{MPa}.$$

8.3.2 Effect of Grain Size on Strength of Ceramics

Mechanical properties of ceramics are affected by grain size in several ways. The most important effect is the reduction in the sizes of inherent flaws, as the grain size is reduced. One often finds flaws in a ceramic, caused by processing, that have a characteristic size of the same order of the grain size. The fracture toughness K_{Ic} of a ceramic being an intrinsic property, the tensile stress at which a flaw will be activated is dictated by the equation

$$\sigma = K_{Ic}/\sqrt{\pi a}. \tag{8.1}$$

Since the flaw size is often established by the grain size ($2a = D$), one has

$$\sigma = \frac{\sqrt{K_{Ic}}}{\sqrt{\pi D/2}}. \tag{8.2}$$

This factor is important in the tensile strength of ceramics.

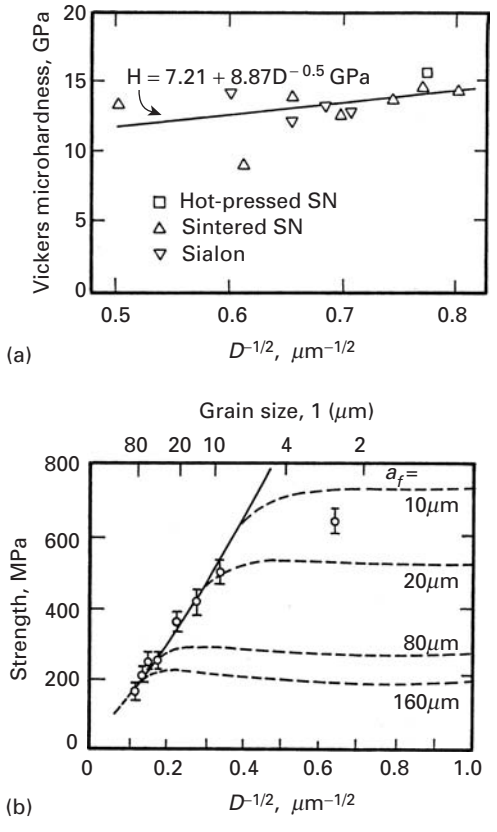

Fig. 8.32 (a) Effect of grain size on microhardness of hot-pressed and sintered Si_3N_4 and sialon. (From A. K. Mukhopadhyay, S. K. Datta, and D. Chakraborty, *J. European Cer. Soc.*, 6 (1990) 303.) (b) Strength as function of grain size for alumina; a_f is the flaw size. The solid curve refers to flaws having size $a_f = 0.5D$ (facet flaws) and the dashed lines to flaws of fixed size. (Adapted from P. Chantikul, S. J. Bennison, and B. R. Lawn, *J. Am Cer. Soc.* 73 (1990) 2419.)

The microindentation hardness of ceramics has also been found to be somewhat sensitive to grain size. Figure 8.32(a) shows microhardnesses for hot pressed and sintered silicon nitride, as well as for sialon (a silicon–aluminum–oxygen–nitrogen compound). The hardness increases with a decrease in grain size (D), and the results are plotted in a Hall–Petch fashion i.e., hardness vs. $D^{-1/2}$. However, this effect is not as important as in metals.

Figure 8.32(b) shows the effect of grain size of the strength of alumina. The solid line represents the application of Equation 8.2. For smaller grain sizes, there are deviations (dashed lines), and other factors enter into consideration as well. Nanocrystalline ceramics possess a property of considerable technological significance: superplasticity. This property enables ceramics to undergo plastic deformation in tension and compression. Tensile elongations as high as 800% have been obtained at moderate temperatures (half the melting point of the material). Nanocrystalline TiO_2 deforms superplasticity at temperatures as low as 600 °C, around 300 °C lower than the submicrometer-size oxide. Nanocrystalline zirconia has been shown to exhibit superplastic strain rates 34 times faster than 0.3-μm zirconia. These results can be rationalized in terms of the decreasing distance between the grain boundaries, helping plastic deformation by both Coble (grain-boundary sliding) or Nabarro–Herring creep, each of

which is described in detail in Chapter 5. Nabarro–Herring creep predicts a strain rate that is a function of D^{-3}, whereas grain-boundary creep predicts a strain rate that varies with D^{-2}. Clearly, the strain rate in creep is a strong function of the grain size D.

8.3.3 Fracture of Ceramics in Tension

Most often, tensile stresses produce mode I fracture in ceramics. Such tensile stresses can be generated by actual tensile testing or by flexural testing. Flexural testing produces a tensile stress in the outer layers of the specimen. The crack propagation path is the one that requires the least energy, and intergranular fracture is often observed in ceramics. Figure 8.33(a) shows an intergranular fracture in alumina produced by bending. The fracture follows, for the most part, the grain boundaries, although transgranular fracture is also observed in some places. Figure 8.33(b) shows a primarily intergranular fracture in TiB_2.

In single-crystal alumina (sapphire), there are no grain boundaries; therefore, the fracture cannot be intergranular, but will instead propagate through the crystal. In such a monocrystal, different crystallographic planes have different surface energies, and fracture will occur on those planes with the least energy. For polycrystalline alumina, the tensile strength is approximately 0.20 GPa, while the tensile strength of single-crystal alumina is 7–15 GPa. This is fairly close to the theoretical strength. The fracture of sapphire usually does not occur along the basal plane, because the surface energy of the (0001) plane is very high. Separation along this plane is difficult, as it is not electrostatically neutral. The basal plane can be visualized as consisting of oxygen atoms. (See Figure 4.43.) Thus, basal plane (0001) fracture would necessitate the separation of oppositely charged ions between planes and would require great energy. Table 8.5 shows the surface energies for sapphire along different planes. From these values, one can see that the $\{1010\}$ and $\{1012\}$ planes would be the preferred fracture planes. These high values of surface energy also explain why fracture in polycrystals tends to be intergranular. Another reason is that, in anisotropic materials (materials that are anisotropic in their elastic constants or thermal expansion coefficients), the grain boundaries are regions of stress concentration in which the initiation of a fracture is more likely to occur than in other regions. Figure 8.34 shows a scanning electron micrograph of a fracture surface in a single crystal of sapphire. The flat surfaces are the planes where the surface energy is the lowest.

According to fracture mechanics, internal flaws intensify the externally applied forces; furthermore, this intensification factor depends on the size of the flaw. Thus, specimens with different flaw size distributions will have different strengths. It is well known that the tensile strength of ceramics shows a much greater variability than that of metals. While the yield stress of most metals shows a standard deviation of 5% or less, the tensile strength of ceramics often shows a standard deviation of 25%. The great variation in results from test to test necessitates the use of statistics. In this regard, Weibull's

Table 8.5 Fracture Surface Energy of Sapphire at Room Temperature[a]

Fracture Plane	Fracture Surface Energy (J/m^2)
{0001}	>40
{1010}	7.3
{1012}	6
{1126}	24.4

[a] From S. M. Wiederhorn, *J. Am. Cer. Soc.* 50 (1967) 407, Table I, p. 486.

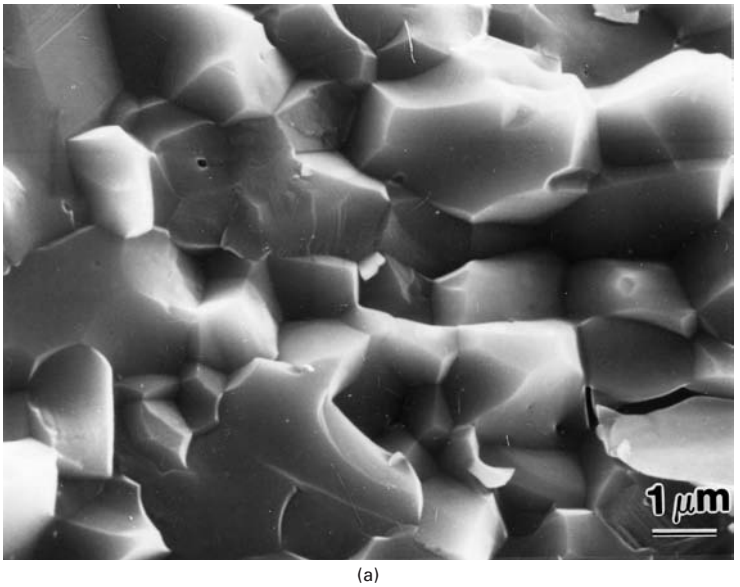

(a)

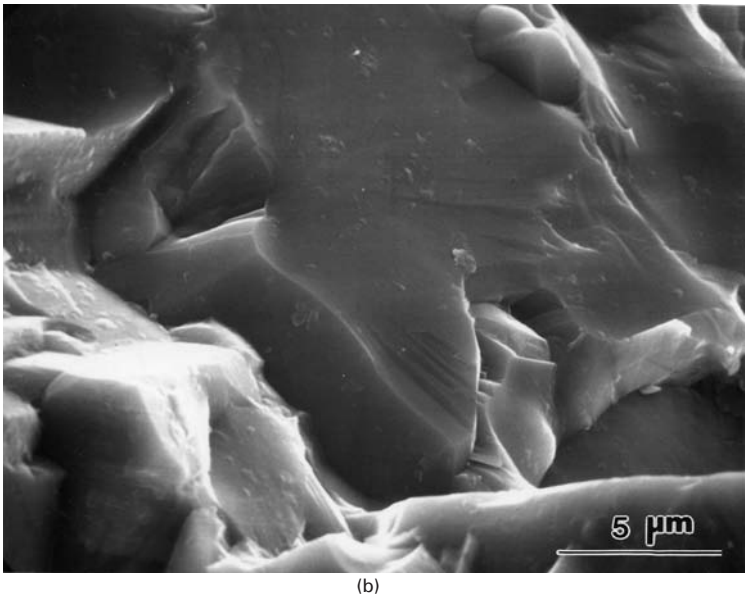

(b)

Fig. 8.33 (a) Scanning electron micrograph of fracture surface in 99.4% pure alumina. Fracture is primarily intergranular. (b) Scanning electron micrograph of tensile fracture surface in TiB_2. Fracture is primarily transgranular.

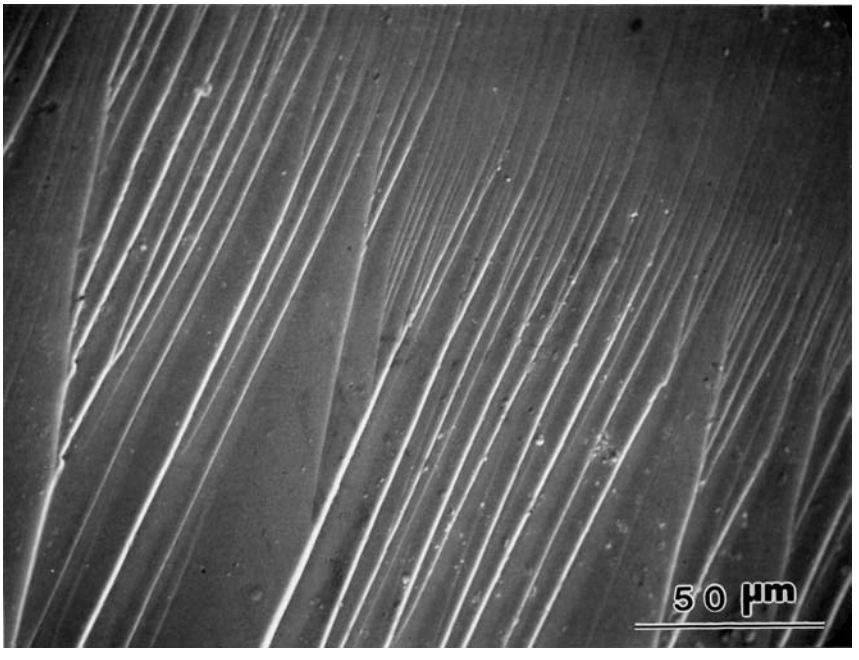

Fig. 8.34 Scanning electron micrograph of fracture surface in sapphire (monocrystalline alumina).

contribution is universally recognized.[6] The Weibull analysis is described in Chapter 7; it is sufficient here to give the basic equation for the probability that a specimen of volume V will not fail at an applied tensile stress σ. This equation is (see Equations 7.49 and 7.53)

$$P(V) = \exp\left[-\frac{V}{V_0}\left(\frac{\sigma - \sigma_u}{\sigma_0}\right)^m\right]$$

where σ_0 and V_0 are normalizing parameters, σ_u is the stress below which fracture is assumed to have zero probability, and m is called the *Weibull modulus*, a measure of the variability of the strength of the material: The greater m, the less variation there is in the strength. The Weibull modulus for ceramics is usually between 5 and 20. The equation also shows that the strength of a ceramic decreases as its volume increases. This is due to a greater probability of finding large flaws in a large specimen than in a small one. The important conclusion that can be drawn is that *it is the largest flaw that determines failure*.

The fracture toughness of monolithic ceramics varies between 1 and 5 MPa $m^{1/2}$. This toughness is dictated by the strength of the material's interatomic bonds, since little plastic deformation is involved in propagating a crack. Many methods can be used to enhance fracture toughness. However, ceramics retain sharp cracks and low ductility. Note that, although one idealizes the propagation

[6] W. Weibull, *J. Appl. Mech.*, 18 (1951) 293.

of a crack as an isolated event in a perfectly elastic material, it has been found that the stresses set up at the tip of the crack tend to generate microcracks. These microcracks change the stress field ahead of the major crack, altering its response to the applied load.

8.3.4 Fracture in Ceramics Under Compression

Fracture under tension is easy to understand, since it involves the formation of cracks (mainly at imperfections in the material) and their propagation. When a brittle metal, an intermetallic compound, or a ceramic is subjected to compression, it will eventually fail, although at stresses much higher than the tensile strength. How does it fail, since we know that cracks propagate (in mode I) under tension only? Several mechanisms have been proposed, and they all involve the formation of localized regions of tension in the material, caused by the interaction of the externally applied compressive stresses with microstructural defects. Figure 8.35(a) shows a specimen of grout (cement and sand) that failed in compression. The cracks are aligned primarily with the compression axis. The student can reproduce this type of failure by taking a piece of chalk and compressing it in a clamp or vise. The same pattern of cracks will form. This failure mode is called *axial splitting* and is very prominent for unconfined brittle materials. The sequence of events leading from the activation of existing flaws to the growth of cracks, their coalescence, and the formation of slender columns under compression is shown in Figure 8.35(b). The columns become unstable and buckle under the applied compressive loads, ejecting fragments, increasing the load on the remaining specimen, and leading to complete failure.

Griffith was the first to propose a mechanism for the compressive fracture of brittle materials.[7] The mechanism is shown in Figure 8.36. It is based on a pre-existing crack of length $2a$ oriented at an angle ψ to the highest compressive stress (σ_c). This compressive stress will cause a shear stress acting on the opposite faces of the pre-existing flaw. Thus, sliding of the two surfaces will take place. At the ends of the flaw, this sliding is prevented. This will lead to a localized tensile stress ahead of flaw (marked by a plus sign in Figure 8.36(a)) that will, eventually, nucleate two cracks (Figure 8.36(b)). Initially, the cracks will grow at an angle of 70° to the face of the flaw and will then align themselves with the direction of the maximum compressive stress (Figure 8.36(b)). The equations developed by Griffith, called the Griffith criterion, are given in Section 3.7.5. They predict a compressive strength for brittle material eight times larger than the tensile strength. The mathematical analysis of the stresses created at the end of the flaw is based on the scheme shown in Figure 8.36(c). Normal and shear stresses σ'_{22} and σ'_{12} are determined in the plane of the flaw. A frictional resistance μ can be assumed at the flaw surfaces. The wing cracks have length ℓ in Figure 8.36(c). A simpler situation

[7] A. A. Griffith, *Proc. First Int. Cong. App. Mech.*, 1 (1924) 55.

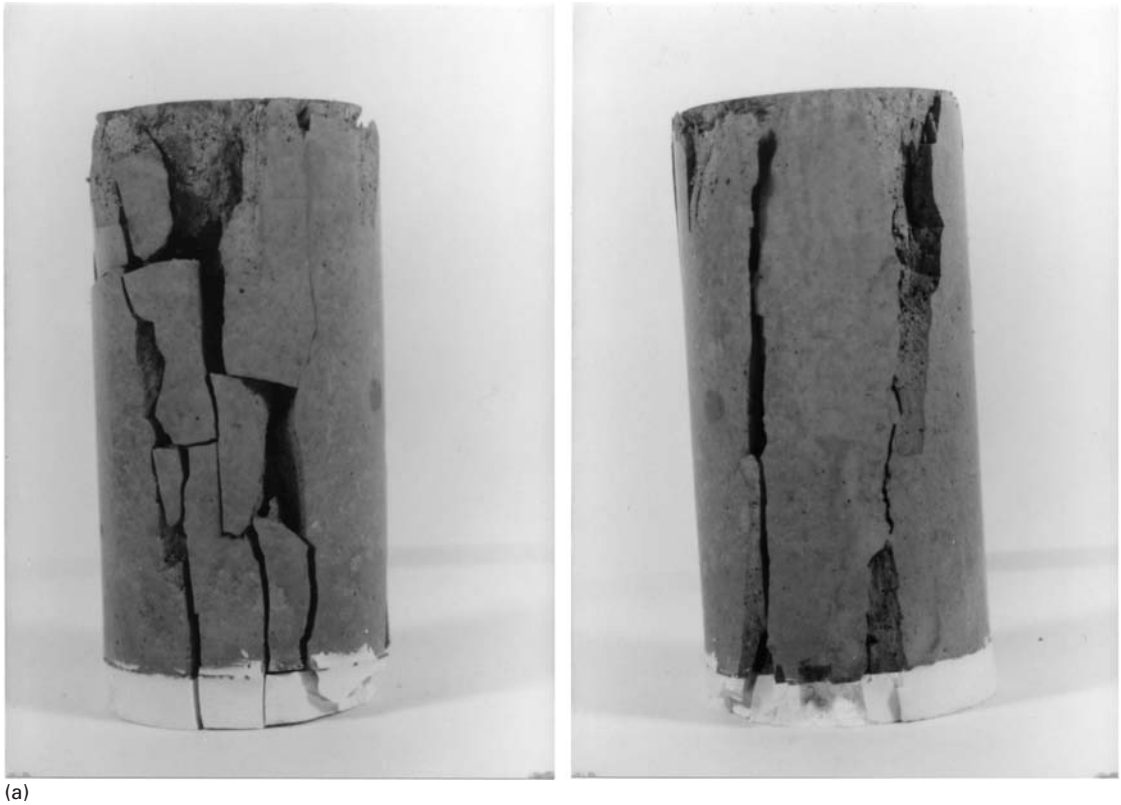

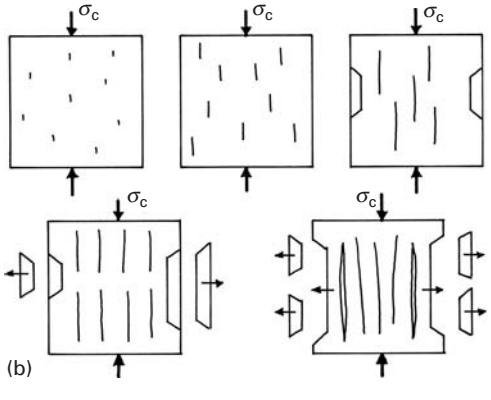

Fig. 8.35 (a) Compressive failure of brittle material by axial splitting. (b) Schematic representation of growth of critical cracks, producing axial splitting and spalling of fragments; separate columns under compression will collapse.

is when the flaw is spherical. In this case, (tangential) tensile stresses generated at the north and south pole of the flaw can generate cracks. (See Figure 8.36(d).) The introduction of lateral stresses σ_ℓ (also called lateral confinement) alters the propagation of wing cracks and their interaction and has a profound effect on final failure.

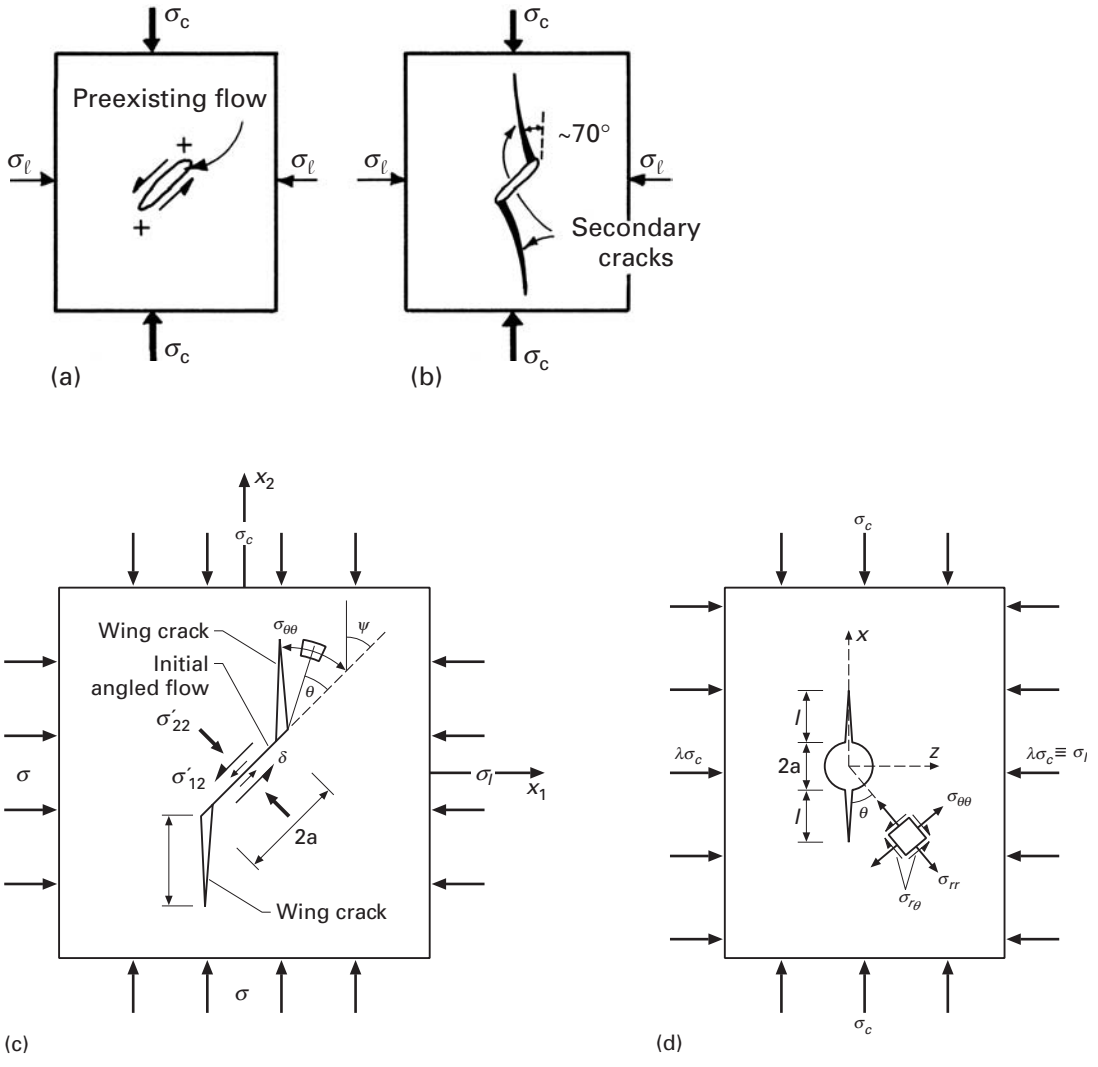

Fig. 8.36 (a) Schematic representation of elliptical flaw subjected to compressive stress σ_c; σ_l is lateral stress. (b) Formation of "wing" cracks from ends of flaw. (c) Stresses generated by flaw of orientation ψ with compressive axis. (Adapted from M. F. Ashby and S. D. Hallam, *Acta. Met.*, 34 (1986) 497.) (d) Circular flaw generating crack. (Adapted from C. G. Sammis and M. F. Ashby, *Acta Met.*, 34 (1986) 511.)

Failure of brittle materials under compression is activated by existing flaws. Brittle metals (cast iron, intermetallics), ceramics, ceramic composites, concrete, and rock are subjected to these mechanisms. Spherical voids and sharp (crack-like) flaws are often produced during the processing of brittle materials. For example, spherical voids are generated during sintering and hot pressing of ceramic powders and are the remnants of the material's initial porosity. Microcracks are created by thermal expansion mismatch (especially in noncubic materials). Frequently, the scale of the microcracks is that of the grain size; they tend to extend from boundary to boundary. The compressive failure of brittle materials is strongly affected by lateral confinement (stresses transverse to the loading direction). Figure 8.37 shows how cracks aligned with the principal direction of loading are generated at spherical and sharp flaws and how they lead to failure. The stress–strain curves and the interactions between the cracks

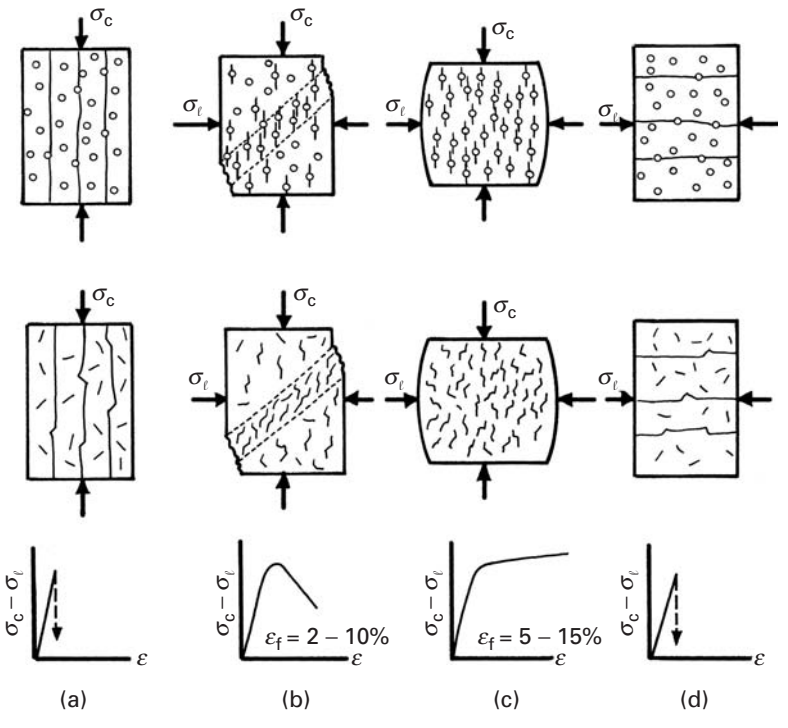

Fig. 8.37 Failure modes in compression for brittle materials containing spherical and flat flaws, as a function of increasing confinement (σ_ℓ/σ_c). (a) Simple compression, giving failure by "axial splitting," or "slabbing." (b) Small confining stress, resulting in shear failure. (c) Large confining stresses σ_ℓ, providing homogeneous microcracking and a "pseudoplastic" response. (d) σ_c becomes equal to zero; the situation is identical to (a), but rotated by 90°. (Adapted from C. G. Sammis and M. F. Ashby, *Acta Met.*, 34 (1986) 511; and M. F. Ashby and S. D. Hallam, *Acta Met.*, 34 (1986) 497.)

are dependent on the lateral confinement of the material, which is increased from left to right. In the absence of confinement ($\sigma_\ell = 0$), the cracks generated at flaws can grow indefinitely under increasing compressive stress σ_c. They split the specimen vertically, and the segments become unstable and crumble – for instance, from Euler instability. As confinement is increased, the growth of cracks is hindered, and failure occurs along a band of shear localization, where a larger number of cracks is formed. At a still larger confinement (Figure 8.37(c)) the brittle material exhibits a "pseudoplastic" response, with numerous flaws activating cracks. Finally, in Figure 8.37(d), axial splitting (also called "slabbing") occurs at 90° to the first case (Figure 8.37(a)).

Calculations analogous to those of Griffith were carried out for elliptical flaws by Ashby and Hallam[8] and Horii and Nemat–Nasser.[9] The Ashby–Hallam equations are given here.

When the friction coefficient μ is zero, the angle ψ for which K_I is maximum is, as expected, 45°. By making $\sigma_\ell/\sigma_c, = \lambda$, the following equation is obtained:

$$K_I = -\frac{\sigma_c\sqrt{\pi a}}{\sqrt{3}}[(1-\lambda)(1+\mu^2)^{1/2} - (1+\lambda)\mu].$$

[8] M. E. Ashby and S. D. Hallam, *Acta Met.*, 34 (1986), 497.

[9] H. Horii and S. Nemat–Nasser, *J. Geophys. Res.*, 90 (1985) 3105; and *Phil. Trans. Roy Soc.* (London), 319 (1986) 337.

The critical value of the stress intensity factor, K_{Ic}, is reached at the stress level at which wing crack growth starts. For a crack making an angle $\psi = (1/2)\tan^{-1}(1/\mu)$ with the principal loading axis, we have

$$\frac{\sigma_c\sqrt{\pi a}}{K_{Ic}} = \frac{-\sqrt{3}}{[(1-\lambda)(1+\mu^2)^{1/2} - (1+\lambda)\mu]}.$$

Ashby and Hallam also obtained an expression for the increase in length of the winged cracks, $\ell/a = L$, as a function of normalized stress:

$$\frac{\sigma_c\sqrt{\pi a}}{K_{Ic}} = \frac{-(1+L)^{3/2}}{[1-\lambda-\mu(1+\lambda)-4.3\lambda L]\left[0.23L + \frac{1}{\sqrt{3}(1+L)^{1/2}}\right]}.$$

For spherical and circular flaws, the equations given in Section 7.3 can be applied. This results in the following expression:

$$\frac{\sigma_c\sqrt{\pi a}}{K_{Ic}} = -\frac{1}{L^{1/2}\left[\frac{1.1(1-2.1\lambda)}{(1+L)^{3.3}} - \lambda\right]}.$$

Under simple compression ($\lambda = 0$, $\sigma_\ell = 0$), the crack grows in a stable fashion from an initial value of normalized stress equal to 4. In an initial stage, from $L = 0$ to $L = 0.2$, the stress actually drops with increasing length. This corresponds to the initial "pop-in" stage of crack formation. Since K_{Ic} is a material constant, the compressive stress at which a crack grows decreases with increasing void size. Hence, *larger voids are more effective crack starters*. For lateral tension ($\lambda < 0$), the crack grows in a stable fashion to a certain size and then grows unstably (in the region where σ_c decreases with increasing L). The equations also show the total suppression of crack growth when $\lambda \geq \frac{1}{3}$.

Additional mechanisms involving dislocations, anisotropy of the elastic properties of adjacent grains, and dislocation–grain-boundary interactions were proposed by Lankford,[10] who studied the behavior of alumina under compression and found localized plasticity (caused by either twinning or dislocations) at stresses below the compressive failure stress. The interaction of deformation bands with grain boundaries caused microcracks to begin forming. Figure 8.38 shows a schematic indicating how microstructural anisotropy can lead to stress concentrations at the grain boundaries. If two adjacent grains have different elastic moduli along the axis of compression (because of differences in crystallographic orientation), they will tend to deform differently. This will impose additional stresses on the grain boundaries because of compatibility requirements (Figure 8.38(a)). In a similar way, deformation bands (whether they be dislocations or twins) will create stress concentrations at the grain boundaries (Figure 8.38(b)). Figure 8.38(c) shows examples of a crack produced by different interactions with a grain boundary. Thus, failure of a ceramic under compression is a gradual process, although the actual fracture

[10] J. Lankford, *J. Mater. Sci.*, 12 (1977) 791.

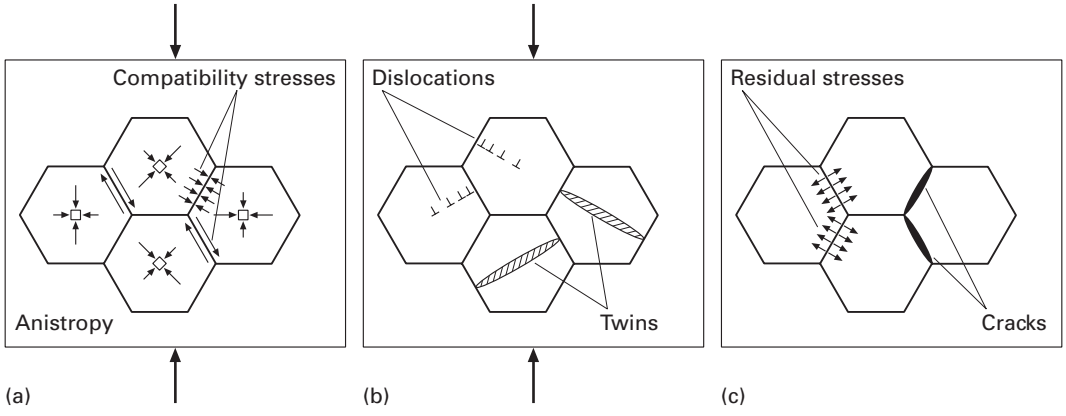

Fig. 8.38 Schematic showing how (a) anisotropy of elastic properties and (b) localized plastic deformation can lead to stress concentrations and (c) cracking at grain boundaries during unloading. (After M. A. Meyers, *Dynamic Behavior of Materials* (New York: J. Wiley, 1994), p. 559.)

often occurs in an "explosive" manner, as the ceramic fragments into many pieces due to the coalescence of microcracks.

Figure 8.39 shows several mechanisms that were identified as leading to cracking in SiC. Some of these mechanisms have been presented in Figure 8.38. Others, such as grain-boundary debonding, are specific to ceramics where the grain boundaries have a lower strength than the grain interiors. Such is often the case when ceramics are sintered and sintering agents (glasses) are used. They form a thin film at the grain boundaries. Voids are also significant initiators of cracking. Dislocation pileups create stress concentrations which eventually cause debonding (Figure 8.3) and formation of Zener–Stroh-type cracks.

8.3.5 Thermally Induced Fracture in Ceramics

Thermal stresses induced during cooling can have a profound effect on the mechanical strength of the ceramics. This can be explained in a qualitative manner by Figure 8.40. The polycrystalline aggregate is schematically represented by an array of hexagons. When the temperature is reduced from T_2 to T_1, the hexagonal grains contract. The noncubic structure of alumina and many other ceramics results in different contractions along different crystallographic orientations. The same effect manifests itself in noncubic metals. In some metals, substantial plastic deformation is observed after thermal cycling (numerous heating and cooling cycles). The problem is especially crucial in composites, where the different components often have quite different thermal expansion coefficients. The thermal expansion coefficient along the *c*-axis of Al_2O_3 is about 10% higher than perpendicular to it. The stresses set up by these differences in thermal expansion are sufficient to introduce microcracks into the material after cooling. In Figure 8.40, we would have $\Delta L_1 \neq \Delta L_2$ if the grains were free. However, each grain is constrained by its neighbors, and stresses therefore arise. These stresses are given by

$$\sigma = \frac{2}{3(1-\nu)} \int_{T_1}^{T_2} E\,(\alpha_c - \alpha_a) dT\,,$$

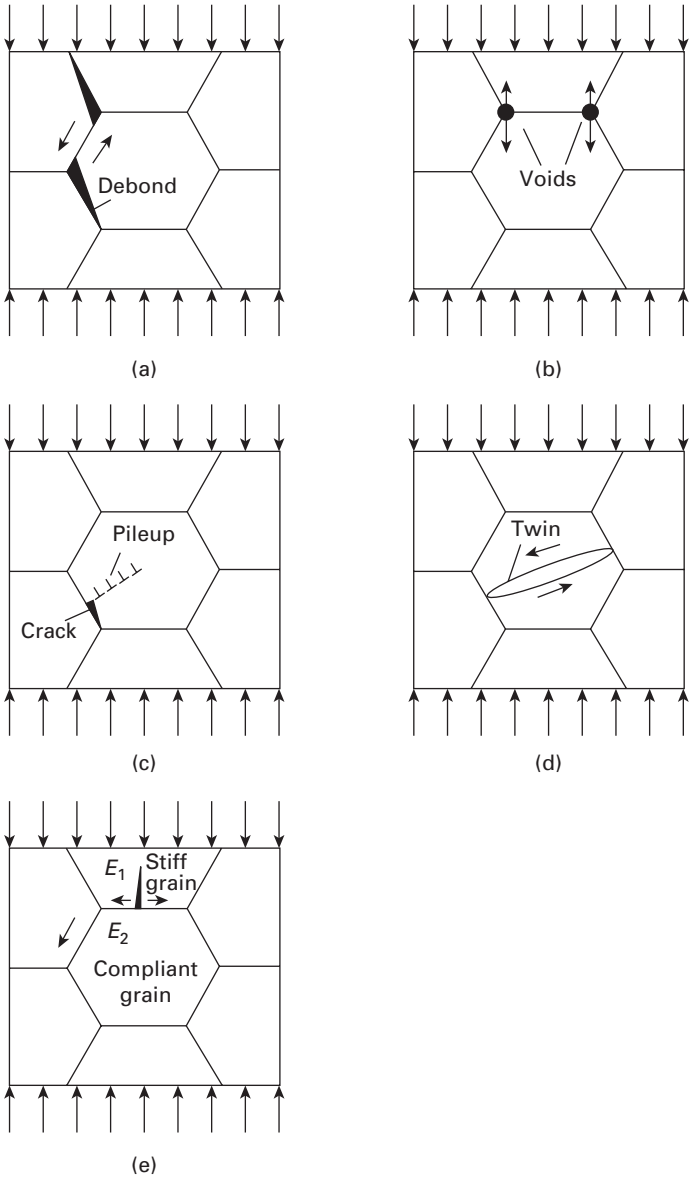

Fig. 8.39 Schematic overview of principal damage initiation mechanisms in SiC: (a) grain boundary debonding; (b) foreign particles, such as inclusions and voids at the grain boundaries; (c) dislocation pileups, leading to Zener–Stroh cracks; (d) twins and stacking faults; (e) dilatant crack produced by elastic anisotropy. (From C. J. Shih, M. A. Meyers, V. F. Nesterenko and S. J. Chen, *Acta Mater.*, 40 (2000) 2399.)

where T_1 and T_2 are the extreme temperatures of the thermal cycle, and α_a and α_c are the thermal expansion coefficients perpendicular and parallel to the *c*-axis, respectively. For constant expansion coefficients, and assuming a constant E, we get

$$\sigma = \frac{2E}{3(1-v)}\Delta\alpha\Delta T.$$

Cooling a polycrystalline alumina sample from 1,020 °C to 20 °C would generate stresses on the order of

$$\sigma = \frac{2 \times 400}{3(1-0.31)}(0.7 \times 10^{-6}) \times 1{,}000 = 0.27\,\text{GPa} = 270\,\text{MPa}$$

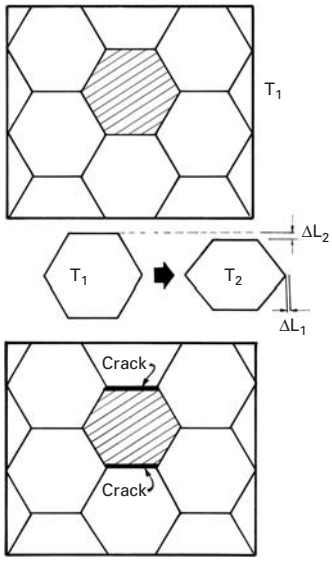

Fig. 8.40 Thermally induced cracks created when grains contract in an anisotropic fashion during cooling from T_1 to T_2.

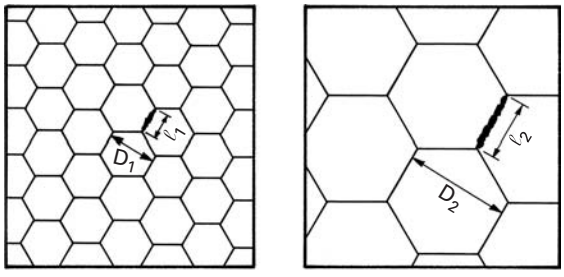

Fig. 8.41 Thermally induced microcracks in ceramic specimens with two grain sizes.

between two grains of orientations *a* and *c*. This is approximately $1\frac{1}{2}$ times the tensile strength of alumina, as can be seen from Table 8.2. Thus, microcracks can be generated by anisotropy of an expansion coefficient. Even in the case where no microcracks are generated, internal stresses remain within the grains. When a ceramic is subjected to external loading, the internal stresses due to thermal differences interact with the externally applied loads and can considerably reduce the stresses required for fracture.

The anisotropic effect of expansion on microcracking affects the strength of ceramics in a manner that is dependent on grain size. This effect, is illustrated in Figure 8.41. Here we assume that microcracks are generated by thermal anisotropy in the two specimens. The microcracks will extend over one grain face. The sizes of the two microcracks are ℓ_1 and ℓ_2 for the small and large grain-sized specimens, respectively. If the grain sizes are D_1 and D_2, we can say that

$$\frac{\ell_1}{D_1} = \frac{\ell_2}{D_2}.$$

The fracture mechanics equation

$$K_{Ic} = \sigma\sqrt{\pi a}$$

can then be applied to determine the tensile strength of the ceramics.

Thus, the tensile strength can be written as

$$\sigma = \frac{K_{Ic}}{\sqrt{\pi a}} = \frac{K_{Ic}}{\sqrt{\frac{\pi \ell}{2}}}.$$

By substituting D for ℓ and combining all constants into one, we obtain

$$\sigma = K_{Ic} k D^{-1/2}.$$

k is a parameter. This simple equation expresses the experimentally observed fact that thermal anisotropy is much more effective in weakening specimens with a large grain size than specimens with a small grain size.

Another serious problem of a thermal nature affecting ceramics is cracking, because of temperature differentials within one component. We all know that china will fracture if rapidly cooled. Ceramics

are subject to very intense stress concentrations if temperature differentials are set up within them. This is so because plastic deformation, which serves to accommodate stresses due to severe temperature gradients in metals, is mostly absent in ceramics. Thus, there are limits to the rates at which components can be cooled or heated. If these rates are exceeded, the components fail. A simple example is a furnace tube that is heated to a high temperature. If the resistance wire that heats the furnace touches the ceramic, a significant temperature gradient is established over a small distance. This temperature gradient creates stresses that lead to fracture if the tensile strength of the ceramic is exceeded. It is very common for ceramic bricks (refractory bricks) to break during cooling. In ceramics thermal shock or rapid cooling can have catastrophic effects, and the superb high-temperature properties of ceramics are of no advantage if the ceramic fails during cooling. When ceramics are used in conjunction with metals in machines, the difference between the thermal expansion coefficient of the metal and that of the ceramic can lead to failure. These aspects must be considered in the design of ceramic components, and heat transfer equations should be used to estimate the temperature differentials and the associated stresses within the ceramic.

8.4 Fracture in Polymers

The fracture process in polymers involves the breaking of inter- and intramolecular bonds. Recall that amorphous or glassy polymers have a glass transition temperature T_g, but no melting point T_m. These glassy polymers are rigid below T_g and less viscous above that temperature. Semicrystalline polymers have both a melting point and a glass transition temperature, the former referring to the crystalline phase, the latter to the amorphous phase surrounding the crystalline phase. More information about the structure of polymers is given in Chapter 1.

8.4.1 Brittle Fracture

Many polymers fracture in a brittle manner below their glass transition temperature. This is particularly true of polymers having large, bulky side groups or a high density of cross-links. Under either of these circumstances, the molecular chain structure of the polymer becomes so rigid, that chain disentanglement and/or slipping becomes very difficult. Examples of such polymers are thermosets, such as epoxy, polyester, and polystyrene. The stress–strain curve of these polymers is quite linear to fracture, and the strain to failure is typically less than 1%. Figure 8.42(a), a scanning electron micrograph, shows an example of a brittle fracture surface in a cross-linked polyester; Figure 8.42(b) shows schematically the different regions that compose such a surface. There are three regions:

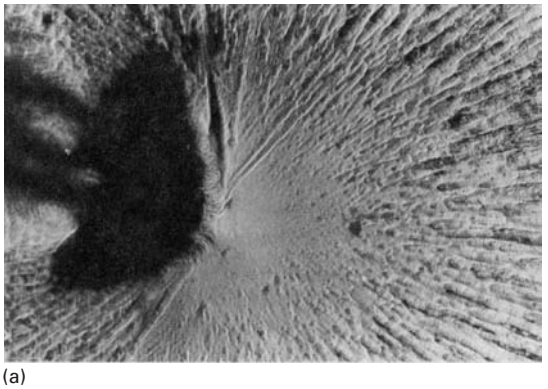
(a)

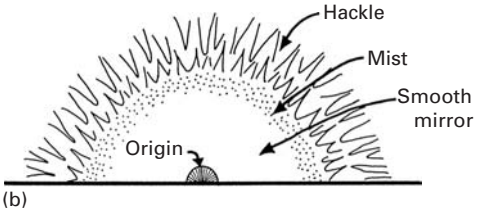

(b)

Fig. 8.42 (a) Brittle fracture in a highly cross-linked thermoset (polyester). (b) The three different regions that compose the brittle fracture surface in (a).

1. A mirrorlike, or specular, region adjoining the crack nucleation site, indicating slow crack growth.
2. A coarse and flat region indicative of fast crack growth; sometimes this region is called the region of *hackle*, and one can see that the crack has propagated on different levels over small areas. When hackle is elongated in the direction of crack propagation, the pattern is called "river markings."
3. A transitional region between the preceding two that has a *misty* appearance and no resolvable features.

Similar brittle fracture surface features are observed in ceramics. (See Figure 8.29.) In highly cross-linked thermosets, such as epoxies and polyesters, the plastic deformation before fracture is negligible. Consequently, manifestations of plastic deformation, such as crazing and shear yielding, are generally not observed.

8.4.2 Crazing and Shear Yielding

Frequently, the phenomena of crazing and shear yielding precede actual fracture in a polymer. Both these phenomena involve a localization of the plastic deformation in the material. The major difference between the two is that crazing occurs with an increase in volume, whereas shear yielding occurs at constant volume.

In glassy polymers, one can regard crazing and shear yielding as competing processes. In brittle glassy polymers, such as polymethyl methacrylate (PMMA) or polystyrene (PS), crazing precedes the final brittle fracture. In comparatively more ductile polymers (for example, polycarbonate or oriented polyethylene), which have flexible main-chain linkages, shear yielding is the dominant mode of deformation,

and the final fracture is ductile. In particular, if an oriented high-density polyethylene sheet is deformed in a direction oblique to the initial draw direction, it will show a shear deformation band in which highly localized plastic deformation occurs.

It is thought that molecular entanglements control the geometry of crazes and shear yield zones. A craze is a region of a polymer in which the normal "cooked-spaghetti-like" chain arrangement characteristic of the amorphous state has been transformed into drawn-out molecular chains interspersed by voids. The crazed region is a very small percentage of the total region of the polymer (a few nanometers to a few micrometers). Because of the presence of voids in a craze, the plastic deformation of the small volume of material in the craze occurs without an accompanying lateral contraction; that is, the constancy-of-volume condition which holds in the regular bulk polymer does not hold in the crazed material.

A craze is neither a void nor a crack. Detailed optical- and electron-microscopic observations of crazed regions show that crazes are not voids and that they are capable of transmitting load. The refractive index of a craze in a polymer such as polycarbonate, in the dry state and after immersion in ethanol, would be different. From such measurements, it was concluded that crazes contain about 50–55% by volume of free space; that is, the density of the material in the crazed region is lower than that of bulk polymer. The lower density of the crazed region reduces the refractive index of the region and causes its characteristic reflectivity. Figure 8.43 shows a series of crazes reproduced in a tensile specimen of polycarbonate. Note that several crazes have run through the entire cross section without failure of the specimen, indicating the load-bearing nature of the crazes. The volume fraction of the polymer in the craze is inversely proportional to λ, the draw ratio (final length ÷ original length) of the craze.

Although crazes are not cracks, cracks leading to final fracture may indeed start at a craze. The polymeric chains in the crazed region get highly oriented in the direction of the applied stress. The void content, as previously mentioned, can be as high as 50 to 60%. Molecular chain entanglements play an important role in controlling craze geometry. Figure 8.44 shows, schematically, craze formation at a crack tip. Crazes are usually nucleated either at surface flaws (scratches, gouge marks, and cracks) or at internal flaws (dust particles and pores). In polymers, microvoids, which are an integral part of crazes, can form at various inhomogeneities in the microstructure, such as random density fluctuations in amorphous polymers, ordered regions in semicrystalline polymers, and particulate matter or inclusions such as fillers, flame retardants, or stabilizers in either kind of polymer. Craze formation is a process of dilation and is aided by hydrostatic tension and retarded by hydrostatic compression.

Atomic force microscopy (AFM) is a powerful addition to the arsenal of characterization and mechanical testing methods. The atomic force microscope enables observation of the surface at the nanometer scale. It can also be used to determine forces at the surface and the

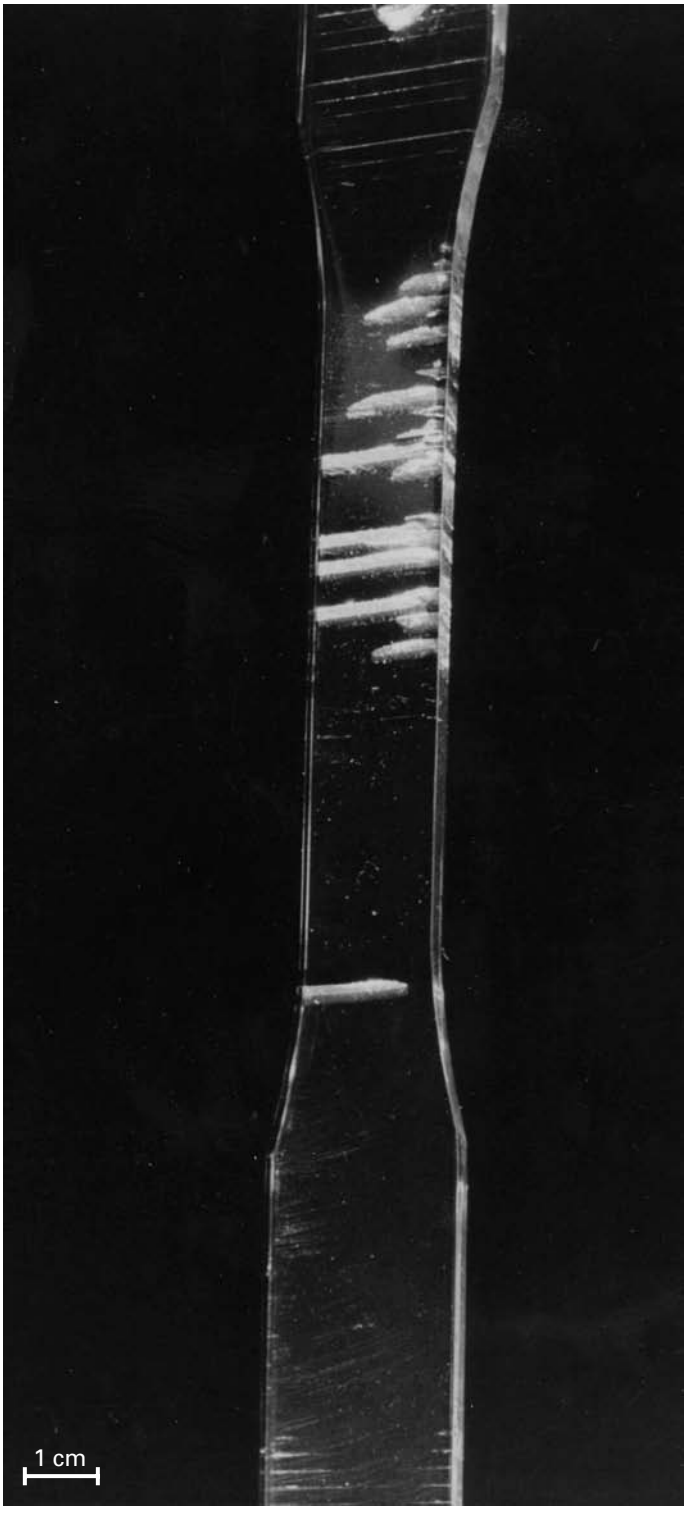

Fig. 8.43 A series of crazes produced in a tensile specimen of polycarbonate. (Used with permission from R. P. Kambour, *Polymer*, 4 (1963) 143.)

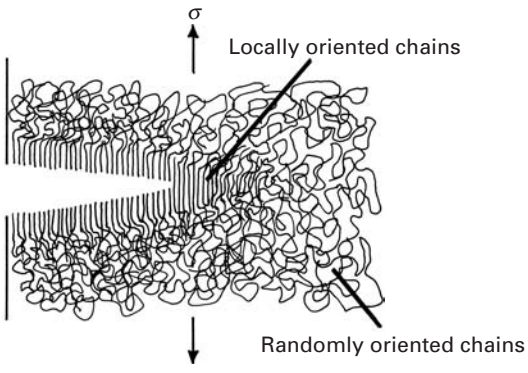

Fig. 8.44 Schematic of craze formation at a crack tip.

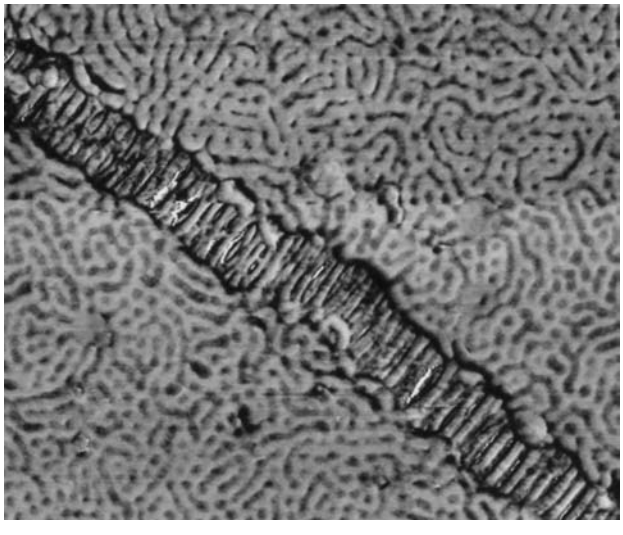

Fig. 8.45 An incipient craze in polymer; note extended polymer chains in craze; Atomic force microscope (AFM) picture. (Courtesy of J. E. Kramer.)

mechanical properties of macromolecules, such as proteins. The tip of the AFM can be used as an indenter. The force is given through the stiffness of the cantilever beam. Figure 8.45 shows an AFM of a polymer containing a craze. The individual polymer molecules are imaged. They are random; thus, the polymer is glassy. An incipient craze runs diagonally through the micrograph. The polymer chains inside the craze are aligned.

The competition between shear yielding and crazing and the importance of the microstructure are shown in Figure 8.46. Polystyrene and polyphenylene oxide (PPO) are completely miscible at all concentrations. Atactic polystyrene (APS) shows the phenomenon of crazing preceding brittle fracture. By mixing the APS and PPO, we can suppress this embrittling tendency. In fact, near 50–50 concentration, crazing in APS is completely suppressed. Instead, extensive shear yielding occurs. The figure shows this phenomenon of transition between shear yielding and crazing in 300-nm films made of blends of APS and PPO and deformed 10% at room temperature. The lower left-hand corners show the weight percentages of APS in the mixture. The letters *C*, *D*, and *S* indicate crazing,

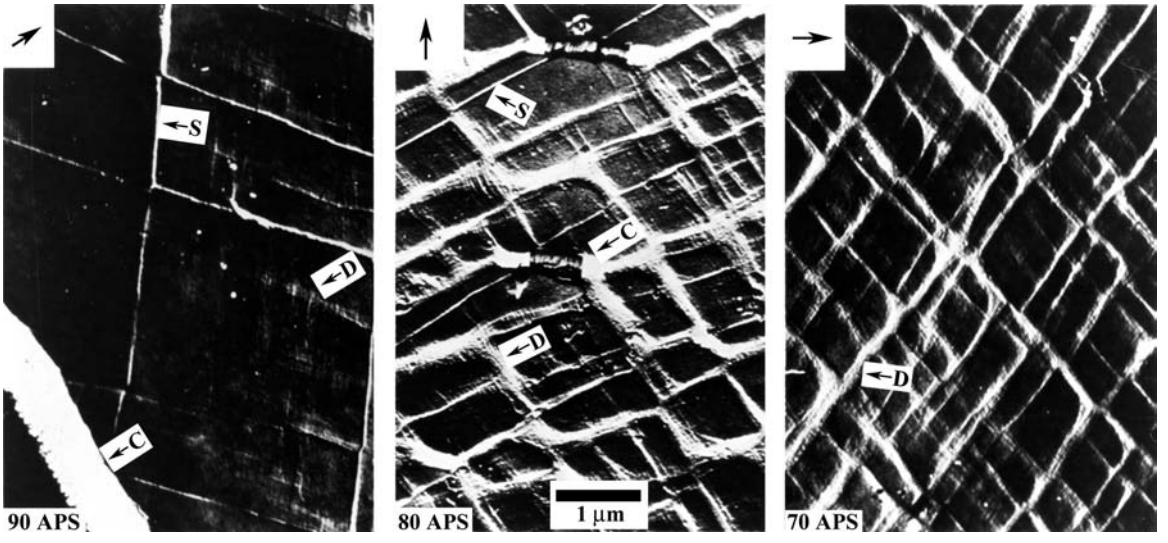

Fig. 8.46 A transition between shear yielding and crazing in film blends of polypropylene oxide (PPO) and atactic polystyrene (APS) deformed 10% at room temperature (Used with permission from E. Baer, A. Hiltner, and H. D. Keith, *Science*, 235 (1987) 1015.). The APS weight percentages are shown in the lower left-hand corners. *C*, *D*, and *S* indicate crazing, diffuse shear, and sharp shear banding, respectively. The arrows indicate the direction of deformation.

diffuse shear banding, and sharp shear banding, respectively. The upper left-hand corners indicate the direction of deformation. Note that, as the amount of PPO increases, more and more crazes are blunted by shear bands. At 70% APS (or 30% PPO), only diffuse shear bands appear.

8.4.3 Fracture in Semicrystalline and Crystalline Polymers

The crystalline regions in a semicrystalline polymer have a folded chain structure; that is, the molecular chains fold back upon themselves to form thin platelets called lamellae. (See Chapter 1.) Amorphous material, containing chain ends, tie molecules, and other material that is difficult to crystallize, separates the different lamellae. The properties of such semicrystalline polymers can be highly anisotropic – very strong and stiff in the main chain direction and weak in the transverse direction. Parameters such as the degree of crystallinity, molecular weight, orientation of the crystals, etc., affect the mechanical behavior in general and the fracture behavior in particular. Because the polymers show a significant amount of viscoelastic behavior at their service temperature, the strain rate has a profound effect on their fracture behavior. Figure 8.47 shows schematically the effect of strain rate on the fracture path through a spherulitic polypropylene. At low strain rates the fracture follows an interspherulitic path, while at high strain rates the fracture becomes transspherulitic.

As described in Chapter 1, polymers are generally amorphous or semicrystalline; it is almost impossible to get a 100% crystalline polymer. Invariably, there is some amorphous material in between crystalline regions, because defects such as chain ends, loops, chain folds, and entanglement are almost impossible to eliminate completely. Single crystals of *monomeric* polymers are prepared from dilute solutions

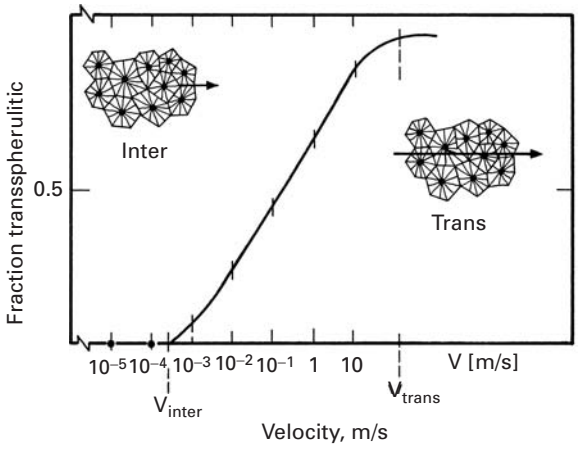

Fig. 8.47 Effect of strain rate on the fracture path through polypropylene. At low strain rates the fracture is interspherulitic, while at high strain rates it is transspherulitic. (After J. M. Schultz, *Polym. Sci. & Eng.*, 24 (1984) 770.)

or vapor phase deposition. These are transformed into polymers by means of a solid-state reaction. The technique has been successful with only certain substituted diacetylines, and that, too, in an essentially one-dimensional form, i.e., short fibers. Nevertheless, these can be used to study the behavior of single-crystal polymers. Specifically, in terms of their fracture behavior, it has been observed that single-crystal polymers cleave parallel to the chain direction because of rather weak van der Waals bonding normal to the chain and strong covalent bonding in the direction of the chain. In polydiacetylene single-crystal fibers, the fracture strength σ_f shows the following dependence on fiber diameter[11], d: $\sigma \propto d^{-1/2}$. This is similar to the size effect seen in other fibers; that is, preexisting defects lead to fracture, and the size of these defects is inversely proportional to the square root fiber diameter.

8.4.4 Toughness of Polymers

Thermosetting polymers such as polyesters, epoxies, and polyimides are highly cross-linked and provide adequate modulus, strength, and creep resistance. But the same cross-linking of molecular chains causes extreme brittleness, i.e., very low fracture toughness. Table 8.6 gives the plane-strain fracture toughness values of some common polymers at room temperature and in air. Figure 8.48 compares some common materials in terms of their fracture toughness, as measured by the fracture energy (G_{Ic}) in J/m^2. Note that thermosetting resins have values only slightly higher than those of inorganic glasses. Thermoplastic resins, such as polymethyl methacrylate, have fracture energies of about 1 kJ/m^2, while polysulfone thermoplastics have fracture energies of several kJ/m^2, almost approaching those of the 7075-T6 aluminum alloy.

[11] R. J. Young, in *Developments in Oriented Polymers*, Vol. 2, ed. I. M. Ward (Essex, U.K.: Elsevier Applied Science, 1987), p. 1.

Table 8.6 Plane-Strain Fracture Toughness (K_{Ic}) of Some Polymers in Air at 20 °C

Polymer	K_{Ic} (MPa $m^{1/2}$)
Epoxy, unsaturated polyester	0.6
Polycarbonate	2.2
Polystyrene	1.0
Polymethylmethacrylate (PMMA)	1.7
Polyethylene	
High-density	2.1
Medium-density	5.0
Nylon	2.8
Polyvinyl chloride (PVC)	2.5

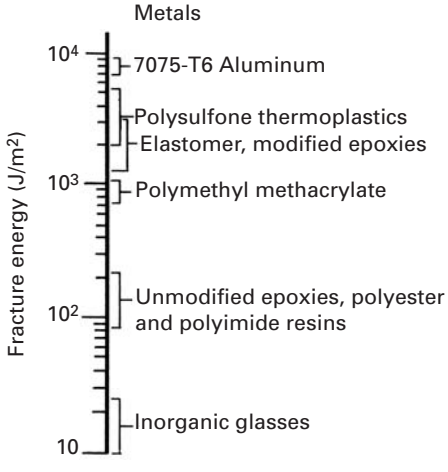

Fig. 8.48 Fracture energy (G_{Ic}) of some common materials. (After R. Y. Ting, in *The Role of Polymeric Matrix in the Processing and Structural Properties of Composites* (New York: Plenum Press, 1983), p. 171.)

Many approaches have been used to improve the toughness of polymers. Alloying or blending a given polymer with a polymer of higher toughness improves the toughness of the polymer. Among the well-known modified thermoplastics are acrylonitrile–butadiene–styrene (ABS) copolymer, high-impact polystyrene (HIPS), and nylon containing a polyolefin. Copolymerization can also lead to improved toughness levels. Generally, thermoplastics are tougher than thermosets, but there are ways to raise the toughness level of thermosets to that of thermoplastics or even higher. One such approach involves the addition of rubbery, soft particles to a brittle thermoset. For example, a class of thermosetting resins that comes close to polysulfones, insofar as toughness is concerned, is the elastomer-modified epoxies. Elastomer- or rubber-modified thermosetting epoxies make multiphase systems, i.e., a kind of composite. Small (a few micrometers or less), soft, rubbery inclusions distributed in a hard, brittle epoxy enhance its toughness by several orders of magnitude. The methods of incorporation of elastomeric particles can be

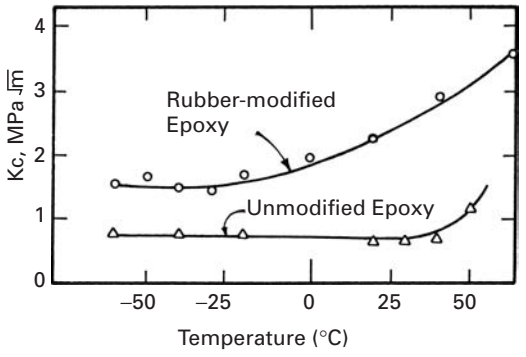

Fig. 8.49 Fracture toughness as a function of temperature of unmodified epoxy and rubber-modified epoxy. (After J. N. Sultan and F. J. McGarry, *Polymer Eng. Sci.*, 13 (1973) 29.)

simple mechanical blending of the soft, rubbery particles and the resin or copolymerization of a mixture of the two. Mechanical blending allows only a small amount (less than 10%) of rubber to be added, whereas larger amounts can be added during polymerization. Figure 8.49 shows toughness as a function of temperature for an unmodified epoxy and a rubber-modified epoxy. Note the higher toughness and enhanced temperature dependence of the rubber-modified epoxy. Epoxy and polyester resins can also be modified by introducing carboxyl-terminated butadiene–acrylonitrile copolymers (CTBNs). Figure 8.50 shows the increase in fracture surface energy of an epoxy as a function of the percent weight of CTBN elastomer. Toughening of glassy polymers by elastomeric additions involves different mechanisms in different polymers. Among the proposed mechanisms for this enhanced toughness are triaxial dilation of the rubber particles at the crack tip, particle elongation, craze initiation, and shear yielding of the polymer.

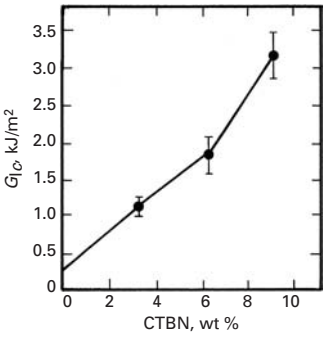

Fig. 8.50 Increase in fracture energy as a function of percent weight of carboxyl-terminated butadiene–acrylonitrile. (After A. K. St. Clair and T. L. St. Clair, *Int. J. Adhesion and Adhesives*, 1 (1981) 249.)

Like the fracture toughness of a metal or a ceramic, the fracture toughness of a polymer is a sensitive function of its microstructure and test temperature. Most polymers, however, are viscoelastic, and this time-dependent property can influence their fracture toughness as well. The data in Table 8.6 were obtained at ambient temperature, and we see that the toughness range for polymers is 1–5 MPa $m^{1/2}$ compared to 10–100 MPa $m^{1/2}$ for metals and 1–10 MPa $m^{1/2}$ for ceramics. In an elastic or time-independent material, fracture toughness is independent of the crack velocity; in a viscoelastic or time-dependent material, steady-state crack growth can occur at an applied stress intensity that is less than the critical value. Figure 8.51(a) shows this schematically, while Figure 8.51(b) shows an actual curve of stress intensity versus crack velocity for PMMA. Note that the data are plotted on a log–log scale. A semilog plot of the same curve for PMMA to much higher crack velocities is shown in Figure 8.52. The same trend is observed in metals, where the yield stress increases with strain rate.[12]

[12] M. A. Meyers, *Dynamic Behavior of Materials* (New York: J. Wiley, 1994).

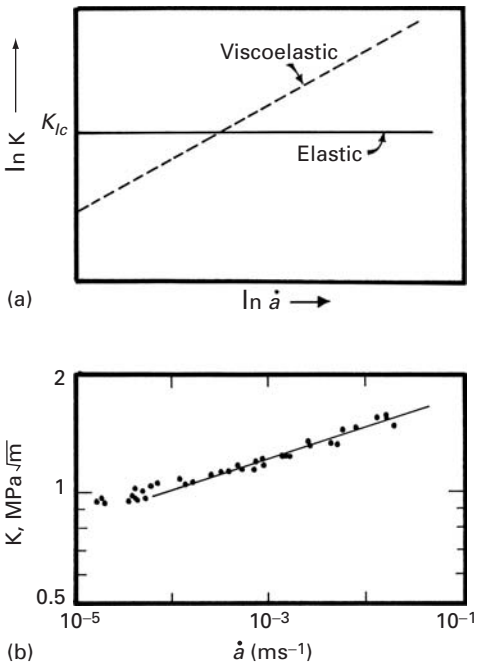

Fig. 8.51 (a) Variation of stress intensity (ln K) as a function of crack velocity (ln $\dot{a}$) for an elastic and viscoelastic material. (b) Stress intensity (K) vs. crack velocity (ln $\dot{a}$) for PMMA. K_{Ic} corresponds to a crack velocity of several hundred m s^{-1}. (After G. P. Marshall, L. H. Coutts, and J. G. Williams, *J. Mater. Sci.*, 9 (1974) 1409.)

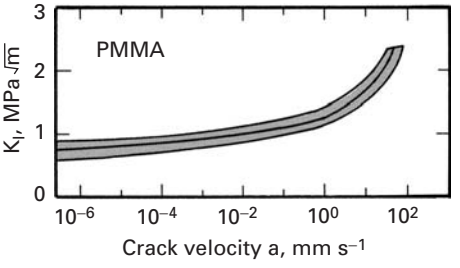

Fig. 8.52 Variation of stress intensity factor with crack velocity in PMMA. (After W. Döll, *Advances in Polymer Science* (Berlin: Springer-Verlag, 1983), p. 119.)

Example 8.2

Describe how the phenomenon of crazing can be exploited to improve the toughness of a polymer.

Answer: Craze formation requires energy. Thus, if we increase the number of crazes nucleated, but do not allow them to grow to fracture, we can improve the toughness of a polymer. Such a mechanism is made use of in acrylonitrile butadiene styrene (ABS), which has a much higher toughness than polystyrene (PS). The acrylonitrile and styrene form a single-phase copolymer. Butadiene is dispersed in this copolymer matrix as elastomeric particles. These particles have a layer of styrene–acrylonitric grafted onto them. Thus, ABS has a two-phase structure. When ABS is stressed, crazes nucleate at rather low strains at the elastomer–styrene interface. However, the high extensibility of

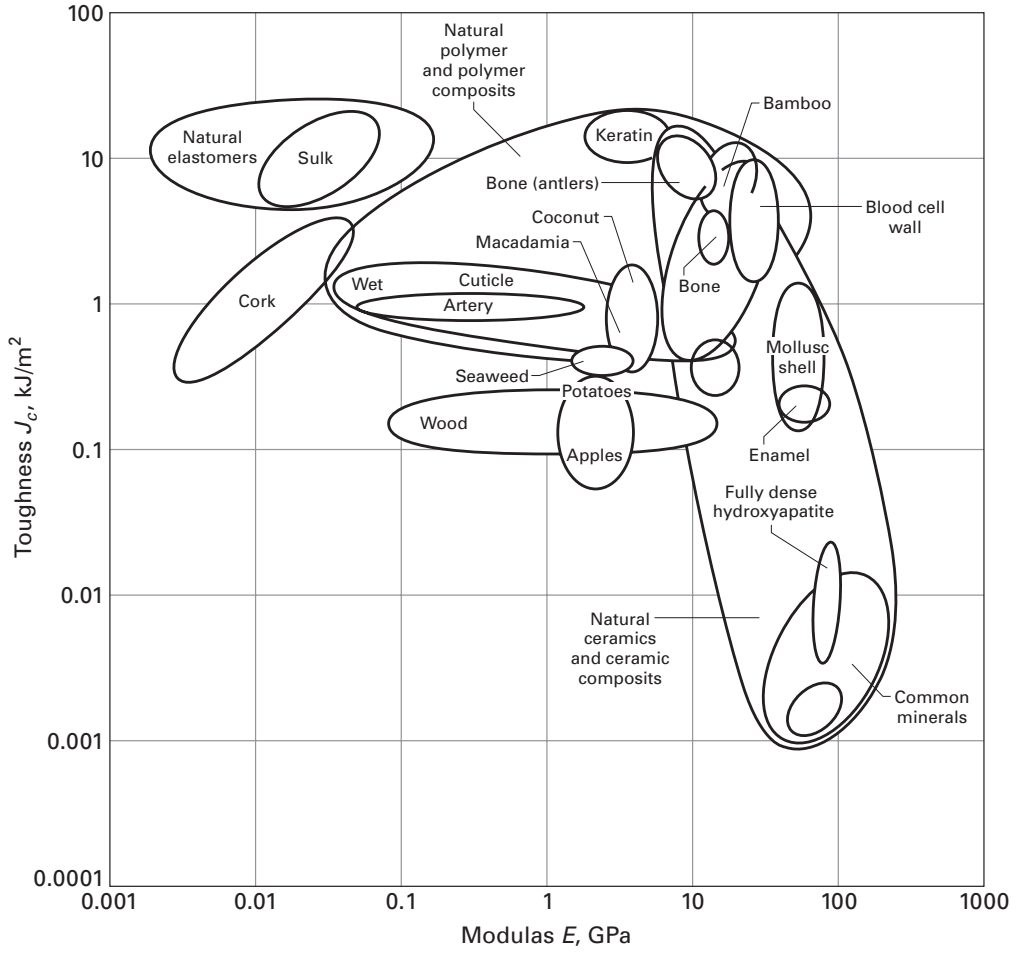

Fig. 8.53 Toughness of biological materials as a function of strength; fracture toughness $K_{Ic}=(EJ_{IC})^{1/2}$. (Courtesy of M. F. Ashby.)

elastomeric particles inhibits the growth of these crazes. A small and uniform particle size aids in producing a high density and an even distribution of crazes in ABS. The reader can easily verify this phenomenon by bending a thin strip of ABS. It will become white, called *stress whitening*, due to the formation of a large number of crazes.

8.5 Fracture and Toughness of Biological Materials

Figure 8.53 provides the fracture toughness (J_c) for a number of biological materials as a function of elastic modulus. The square of fracture toughness (K_c) can be obtained by multiplying J_c by the Young modulus. (See Section 7.7.5.) Figure 8.53 provides a valuable insight into the toughness of biological materials. For instance, shells have a toughness much superior to calcite, although the composition is similar. This is because shells are a composite of calcium carbonate and a thin organic glue layer.

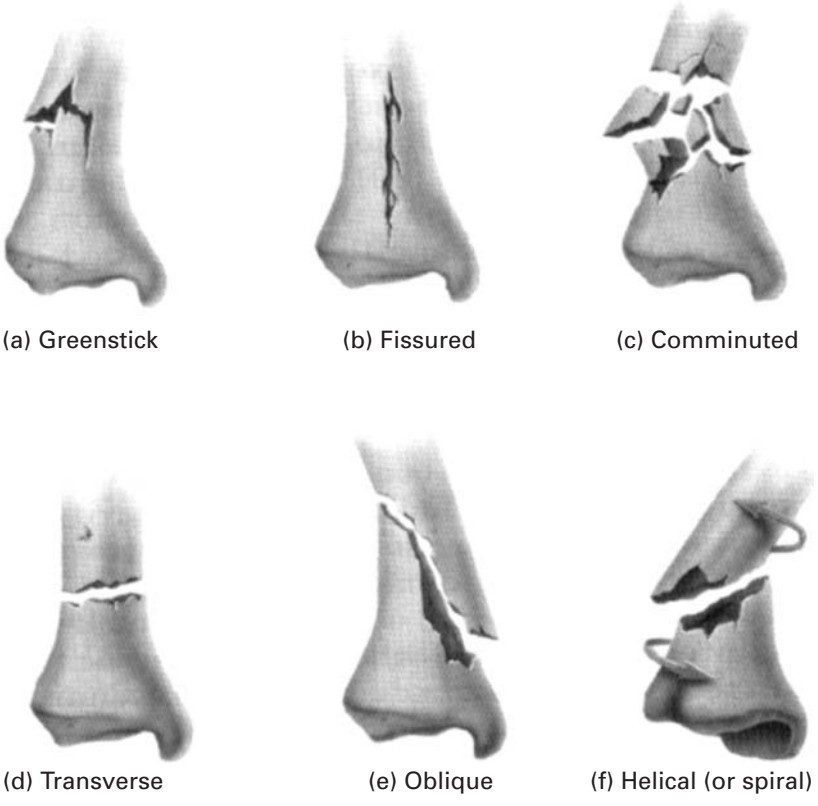

Fig. 8.54 Six modes of fracture in bone. (Adapted from S. J. Hall, *Basic Biomechanics*., 4th ed. (Boston: McGraw Hill, 2003), p. 102.)

Of extreme importance is the fracture and fracture prevention in bone. We know that bone strength decreases as porosity increases. This is one of the changes undergone by bone with aging. There are many fracture morphologies in bone, depending on the loading stresses, rate of loading, and condition of bone. Figure 8.54 presents some of these modalities.

(**a**) **Greenstick fracture**: This occurs in young bone, that has a large volume fraction of collagen, and can break as a green twig. This zig-zag fracture indicates a high toughness.

(**b**) **Fissured fracture**: This corresponds to a longitudinal crack in bone.

(**c**) **Comminuted fracture**: In this many fragments are formed. This is typical of a fracture caused by impact at high velocities. Two factors play a key role. As the velocity of projectile is increased, its kinetic energy increases. This energy is transferred to the bone. The second factor is that at high rates, many cracks are produced simultaneously; they can grow independently until their surfaces intersect. This is the reason why a glass, when thrown on the ground violently, shatters into many small fragments. An additional reason is that the bone becomes stiffer and more brittle as the strain rate is increased.

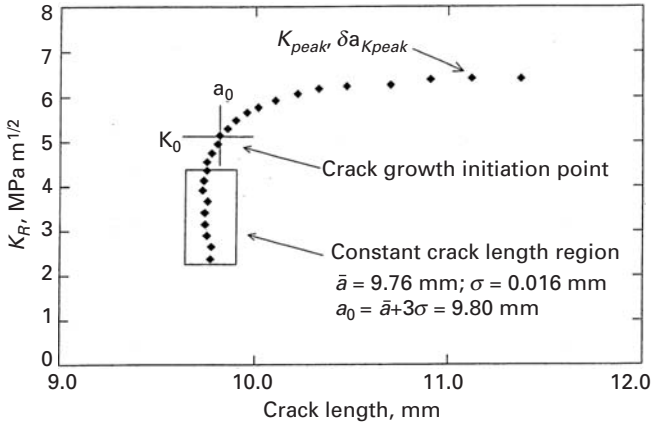

Fig. 8.55 Crack resistance curve as a function of length for horse bone. (From C. L. Malik, J. C. Gibeling, R. B. Martin, and S. M. Stover, "R-Curve Fracture Mechanics of Equine Cortical Bone," *J. Biomech*., 36 (2003) 191.)

(**d**) **Transverse fracture**: This is a complete fracture approximately normal to the axis of the bone.

(**e**) **Oblique fracture**: This is a complete fracture oblique to the bone axis.

(**f**) **Helical fracture**: This fracture, which is also called spiral, is caused by torsional stresses.

The curious student should take a piece of chalk and twist it with her hands. A beautiful helical fracture will result. This type of fracture is known, in the medical community, as spiral. However, this name is not correct, and a helix describes the crack trajectory better than a spiral. Chapter 2 (Example 2.6) provides more information.

Biological materials such as bones and teeth also can be characterized by means of fracture mechanics parameters. For instance, Malik and coworkers[13] studied the fracture toughness of the leg bones (third metacarpal bone) in horses and found that fracture toughness increased with crack length. This behavior is similar to ceramic matrix composites. This increase in fracture toughness with crack growth in ceramic matrix composites is indicative of mechanisms of toughening in the material that are due to the existence of the reinforcing and matrix component. Microcracks in the ceramic phase can produce a decrease in overall stress concentration.

When the fracture toughness is dependent on crack size, linear elastic fracture mechanics cannot be applied and one has to apply other testing methods, such as R curve. In the case of horse leg bone, it was found that there was debonding along macroscopic lamellar structures ahead of the crack, leading to crack deflection, crack energy absorption, and toughening as the crack grew. Figure 8.55 shows the increase in K_R with crack length. For an initial crack length of 9.76 mm, the initial value of the toughness is 5 MPa m$^{1/2}$. The toughness increases to >6 MPa m$^{1/2}$ with increasing crack length.

[13] C. L. Malik, J. C. Gibeling, R. B. Martin, and S. M. Stover, *J. Biomech*., 36 (2003) 191.

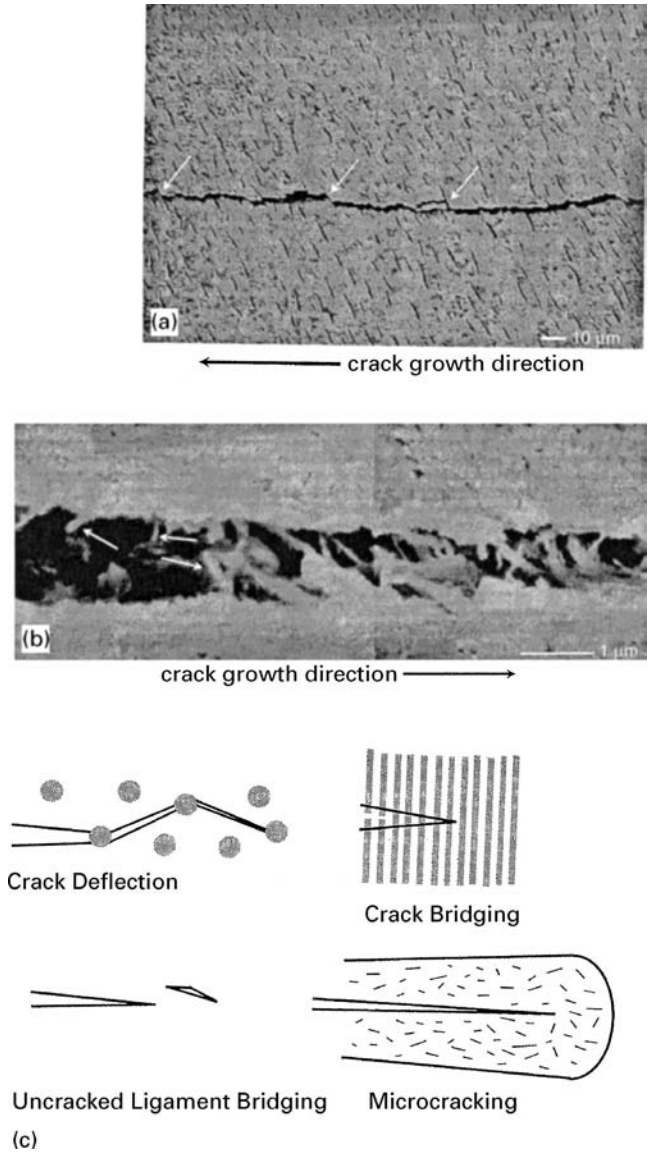

Fig. 8.56 (a) Microcracks in wake of crack and deflection of crack plane by microcracks; (b) bridging behind crack by collagen ligaments; (c) schematic showing four mechanisms contributing to toughening in dentin. (From R. K. Nalla, J. H. Kinney, and R. O. Ritchie, *Biomaterials*, 24 (2003) 3955.)

Several mechanisms of toughening can be identified in dentin, the major component of teeth. Dentin is a composite consisting of nanosized apatite crystals and collagen. The structure is characterized by tubules, which are hollow tubes with a diameter of approximately 1 μm (in elephant tusk). In human teeth, the tubules are similar but have a circular, not elliptical, cross section.

The crack propagation is affected by microcracks produced during loading. Figure 8.56(a) shows microcracks forming a regular pattern and contributing to an irregular crack path. The areas where the crack front was affected by existing microcracks is marked by arrows. These microcracks form ahead of the crack tip and would, at first sight, be considered a weakening mechanism. However, they toughen brittle

materials by delocalizing the stresses. Another toughening mechanism that was identified was the bridging of the crack by collagen fibers. This is shown in Figure 8.56(b). Figure 8.56(c) shows a schematic of the four toughening mechanisms thought to operate in dentin.

8.6 Fracture Mechanism Maps

Data presented in the form of mechanism maps can be very useful, in as much as such maps organize information that is widely scattered in a variety of sources. The idea of mechanism maps is just an extension of the concept of phase diagrams in alloy chemistry, in which different phases coexisting in multicomponent systems are represented as a function of composition and temperature.

Fracture mechanism maps provide information about mechanical properties in a compact form. With these maps, one can plot normalized tensile strength σ/E against the homologous temperature T/T_m. Regions of different types of fracture are classified on the basis of fractography, or fracture–time or fracture–strain studies. Figure 8.57 shows examples of fracture mechanism maps. Such maps can be developed for metals (see Figure 8.57(a) for nickel), ceramics (see Figure 8.57(b) for alumina), and polymers. One can also plot stress intensity factor against temperature and obtain information about crack growth during the fracture process.

Suggested Reading

M. F. Ashby, *Materials Selection in Mechanical Design*, 2nd ed. Oxford: Elsevier, 1999.

Exercises

8.1 In Figure 8.6, mechanical twinning has generated microcracks that, in subsequent tensile tests, weakened the specimen. The ultimate tensile strength of tungsten is 1.2 GPa, and its fracture toughness is approximately 70 MPa $m^{1/2}$. By how much is the fracture stress decreased due to the presence of the microcracks?

8.2 Explain why FCC metals show a ductile fracture even at low temperatures, while BCC metals do not.

8.3 Show, by a sequence of sketches, how the neck in pure copper and in copper with 15% volume fraction of a second phase will develop. Using values from Figure 8.17, show the approximate configuration of the final neck.

8.4 Alumina specimens contain flaws introduced during processing; these flaws are, approximately, equal to the grain size. Plot the fracture stress vs. grain size (for grains below 200 μm), knowing that the fracture toughness for alumina is equal to 4 MPa $m^{1/2}$. Assume $Y = 1$.

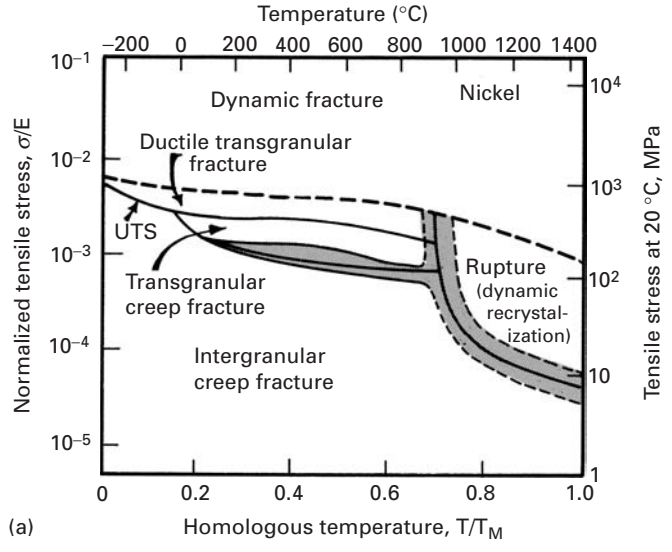

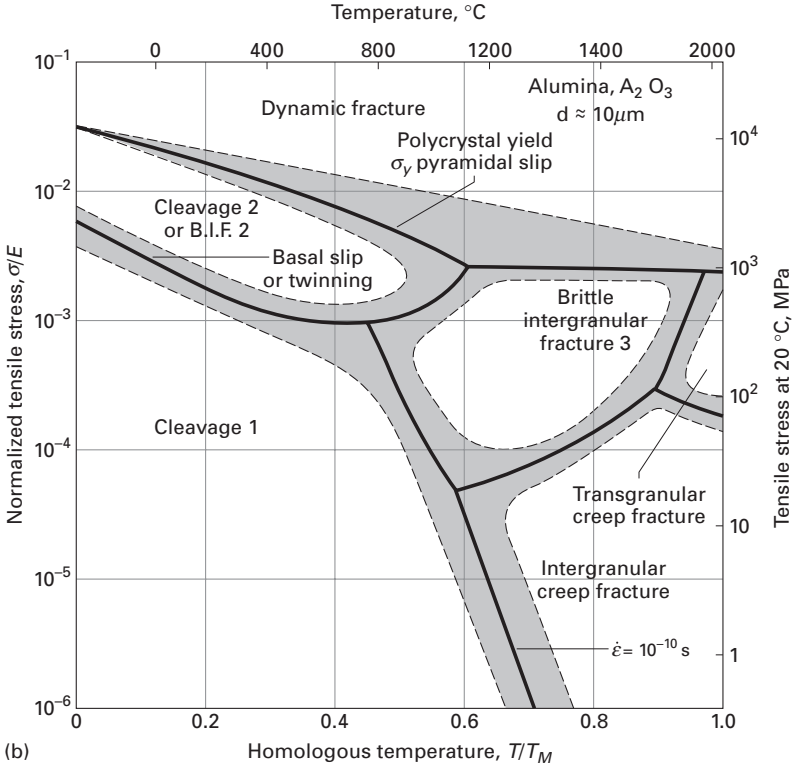

Fig. 8.57 (a) Fracture mechanism map for nickel tested in tension; shading indicates a mixed mode of fracture. (Adapted from M. F. Ashby, C. Gandhi, and D. M. R. Taplin, *Acta Met.*, 27 (1979), 699.) (b) Fracture mechanism map for alumina with grain size of 10 μm. (Adapted from C. Gandhi and M. F. Ashby, *Acta Met.*, 27 (1979), 1565.)

8.5 Calculate the theoretical cleavage stress for sapphire (monocrystalline Al_2O_3) along its four crystallographic orientations. (See Table 8.5.)

8.6

(a) Calculate the compressive strength for a ceramic containing crack of size 100 μm. Let μ be the coefficient of friction between the flaw walls and ℓ

be the length of the cracks generated at the ends of an existing flaw. (See Figure 8.36.) Assume that the onset of failure corresponds to a value of $\ell = 2a$ and that $\mu = 1$, and that $K_{Ic} = 4$ MN m$^{1/2}$.

(b) Compare the tensile strength with the compressive strength that you obtained in part (a).

8.7 A ceramic with $K_{Ic} = 4$ MPa m$^{1/2}$ contains pores with radius $a = 5$ μm due to incomplete sintering. These pores lead to a decrease in the failure stress of the material in both tension and compression. One in every ten grain-boundary junctions contains a void; the grain size of the ceramic is 50 μm. The ceramic fails in compression when the length ℓ of each crack generated at the voids equals one-half of the spacing between the voids.

(a) Determine the compression strength of the ceramic, using the equation from Sammis and Ashby.

(b) Determine the tensile strength of the ceramic, assuming flaws with size a.

8.8 Using the micrographs of Figure 8.31, establish, for Al_2O_3 ($K_{Ic} = 2.5$ MPa m$^{1/2}$), (a) the strength in compression, using the Sammis–Ashby equation from the previous problem, and (b) the tensile strength.

8.9 Tempering is the treatment given to flat glass (e.g., the glass window in the oven in your kitchen) by quenching the glass in a suitable liquid. Draw schematically the stress distribution in such a glass as a function of the thickness of a glass sheet. Discuss the significance of the stress distribution obtained in tempered glass.

8.10 Estimate the internal thermal stress generated in a polycrystalline sample of titanium dioxide for $\Delta T = 1{,}000$ °C. Young's modulus for $TiO_2 = 290$ GPa, and the expansion coefficients along the direction a and c are:

$$\alpha_a = 6.8 \times 10^{-6}\,\mathrm{K}^{-1},$$
$$\alpha_c = 8.3 \times 10^{-6}\,\mathrm{K}^{-1}.$$

Assume $K_c = \sigma\sqrt{\pi a}$.

8.11 Si_3N_4 has a surface energy equal to 30 J/m^2 and an atomic spacing $a_0 \approx 0.2$ nm. Calculate the theoretical strength of this material (see Chapter 7), and compare the value you get with the one experimentally observed in tension testing ($\sigma = 550$ MPa). Calculate the flaw size that would cause this failure stress.

8.12 The theoretical density of a polymer is 1.21 g cm^{-3}. By an optical technique, it was determined that the crazed region in this polymer had 40% porosity. What is the density of the crazed region? Can you estimate the elastic modulus of the crazed region as a percentage of the modulus of the normal polymer?

8.13 A polycarbonate sample showed a craze growth length and time relationship of

$$\ell = k \log(t/t_0),$$

where ℓ is the craze length at time t, t_0 is the time crazing is initiated after the application of the load, and k is a constant. For a given temperature and

stress, find the rate of craze growth. Comment on the implications of the relationship that you obtain.

8.14 Craze formation is a plastic deformation mechanism that occurs without lateral contraction. What can you say about the Poisson ratio of the crazed material?

8.15 The *Titanic* sank on April 14–15, 1912 after hitting an iceberg. Ironically, this ship had been dubbed the "Unsinkable." This was a tremendous shock. In 1985, the wreck was discovered and explored. Why did the 46,000-ton ship sink in less than three hours?

Hint: Entire hull steel plates littered the bottom of the sea. Metallurgical examinations carried out at NIST revealed that the wrought iron in the rivets that joined the plates contained three times today's allowable amount of slag (the glassy residue left behind after the smelting of ore).

8.16 The famous accident of the NASA *Challenger* space shuttle that occurred on a cold night was caused by a faulty O-ring. Explain the accident.

8.17 Describe the microscopic processes that take place during ductile and brittle fracture. What are the differences in appearance of these fractures?

8.18 Figure 8.10 shows *r*-type cavities nucleated at grain boundaries in copper. Assuming that the applied stress is in the vertical direction, make a sketch of the consecutive events that would occur along the grain boundaries.

8.19 At a homologous temperature (T/T_m) of 0.6, describe the fracture mechanism changes that alumina would undergo as the normalized stress is increased from 10^{-5} to 10^{-3}. Use the fracture mechanism map for alumina (Figure 8.57(b)) to answer this question.

Chapter 9

Fracture Testing

9.1 Introduction

Fracture of any material (be it a recently acquired child's toy or a nuclear pressure vessel) is generally an undesirable happening, resulting in economic loss, an interruption in the availability of a desired service, and, possibly, damage to human beings. Besides, one has good, technical reasons to do fracture testing: to compare and select the toughest (and most economical material) for given service conditions; to compare a particular material's fracture characteristics against a specified standard; to predict the effects of service conditions (e.g., corrosion, fatigue, stress corrosion) on the material toughness; and to study the effects of microstructural changes on material toughness. One or more of these reasons for fracture testing may apply during the design, selection, construction, and/or operation of material structures. There are two broad categories of fracture tests; qualitative and quantitative. The Charpy impact test exemplifies the former, and the plane-strain fracture toughness (K_{Ic}) test illustrates the latter. We describe briefly important tests in both of these categories.

9.2 Impact Testing

We saw in Chapter 7 that stress concentrations, like cracks and notches, are sites where failure of a material starts. It has been long appreciated that the failure of a given material in the presence of a notch is controlled by the material's fracture toughness. Many tests have been developed and standardized to measure this "notch toughness" of a material. Almost all are qualitative and comparative in nature. As pointed out in Chapter 7, a triaxial stress state, high strain rate, and low temperature all contribute to a brittle failure of the material. Thus, in order to simulate most severe service conditions, almost all of these tests involve a notched sample, to be broken by impact over a range of temperatures.

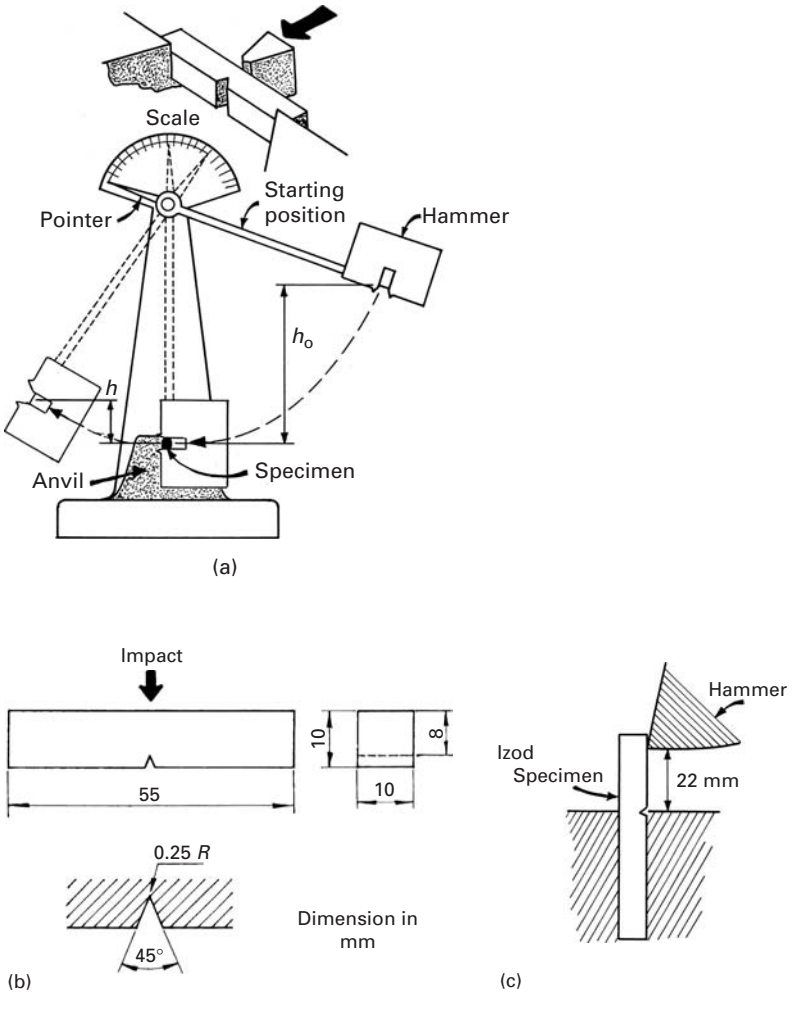

Fig. 9.1 (a) Charpy impact testing machine. (b) Charpy impact test specimen. (c) Izod impact test specimen.

9.2.1 Charpy Impact Test

The Charpy V-notch impact test is an ASTM standard. The notch is located in the center of the test specimen, which is supported horizontally at two points. The specimen receives an impact from a pendulum of a specific weight on the side opposite that of the notch (Figure 9.1). The specimen fails in flexure under impact.

The energy absorbed by the specimen when it receives the impact from the hammer is equal to the difference between the potential energies of the hammer before and after impact. If the hammer has mass m, then

$$E_f = mg\,(h_0 - h_1)\,,$$

where E_f is the sum of the energy of plastic deformation, the energy of the new surfaces generated, and the vibrational energy of the entire system; h_0 is the initial height of the hammer; h_1 is the hammer's final height; and g is the acceleration due to gravity. Of these, the

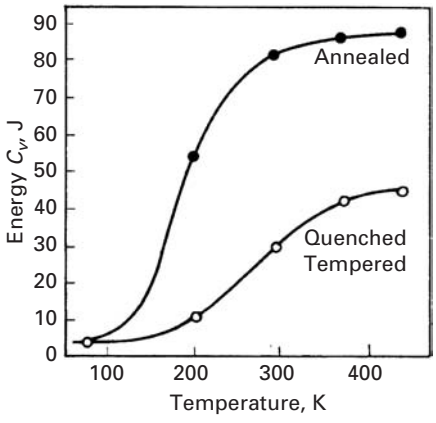

Fig. 9.2 Energy absorbed versus temperature for a steel in annealed and in quenched and tempered states. (Adapted with permission from J. C. Miguez Suarez and K. K. Chawla, *Metalurgia-ABM*, 34 (1978) 825.)

first is the most significant term, and it may be assumed that the Charpy energy is

$$\mathrm{CV} \approx mg\,(h_0 - h_1)\,. \tag{9.1}$$

At impact with the specimen, the hammer has a velocity (the student should consult his or her physics textbook)

$$v = (2gh_0)^{1/2}\,.$$

For a difference in height of 1 m,

$$v = 4.5\,\mathrm{m/s}.$$

If we assume that the average length over which plastic deformation takes place is 5 mm, we have

$$\dot{\varepsilon} = \frac{v}{L} \approx 10^3 s^{-1}.$$

We see, then, that the strain rate in a Charpy test is very high.

In the region around the notch in the test piece, there exists a triaxial stress state due to a plastic yielding constraint there. This triaxial stress state and the high strain rates enhance the tendency toward brittle failure. Generally, we present the results of a Charpy test as the energy absorbed in fracturing the test piece. An indication of the tenacity of the material can be obtained by an examination of the fracture surface. Ductile materials show a fibrous aspect, whereas brittle materials show a flat fracture.

A Charpy test at only one temperature is not sufficient, however, because the energy absorbed in fracture drops with decreasing test temperature. Figure 9.2 shows this variation in the energy absorbed as a function of temperature for a steel in the annealed and in the quenched and tempered states. The temperature at which a change occurs from a high-energy fracture to a low-energy one is called the *ductile–brittle transition temperature* (DBTT). However, since, in practice, there occurs not a sharp change in energy, but instead, a transition zone, it becomes difficult to obtain this DBTT with precision. Figure 9.3 shows how the morphology of the fracture surface changes

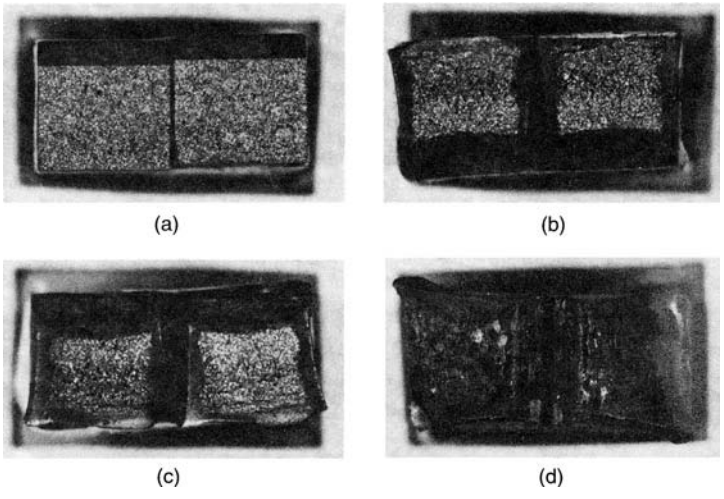

Fig. 9.3 Effect of temperature on the morphology of fracture surface of Charpy steel specimen. Test temperatures $T_a < T_b < T_c < T_d$. (a) Fully brittle fracture. (b, c) Mixed-mode fractures. (d) Fully ductile (fibrous) fracture. Each side of the specimen is 10 mm.

in the transition region. The greater the fraction of fibrous fracture, the greater is the energy absorbed by the specimen. A brittle fracture has a typical cleavage appearance and does not require as much energy as a fibrous fracture. BCC and HCP metals or alloys show a ductile–brittle transition, whereas FCC structures do not. Thus, generally a series of tests at different temperatures is conducted that permits us to determine a transition temperature. This temperature, however arbitrary, is an important parameter in the selection of materials, from the point of view of tenacity, or the tendency of occurrence of brittle fracture. Because the transition temperature is, generally, not very well defined, there exist a number of empirical ways of determining it, based on a certain absorbed energy (e.g., 15 J), change in aspect of the fracture (e.g., the temperature corresponding to 50% fibrous fracture), lateral contraction (e.g., 1%) that occurs at the notch root, or lateral expansion of the specimen. The transition temperature depends on the chemical composition, heat treatment, processing, and microstructure of the material. Among these variables, grain refinement is the only method that results in both an increase in strength of the material in accordance with the Hall–Petch relation and, at the same time, a reduction in the transition temperature (see Section 8.2.2). Heslop and Petch[1] showed that the transition temperature T_c depended on the grain size D according to the formula

$$\frac{dT_c}{d\ln D^{1/2}} = -\frac{1}{\beta},$$

where β is a constant. This is explained by the Armstrong criterion (Section 8.2.3). Thus, a graph of T_c against $\ln D^{1/2}$ will be a straight line with slope $-1/\beta$.

In Figure 9.4, the fraction of the fracture area that is cleavage and the lateral expansion of the Charpy specimen are plotted, in

[1] J. Heslop and N. J. Petch, *Phil. Mag.*, 3 (1958) 1128.

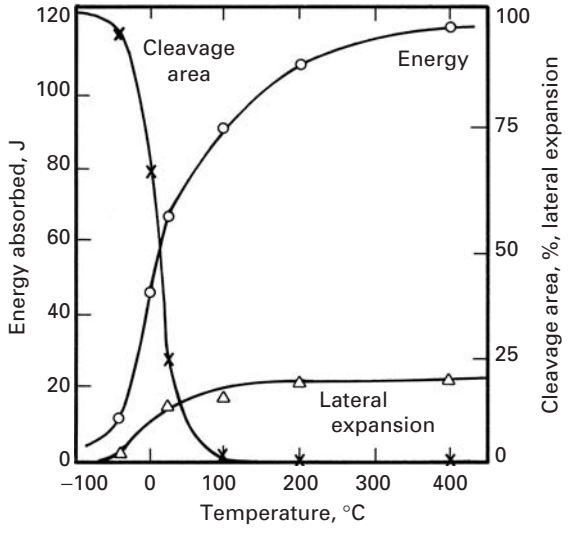

Fig. 9.4 Results of Charpy tests for AISI 1018 steel (cold-drawn).

addition to the energy absorbed by the hammer. The excellent correlation among the three curves is plain, and this test simulates the dynamic response of a metal.

Figure 9.1(c) shows a second specimen geometry also commonly used (especially for plastics) in the same experimental configuration as the Charpy test. It is called the "Izod" specimen. The cross section (10×10 mm) and V-notch geometry of the specimen are identical, but one of the sides is longer. The specimen is held up vertically, and the notch is, in this case, on the same side as the impact.

There is a good "engineering" correlation between Charpy V-notch energy (CVN) and the fracture toughness of some steels in the upper shelf (above the ductile–brittle transition temperature):

$$\left(\frac{K_{Ic}}{\sigma_{ys}}\right)^2 = \frac{5}{\sigma_{ys}}\left(\text{CVN} - \frac{\sigma_{ys}}{20}\right).$$

Like many "engineering" correlations, it is unit dependent. In the equation above, the following units should be used: $K_{Ic} \rightarrow$ ksi.in$^{1/2}$ and $\sigma_{ys} \rightarrow$ ksi, where σ_{ys} is the yield strength. This equation enables us to estimate the fracture toughness (a complicated test) from the Charpy V-notch energy (a simple test).

9.2.2 Drop-Weight Test

The drop-weight test is used to determine a reproducible and well-defined ductile–brittle transition in steels. The specimen consists of a steel plate containing a brittle weld on one surface. A cut is made in the weld with a saw to localize the fracture (Figure 9.5). The specimen is treated as a "simple edge-supported beam" with a stop placed below the center to limit the deformation to a small amount (3%) and prevent general yielding in different steels. The load is applied by means of a freely falling weight striking the side of the specimen opposite to the crack starter. Tests are conducted at 5-K intervals,

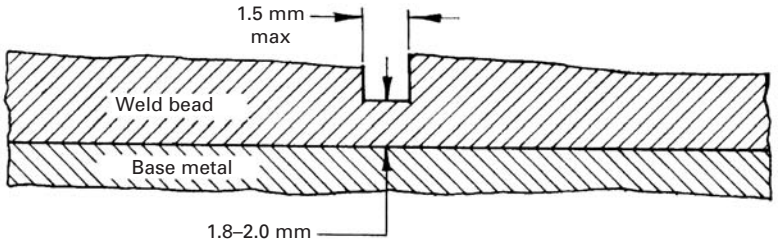

Fig. 9.5 Drop-weight test specimen.

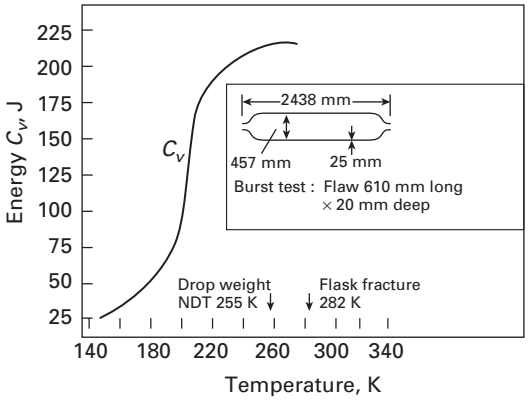

Fig. 9.6 Charpy V-notch curve for a pressure-vessel steel. Note that the NDT temperature determined by the drop-weight test corresponds to the high-toughness region of the Charpy curve. Pneumatic pressurization; material: 2.25 Cr-1 Mo steel, yield stress 590 MPa. (After W. J. Langford, *Can. Met. Quart.*, 19 (1980) 13.)

and a break/no-break temperature, called the *nil ductility transition* (*NDT*) *temperature*, is determined. The NDT temperature is thus the temperature below which a fast, unstable fracture (i.e., brittle fracture) is highly probable. Above that temperature, the toughness of the steel increases rapidly with temperature. This transition temperature is more precise than the Charpy-based transition temperature. The drop-weight test uses a sharp crack that moves rapidly from a notch in a brittle weld material, and thus, the NDT temperature correlates well with the information from a K_{Ic} test, described in Section 9.3. The drop-weight test provides a useful link between the qualitative "transition temperature" approach and the quantitative "K_{Ic}" approach to fracture.

The test affords a simple means of quality control through the NDT temperature, which can be used to group and classify various steels. For some steels, identification of the NDT temperature indicates safe minimum operating temperatures for a given stress. That the drop-weight NDT test is more reliable than a Charpy V-notch value of the transition temperature is illustrated in Figure 9.6 for a pressure-vessel steel. The vessel fractured in an almost brittle manner near its NDT temperature, although, according to the Charpy curve, it was still very tough.

The drop-weight test is applicable primarily to steels in the thickness range 18 to 50 mm. The NDT temperature is unaffected by section sizes above about 12 mm; because of the small notch and the limited

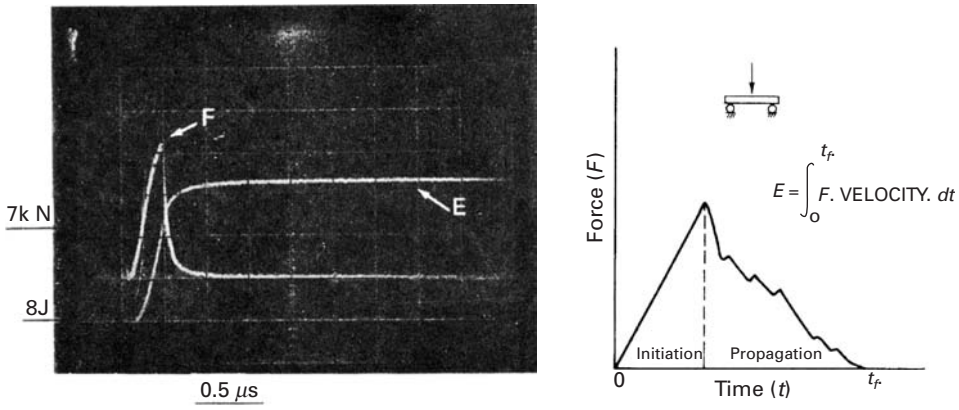

Fig. 9.7 (a) Typical oscilloscope record of an instrumented Charpy impact test. (b) Schematic representation of (a).

deformation due to brittle weld bead material, sufficient notch-tip restraint is ensured.

9.2.3 Instrumented Charpy Impact Test

The Charpy impact test described in Section 9.2.1 is one of the most common tests for characterizing the mechanical behavior of materials. The principal advantages of the test are the ease of preparation of the specimen, the execution of the test proper, speed, and low cost. However, one must recognize that the common Charpy test basically furnishes information of only a comparative character. The transition temperature, for example, depends on the thickness of the specimen (hence, the need to use standard samples); that is, this transition temperature can be used to compare, say, two steels, but it is not an absolute material property. Besides, the common Charpy test measures the total energy absorbed (E_T), which is the sum of the energies spent in initiation (E_i) and in propagation (E_p) of the crack (i.e., $E_T = E_i + E_p$). In view of this problem, a test called the *instrumented Charpy impact test* has been developed. This test furnishes, besides the absorbed energy, the variation in the applied load with time. The instrumentation involves the recording of the signal from a load cell on the pendulum by means of an oscilloscope in the form of a load–time curve of the test sample. Figure 9.7(a) shows a typical oscilloscope record, and Figure 9.7(b) shows a schematic representation of that record. This type of curve can provide information about the load at general yield, maximum load, load at fracture, and so on. The energy spent in impact can also be obtained by integration of the load–time curve. From this curve, one can obtain the energy of fracture if the velocity of the pendulum is known. Assuming this velocity to be constant during the test, we can write the energy of fracture as

$$E' = V_0 \int_0^t P dt, \tag{9.2}$$

where E' is the total fracture energy, based on the constant velocity of the pendulum, V_0 is the initial velocity of the pendulum, P is the instantaneous load, and t is the time.

In fact, the assumption that the velocity of the pendulum is constant is not valid. According to Augland,[2]

$$E_t = E'(1 - \alpha), \tag{9.3}$$

where E_t is the total fracture energy, $E' = V_0 \int_0^t P dt$, $\alpha = E'/4E_0$, and E_0 is the initial energy of the pendulum. The values of total energy absorbed in fracture computed this way from the load–time curves show a one-to-one correspondence with the values determined in a conventional Charpy test. Based on this correspondence, we can use Equation 9.3 for computing the initiation and propagation energies at a given temperature. This information, together with the load at yielding, maximum load, and load at fracture, can allow us to identify the various stages of the fracture process.

It is well known (see Section 9.3) that the plane-strain fracture toughness (K_{Ic}) test gives a much better and precise idea of a material's tenacity than the instrumented Charpy test does. Also, K_{Ic} is a material property. However, as will be seen shortly, the K_{Ic} test possesses certain disadvantages: The preparation of equipment and the specimen is rather expensive, the test is relatively slow and not simple to execute, and so on. Consequently, there have been attempts at developing empirical correlations between the energy absorbed in a conventional Charpy test (CV) and the plane-strain fracture toughness (K_{Ic}). The reader is warned that such correlations are completely empirical and are valid only for the specific metals tested. The instrumented Charpy test, with samples precracked and containing side grooves in order to assure a plane-strain condition, can be used to determine the dynamic fracture toughness K_{ID}. For ultra high-strength metals (σ_y very large), $K_{ID} \approx K_{Ic}$. Thus, we may use the instrumented Charpy test to determine K_{Ic} or K_{ID} for very high-strength steels. But we must check the results obtained with those obtained from a standard ASTM K_{Ic} test, as described in the next section.

9.3 Plane-Strain Fracture Toughness Test

The fracture toughness K_{Ic} of a material may be determined by means of a number of standards, e.g., ASTM 399 or BS 544 for metals. For plastic materials, ASTM D5045–91 gives standard test methods for plane-strain fracture toughness and strain energy release rate. There are different standards for ceramic materials (see Section 9.7). The essential steps in fracture toughness tests involve the measurement of crack extension and load at the sudden failure of the sample. Because it is difficult to measure crack extension directly, one measures the

[2] B. Augland, *Brit. Weld.*, 9 (1962) 434.

relative displacement of two points on opposite sides of the crack plane. This displacement can be calibrated and related to the real crack front extension.

The typical test samples used in fracture toughness tests carried out in accordance with the ASTM standard are shown in Figure 9.8. Figure 9.8(c) shows the size of the specimens. (Tensile and Charpy specimens are also shown for comparison.) The relation between the applied load and the crack opening displacement depends on the size of the crack and the thickness of the sample in relation to the extent of the plastic zones. When the crack length and the sample thickness are very large in relation to the quantity $(K_{Ic}/\sigma_y)^2$, the load–displacement curve is of the type shown in Figure 9.9(a). The load at the brittle fracture that corresponds to K_{Ic} is then well defined. When the specimen is of reduced thickness, a step called "pop-in" occurs in the curve, indicating an increase in the crack opening displacement without an increase in the load (Figure 9.9(b)). This phenomenon is attributed to the fact that the crack front advances only in the center of the plate thickness, where the material is constrained under plane-strain condition. However, near the free surface, plastic deformation is much more pronounced than at the center, and it approaches the conditions of plane stress. Consequently, the plane-strain crack advances much more in the central portion of the plate thickness, and in regions of material near the surfaces of the specimen, the failure eventually is by shear.

When the test piece becomes even thinner, the plane-stress condition prevails, and the load–displacement curve becomes as shown in Figure 9.9(c). To make valid fracture toughness measurements in plane strain, the influence of the free surface, which relaxes the constraint, must be maintained small. This enables the plastic zone to be constrained completely by elastic material. The crack length must also be maintained greater than a certain lower limit.

Figure 9.10 shows the plastic zone at the crack front in a plate of finite thickness. At the edges of the plate ($x_3 \rightarrow \pm B/2$), the stress state approaches that of plane stress. At the center of a sufficiently thick plate, the stress state approaches that of plane strain. This is so because the ε_{33} component of strain is equal to zero at the center, as the material there in that direction is constrained, whereas near the edges the material can yield in the x_3 direction, so ε_{33} is different from zero.

Up to this point, the sample size and the crack length have been discussed in a qualitative way. The lower limits on width, thickness, and crack length all depend on the extent of plastic deformation through the $(K_{Ic}/\sigma_y)^2$ factor. In view of the lack of knowledge about the exact size of the plastic zone for the crack in mode I (the crack opening mode), it is very difficult to determine the lower limits of dimension of the test piece theoretically. These lower limits above which K_{Ic} remains constant are determined by means of trial tests. Samples of dimensions smaller than those limits tend to overestimate the K_{Ic} limit.

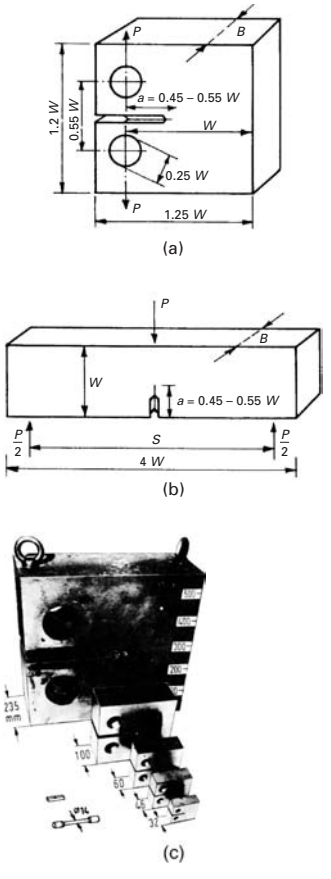

Fig. 9.8 Typical ASTM standard plane-strain fracture toughness test specimens. (a) Compact tension. (b) Bending. (c) Photograph of specimens of various sizes. Charpy and tensile specimens are also shown, for comparison purposes. (Courtesy of MPA, Stuttgart.)

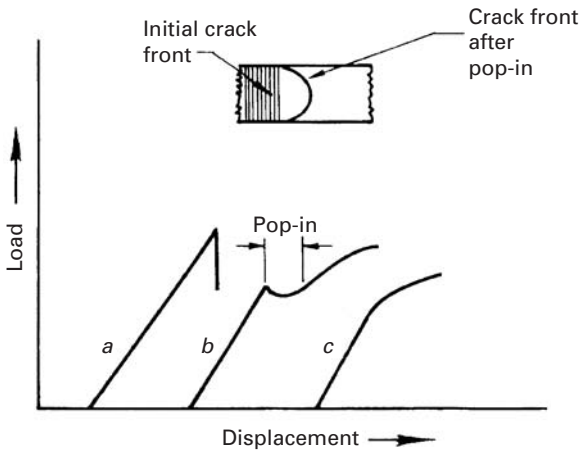

Fig. 9.9 Schematic of typical load–displacement curves in a K_{Ic} test.

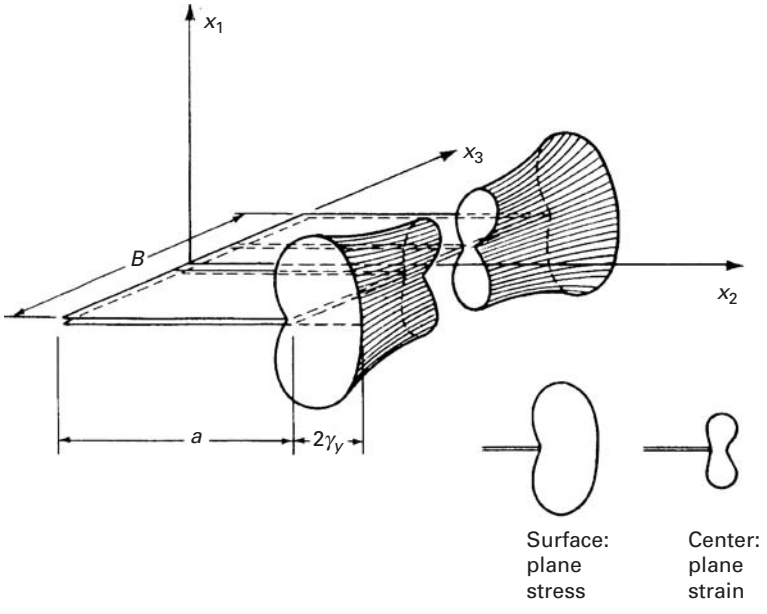

Fig. 9.10 Plastic zone at the crack tip in a plate of finite thickness.

Preferably, in fracture toughness tests, the crack is introduced by fatigue from a starter notch in the sample. The fatigue crack length should be long enough to avoid interference in the crack-tip stress field by the shape of the notch. Under an applied load, the crack opening displacement can be measured between two points on the notch surfaces by various types of transducers. Figure 9.11 shows an assembly for measuring displacement in a notched specimen. Electrical resistance measurements have also been used to detect crack propagation. Calibration curves are utilized for converting displacement measurements and resistance measurements into crack extension.

The load–displacement curves generally show a gradual deviation from linearity, and the "pop-in" step is very small (Figure 9.12). The

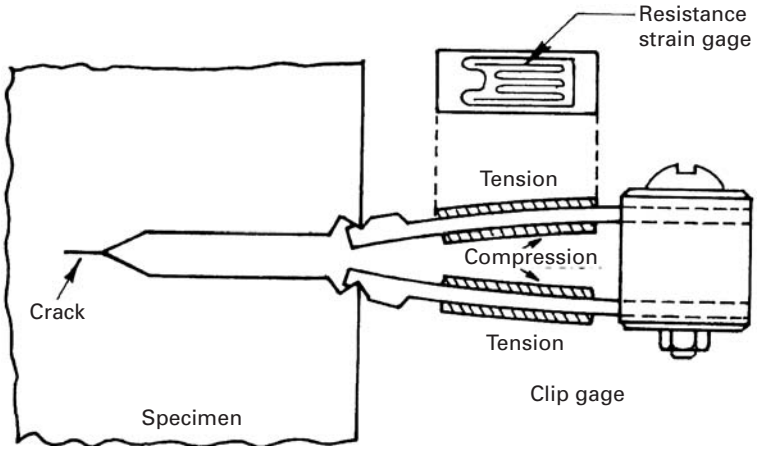

Fig. 9.11 Assembly for measuring displacement in a notched specimen.

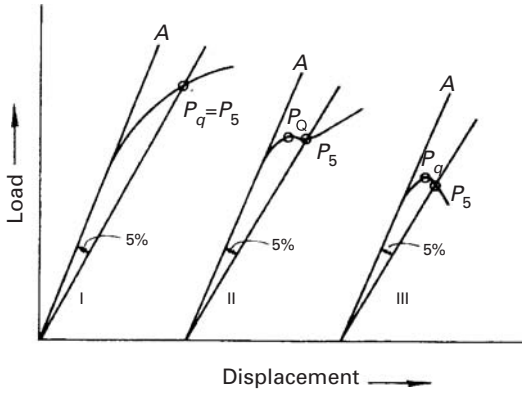

Fig. 9.12 Procedure used for measuring the conditional value K_Q.

procedure used in the analysis of load–displacement records of this type can be explained by means of the figure. Let us designate the linear-slope part as OA. A secant line, OP_5, is drawn at a slope 5% less than that of line OA. The point of intersection of the secant with the load–displacement record is called P_5. We define the load P_Q, for computing a conditional value of K_{Ic}, called K_Q, as follows: If the load on every point of curve before P_5 is less than P_5, then $P_5 = P_Q$ (case I in the figure). If there is a load more than P_5 and before P_5, this load is considered to be P_Q (cases II and III in the figure). In these cases, if $P_{\max}/P_Q > 1.1$, the test is not valid; K_Q does not represent the K_{Ic} value, and a new test needs to be done. After determining the point P_Q, we calculate the value of K_Q according to the known equation for the geometry of the test piece used. A checklist of points is given in Table 9.1 and Figure 9.13 shows schematically the variation of K_c, with the flaw size, specimen thickness, and specimen width. The stress intensity factor is calculated by using the equation

$$K_1 = f\left(\frac{a}{W}\right)\frac{P}{B\sqrt{W}}. \tag{9.4}$$

Table 9.1 | Checklist for the K_{Ic} Test

1. Dimensions of test piece
   a. Thickness, $B \geq 2.5\ (K_{Ic}/\sigma_y)^2$
   b. Crack length, $a \geq 2.5\ (K_{Ic}/\sigma_y)^2$
2. Fatigue precracking
   a. $K_{max}/K_{Ic} \leq 0.6$
   b. Crack front curvature $\leq$ 5% of crack length
   c. Inclination $\leq 10°$
   d. Length between 0.45 W and 0.55 W, where W is the width of the test sample
3. Characteristics of load–displacement curve. This is effectively to limit the plasticity during the test and determines whether the gradual curvature in the load–displacement curve is due to plastic deformation or crack growth.
   a. $P_{max}/P_Q \leq 1.1$

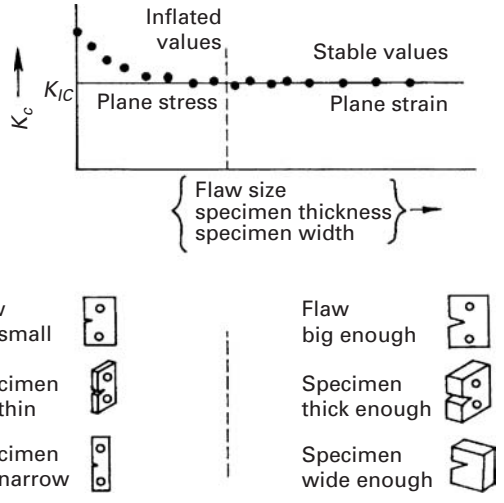

Fig. 9.13 Variation in K_c with flaw size, specimen thickness, and specimen width.

The function $f(a/W)$ has a different form for each specimen geometry. For the compact specimen (Figure 9.8(a)),

$$f\left(\frac{a}{W}\right) = \frac{2+\frac{a}{W}}{\left(1-\frac{a}{W}\right)^{3/2}}\left[0.886 + 4.64\left(\frac{a}{W}\right) - 13.32\left(\frac{a}{W}\right)^2 + 14.72\left(\frac{a}{W}\right)^3 - 5.60\left(\frac{a}{W}\right)^4\right]. \tag{9.5}$$

For the single-edge notched-bend specimen loaded in three-point bending (Figure 9.8(b)),

$$f\left(\frac{a}{W}\right) = \frac{3\frac{S}{W}\sqrt{\frac{a}{W}}}{2\left(1+2\frac{a}{W}\right)\left(1-\frac{a}{W}\right)^{3/2}}\left[1.99 - \frac{a}{W}\left(1-\frac{a}{W}\right)\times\left\{2.15 - 3.93\left(\frac{a}{W}\right) + 2.7\left(\frac{a}{W}\right)^2\right\}\right]. \tag{9.6}$$

The preceding expressions are polynomial fits to functions.

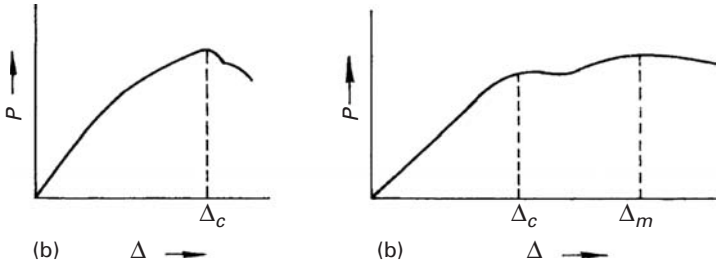

Fig. 9.14 Schematics of load P versus crack opening displacement Δ.

Example 9.1

Estimate the minimum specimen thickness for a valid plane-strain fracture toughness test for material having the following properties:

$$\text{Yield stress } \sigma_y = 400\,\text{MPa},$$
$$\text{Fracture toughness } K_{Ic} = 100\,\text{MPa m}^{1/2}.$$

Solution: The minimum thickness of the specimen is $2.5\,(K_{Ic}/\sigma_y)^2 = 2.5\,(1/4)^2 = 0.156$ m $= 156$ mm.

9.4 Crack Opening Displacement Testing

For crack opening displacement (COD) testing, the test sample for determining δ_c is a slow-bend test specimen similar to the one used for K_{Ic} testing. A clip gage is used to obtain the crack opening displacement. During the test, one obtains a continuous record of the load P versus the opening displacement Δ (Figure 9.14). In the case of a smooth P–Δ curve, the critical value, Δ_c, is the total value (elastic + plastic) corresponding to the maximum load (Figure 9.14(a)). In case the P–Δ curve shows a region of increase in displacement at a constant or decreasing load, followed by an increase in load before fracture, one needs to make auxiliary measurements to determine that this behavior is associated with crack propagation. Should this be so, Δ_c will correspond to the first instability in the curve. If the P–Δ curve shows a maximum, and Δ increases with a reduction in P, then either a stable crack propagation is occurring or a "plastic hinge" is being formed. The "Δ_c" in this case (Figure 9.14(b)) is the value corresponding to the point at which a certain specified crack growth has started. If it is not possible to determine this point, one cannot measure the COD at the start of crack propagation. However, we can measure, for comparative purposes, an opening displacement δ_m, computed from the clip gage output Δ_m, corresponding to the first load maximum. The results in this case will depend on the geometry of the specimen.

Experimentally, we obtain Δ_c, the critical displacement of the clip gage. We need to obtain δ_c, the critical CTOD. Various methods are

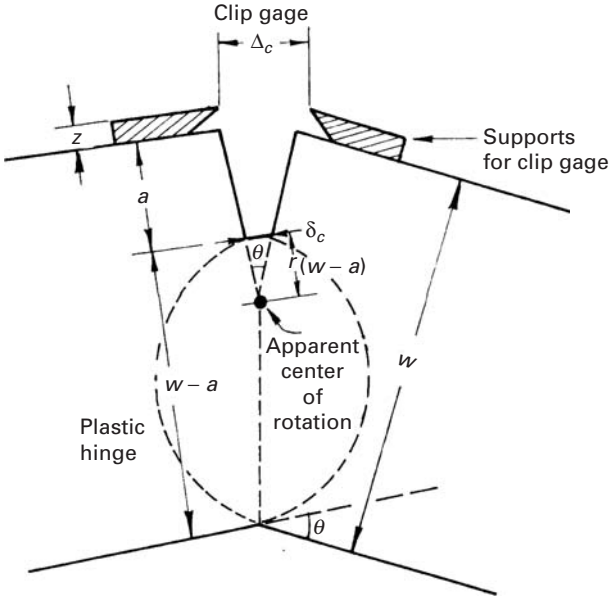

Fig. 9.15 "Plastic hinge" mechanism of deformation.

available, all based on the hypothesis that the deformation occurs by a "hinge" mechanism around a center of rotation at a depth of $r\,(w-a)$ below the crack tip, (Figure 9.15), where w is the width, and a is the length. Experimental calibrations of the crack using specimens of up to 50 mm in thickness, have shown that, for COD in the range 0.0625 to 0.625 mm, δ_c can be obtained to a very good approximation from the relation

$$\delta_c = \frac{(w-a)\,\Delta_c}{w+2a+3z}.$$

This relation is derived on the basis of the assumption that the deformation occurs by a hinge mechanism about a center of rotation at a depth of $(w-a)/3$ below the crack tip (i.e., $r=\frac{1}{3}$). However, r can be smaller for smaller values of Δ_c. Note that $r \approx 0$ in the elastic case (very limited plastic deformation at the crack tip), and $r \approx \frac{1}{3}$ for a totally plastic ligament.

9.5 *J*-Integral Testing

J_{Ic} defines the onset of crack propagation in a material in which large-scale plastic yielding makes direct measurement almost impossible. Thus, one can use *J*-integral testing to find the value of K_{Ic} for a very ductile material from a specimen of dimensions too small to satisfy the requirements of a proper K_{Ic} test.

ASTM standard E819–89 provides a procedure for determining J_c, the critical value of *J*. As pointed out in Chapter 7, the physical interpretation of the *J*-integral is related to the area under the

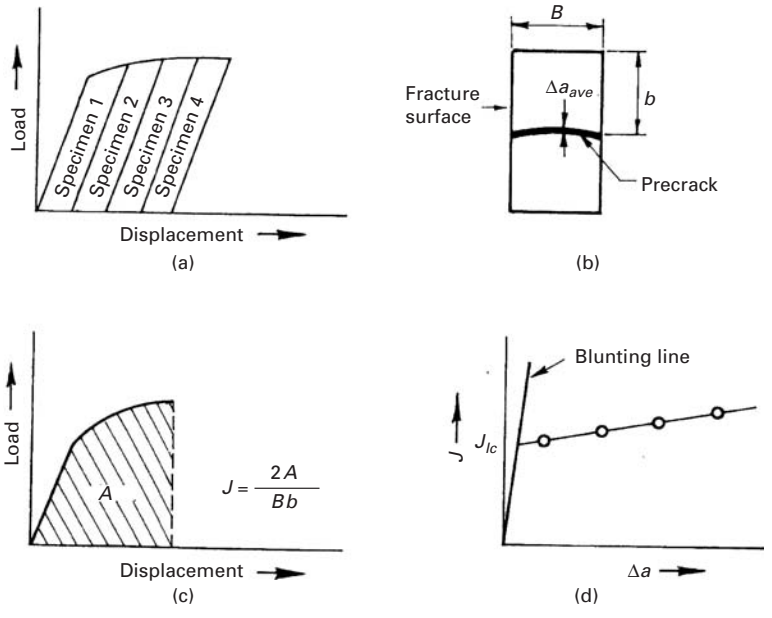

Fig. 9.16 Method for determining J_{Ic}. (a) Load identical specimens to different displacements. (b) Measure the average crack extension by heat tinting. (c) Calculate J for each specimen. (d) Plot J versus Δ_a to find J_{Ic}.

curve of the load versus the load-point displacement for a cracked sample. Both compact tension and bend specimens can be used. The ASTM standard requires at least four specimens to be tested. Each specimen is loaded to different amounts of crack extensions (Figure 9.16). One calculates the value of J for each specimen from the expression

$$J = \frac{2A}{Bb},$$

where A is the area under load versus the load-point displacement curve, B is the specimen thickness, and b is the uncracked ligament. The value of J so derived is plotted against Δa, the crack extension of each specimen. One way of obtaining Δa is to heat-tint the specimen after testing and then break it open. When the specimen is heated, the crack surfaces oxidize. Next, a "best line" through the J points and a "blunting line" from the origin are drawn. This blunting line (indicating the onset of crack blunting due to plastic deformation) is obtained from the equation

$$J = 2\sigma_{\text{flow}}\Delta a, \tag{9.7}$$

where $\sigma_{\text{flow}} = (\sigma_y + \sigma_{UTS})/2$, in which σ_y is the yield stress and σ_{UTS} is the ultimate tensile stress.

The intercept of the J line and the blunting line gives J_{Ic}. J_{Ic} is related to K by

$$J_{Ic} = \frac{K_{Jc}^2}{E}. \tag{9.8}$$

9.6 Flexure Test

The flexure or bend test is one of the easiest tests to do and is very commonly resorted to, especially with brittle materials that behave in a linear elastic manner. A very small amount of material is required, and preparation of the sample is relatively easy. The following assumptions are made in analyzing the flexure behavior of materials. We assume that the Euler–Bernoulli theory is applicable to a freely supported beam. (The beam is not clamped at any point.) That the Euler–Bernoulli theory is applicable means that plane sections remain plane, deformations are small, stress varies linearly with thickness, and there is no Poisson's contraction or expansion. The condition of small deformation comes from the Euler–Bernoulli assumption that the specimen beam is bent into a circular arc. The condition of a small deformation can be easily violated if the material is deformed in a nonlinear, viscoelastic, or plastic manner. Then stress gradients across the vertical section of the beam will not be linear.[3]

The two basic governing equations for a simple beam elastically stressed in bending are

$$\frac{M}{I} = \frac{E}{R} \tag{9.9}$$

and

$$\frac{M}{I} = \frac{\sigma}{y}, \tag{9.10}$$

where M is the applied bending moment, I is the second moment of area of the beam section about the neutral plane, E is Young's modulus of elasticity of the material, R is the radius of curvature of the bent beam, and σ is the tensile or compressive stress on a plane distant y from the neutral plane.

For a uniform circular section of beam,

$$I = \frac{\pi d^4}{64}, \tag{9.11}$$

where d is the diameter of the section.

For a uniform, rectangular section of beam,

$$I = \frac{bh^3}{12} \tag{9.12}$$

where b is the width of the beam and h is the height of the beam.

Bending takes place in the direction of the depth; that is, h and y are measured in the same direction. Also, for a beam with a symmetrical section with respect to the neutral plane, replacing $h/2$ (or $d/2$) for y in Equation (9.10) gives the stress at the beam surface.

[3] The student should recall discussions on beam deflections in courses on mechanics of materials.

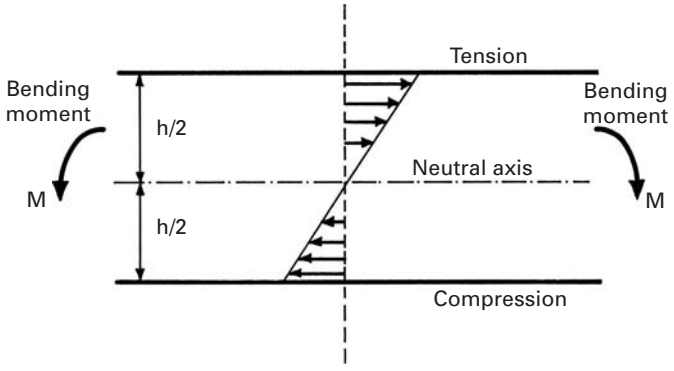

Fig. 9.17 Normal stresses along a section of beam for linearly elastic material.

In the elastic regimen, stress and strain are related by Hooke's law,

$$\sigma = E\,\varepsilon. \tag{9.13}$$

From Equations (9.9), (9.10), and (9.13), we obtain the following simple relation, valid in the elastic regimen:

$$\varepsilon = \frac{y}{R}. \tag{9.14}$$

Figure 9.17 shows the elastic normal stress distribution through the thickness when a beam is bent. The stress and strain vary linearly with the thickness y across the section, with the neutral plane ($y = 0$) representing the zero level. The material on the outside or above the neutral plane of the bent beam is stressed in tension, while that on the inside or below the neutral plane is stressed in compression. Thus, the elastic strain ε in a beam bent to a radius of curvature R varies linearly with distance y from the neutral plane across the beam thickness.

Two main types of flexure tests are three-point and four-point bend tests. Another variant of flexure tests is the so-called interlaminar shear stress (ILSS) that is used in fiber reinforced composites. We describe these briefly.

9.6.1 Three-Point Bend Test

In the three-point bend test, the load is applied at the center point of the beam, and the bending moment M increases from the two extremities to a maximum at the center point. (See Figure 9.18(a).) In this case,

$$M = (P/2)(S/2) = PS/4,$$

while the moment of inertia, for a beam of a rectangular section, is

$$I = bh^3/12.$$

Using Equation 9.10, we can obtain the maximum stress in the outermost layer ($y = h/2$) as

$$\boxed{\sigma_{\max} = 3PS/2bh^2.} \tag{9.15}$$

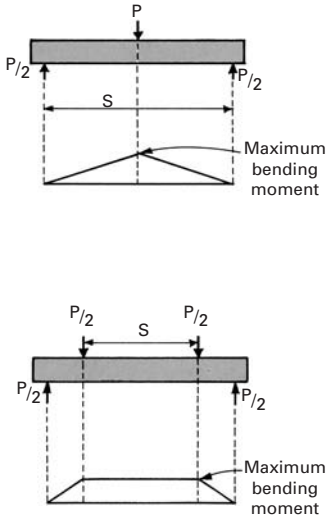

Fig. 9.18 Application of loads and bending moment diagrams for (a) three-point bending and (b) four-point bending tests.

9.6.2 Four-Point Bending

Four-point bending is also called pure bending, since there are no transverse shear stresses on the cross-sections of the beam in the inner span. For an elastic beam bent at four points, the bending moment is constant in the inner span (see Figure 9.18(b)) and is given by

$$M = \frac{\sigma_{\max} I}{h/2} = \frac{P}{2}.\frac{S}{4} \tag{9.16}$$

where I is the moment of inertia, $h/2$ is the distance from the neutral axis to the outer surface, and $\sigma_{\max}$ is the normal stress on a transverse section of the same outer fiber. The maximum stress in a rectangular beam undergoing a four-point bending is

$$\boxed{\sigma_{\max} = 3PS/4bh^2,} \tag{9.17}$$

where S is the outer span and b is the breadth of the beam.

The three- and four-point bending tests are extremely helpful in determining the strength of brittle materials, and especially of ceramics. If brittle materials are tested in tension the alignment of the grips is very critical. Slight misalignments cause major stress inhomogeneities which significantly affect the strength. Flexure tests, on the other hand, are simple and reliable. The four-point bending test presents the following advantage over the three-point bending test: the entire span length is subjected to a constant stress. In a three-point bend, the maximum stress occurs only at the mid-section (see Example 9.2). The resultant strength is called bend strength, flexural strength or, commonly but erroneously, MOR (modulus of rupture). Examples:

Al_2O_3 (99.5% dense)	400 MPa
SiC (hot-pressed)	600 MPa
Soda–lime glass	65 MPa

A systematic comparison of 1,500 sintered alumina specimens (AD-999) with varying dimensions ($3 \times 4 \times 50$ mm and other sizes) revealed that the Weibull modulus was equal to 10 and the characteristic strength of the bend bar was equal to 466 MPa in three-point bending. The four-point bending results were $m = 9.8$ (Weibull modulus) and $\sigma_0 = 374$ MPa. The value of σ_0 corresponds to the 63.2% probability of failure, $(1 - 1/e)$. The four-point bend test results show a lower σ_0 because of a larger surface (and thus a greater probability of flaws $\geq a_c$, the critical length) is subjected to the maximum stress.

A miniaturized bend test was developed for use in small specimens with 3 mm diameter.[4] In this setup, a disk instead of a bar is used. The deflection of specimen is measured with an LVDT (linear variable differential transducer) as it is deformed by a punch. The setup is shown in Figure 9.19.

The maximum stress in the specimen is given by:

$$\sigma = \frac{3P}{2\pi t^2}\left[1 + (1+\nu)\ln\frac{R}{r'}\right],$$

[4] H. Li, F. C. Chen, and A. J. Ardell, *Met. Trans A*, 22 (1991) 2061.

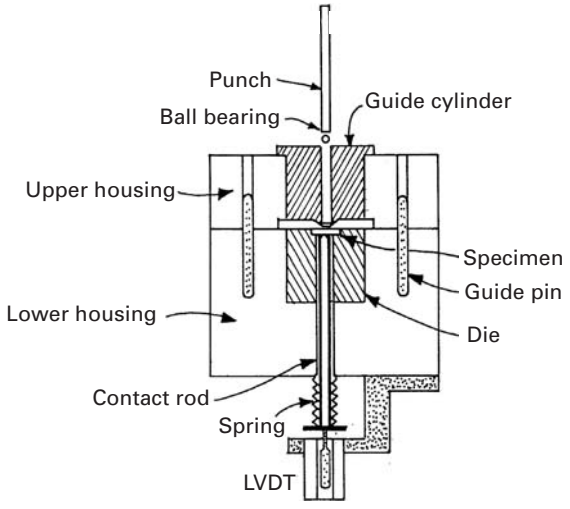

Fig. 9.19 Chematic drawing of the miniaturized disk-bend test. (Adapted from H. Li, F. C. Chen, and A. J. Ardell, *Met. Trans A*, 22 (1991) 2061.)

where P is the load, t is the specimen thickness, R is the radius of the lower supporting die (smaller than 3 mm), r is the radius of the contact area between the ball at the tip of the punch and the specimen, and r' has one of the values:

$$r' = (1.6r^2 + t^2) - 0.675t \quad \text{if} \quad r \leq t/2$$

and

$$r' = r \quad \text{if} \quad r > t/2.$$

This miniaturized bend test can be used on ductile or brittle materials and is well suited when material is available in small sizes.

9.6.3 Interlaminar Shear Strength Test

The interlaminar shear strength test is also known as the short-beam shear test. It is commonly used with fiber reinforced composites, with the fiber length parallel to the length of a three-point bend bar. In such a test, the maximum shear stress occurs at the midplane and is given by

$$\boxed{\tau_{\max} = \frac{3P}{4bh}.} \tag{9.18}$$

The maximum tensile stress occurs at the outermost surface and is given by Equation 9.15. Dividing Equation 9.18 by Equation 9.15, we get

$$\boxed{\frac{\tau_{\max}}{\sigma_{\max}} = \frac{h}{2S}.} \tag{9.19}$$

Equation 9.19 says that if we make the load span S very small, we can maximize the shear stress τ so that the specimen fails under shear with a crack running along the midplane. Thus, if we deliberately make the span very small (hence the name, "short beam"), then it is likely that failure will occur under shear. A word of caution is in order about the interpretation of this test: The test becomes invalid

if the fibers fail in tension before shear induced failure occurs. The test will also be invalid if shear and tensile failure occur simultaneously. It is advisable to examine the fracture surface after the test, to make sure that the crack is along the interface and not through the matrix.

Example 9.2

In a three-point bend test (see Figure E9.2), the specimen has a span of 50 mm and a load P of 50 N. The width and height are 5 mm each. Draw the moment and shear force diagrams. Find the maximum moment and maximum stress.

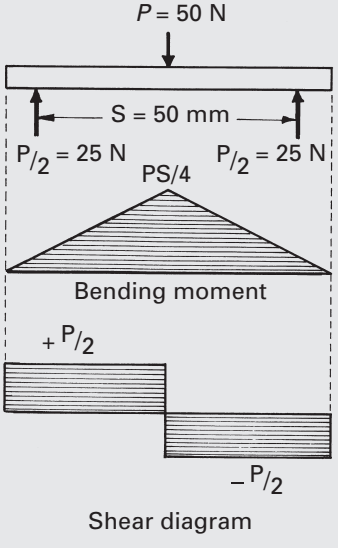

Fig. E9.2

Solution: We have

$$\text{Load, } P = 50\,\text{N}, \quad \text{Span, } S = 50\,\text{mm} = 50 \times 10^{-3}\,\text{m}.$$

In three-point bending, the maximum bending moment occurs at the midpoint of the beam and is given by

$$\frac{P}{2} \times \frac{S}{2} = \frac{PS}{4} = \frac{50\,\text{N} \times 50 \times 10^{-3}\,\text{m}}{4} = 625 \times 10^{-3}\,\text{N} \cdot \text{m}.$$

Note that the maximum stress also occurs along the centerline of the specimen; that is, the whole of the specimen is not subjected to a uniform stress, as would be the case in a tensile test. We have

$$\text{Maxinum stress (Equation 9.15)} = \frac{3 \cdot PS}{bh^2} = \frac{3 \cdot 50 \times \left(50 \times 10^{-3}\right)}{5 \times 10^{-3}\left(5 \times 10^{-3}\right)^2}$$
$$= 60\,\text{MPa}.$$

Example 9.3

It is generally known that a given material will show a higher strength in a three-point bend test than in an axial tension test. Consider a rod of a square cross section and side a. If the span in the bend test is S, show that the ratio of the bend strength to the tensile strength is

$$\sigma_{\text{bend}}/\sigma_{\text{ten}} = 3S/2a.$$

Solution: For uniaxial tension:

$$\text{Force} = P,$$
$$\text{Cross-sectional area} = a^2,$$
$$\text{Tensile strength } \sigma_{\text{ten}} = P/a^2.$$

For three-point bending:
The maximum stress in three-point bending is $\sigma_{\text{bend}} = \sigma_{\max} = M_{\max} y_{\max}/I$, where

$$I = bh^3/12 = a^4/12,$$
$$M = PS/4,$$
$$y_{\max} = a/2.$$

Hence,

$$\frac{\sigma_{\text{bend}}}{\sigma_{\text{ten}}} = \frac{PS}{4} \times \frac{a}{2} \times \frac{12}{a^4}, \frac{a^2}{P} = \frac{3S}{2a}.$$

Thus, the maximum stress in bending is $3S/2a$ times the tensile stress. Generally, $S \gg a$, so the difference can be very large indeed!

9.7 Fracture Toughness Testing of Brittle Materials

In brittle materials – especially ceramics – the strength is largely determined by the size and sharpness of flaws and by the resistance of cracks to propagation. Since plasticity is very limited in such materials, the size of the specimen can be reduced much more than in metals. Recall that the thickness B of the test specimen should exceed $2.5(K_{Ic}/\sigma_y)^2$. This ensures a plastic zone size that is small with respect to B, and therefore, the state of plane strain can be assumed. We will estimate the minimum acceptable specimen thickness for a typical ceramic, alumina, for which

$$K_{Ic} \approx 4\,\text{MPa}\,\text{m}^{1/2},$$
$$\sigma \approx 400\,\text{MPa}.$$

For this specimen,

$$B \geq 2.5 \times 10^{-4}\,\text{m}.$$

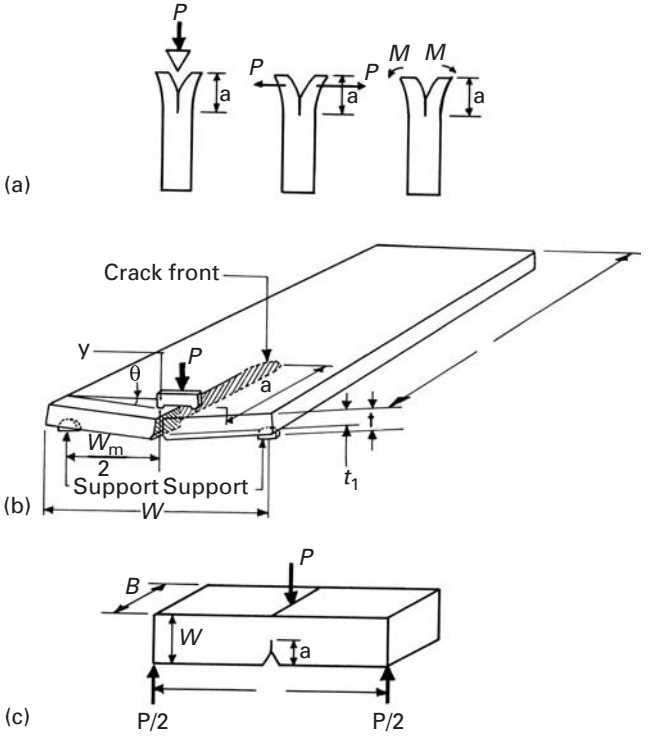

Fig. 9.20 Fracture-testing methods for brittle materials. (a) Double-cantilever beam (DCB). (b) Double torsion. (c) Notch flexure.

Therefore, the minimum thickness is very small, and microstructural inhomogeneities limit the size of the specimen. We next discuss the most common methods of testing brittle materials (Figure 9.20).

A double-cantilever specimen (DCB) with a precrack of size a is illustrated in Figure 9.20(a). Three possible loading configurations are shown: wedge loading, applied load P, and applied moment M. A groove is machined into the specimen to guide the propagation of the crack. The three loading methods provide essentially three relationships, between K_I, the stress intensity factor and the crack length.

A double-torsion specimen is very convenient for determining the fracture toughness of ceramics at high temperatures. It requires only the application of a compressive load P (Figure 9.20(b)). The stress intensity K_I does not depend on the length of the crack for $0.25\ L < a < 0.75\ L$. The fracture toughness is given by

$$K_I = P\,W_m \left[\frac{3}{W t^3 t_1\,(1-\nu)\,\xi}\right]^{1/2}, \tag{9.20}$$

where ξ is a geometrical factor that depends on the thickness of the specimen, t_1.

The notch bend test (Figure 9.20(c)) is analogous to the same test applied to metals. A notch is cut into the brittle material. A crack

"pops in" during loading and then grows with P. This technique requires only small specimens.

9.7.1 Chevron Notch Test

The main advantage of the chevron notch test is that the critical stress intensity factor can be determined from the maximum load without resorting to precracking and crack length measurement. The test requires that the specimen undergo stable crack growth before reaching the maximum load, as indicated by the load–displacement curve deviating slightly from the initial linear part before final fracture.

The notches in the samples can be conveniently made with a low-speed diamond saw. The dimensions of the specimen should obey the following guidelines, as recommended in various references:[5]

$$S/W = 4, \quad W/B = 1.5, \quad \alpha_0 = a_0/W \geq 0.3, \quad \text{and} \quad \theta = 60^\circ.$$

Here, S is the span, W is the height of the specimen, B is the width of the specimen, and θ is the included angle. Figure 9.21(a) shows a schematic of the test arrangement and the details of the notch plane. The test can be performed in a universal testing machine at a constant crosshead speed. The chevron tip length, a_0, can be measured from optical micrographs of broken specimens, as shown in Figure 9.21(b). The critical stress intensity factor can be obtained from the relationship

$$K_{Ic} = \frac{P_{\max}}{B\sqrt{W}} Y_c(\alpha_0),$$

where $P_{\max}$ is the maximum load, B is the width of the specimen, W is the height of the specimen, and Y_c is a dimensionless coefficient[6] given by

$$Y_c(\alpha_0) = 5.639 + 27.44\alpha_0 + 18.93\alpha_0^3 - 43.42\alpha_0^3 + 338.9\alpha_0^4$$

for the geometry of the specimen in this study (i.e., $\theta = 60^\circ$ and $W/B = 1.5$).

In another variant of the chevron test, the chevron-notched short-rod specimen shown in Figure 9.21(c) which has been standardized by ASTM (E1304–89), has a wedge inserted into a slit that is cut in it, leaving a thin layer of ceramic with a V-shape. A crack is initiated at the tip of the wedge; the width of the crack increases as the crack moves forward. The wedge also guides the crack as it grows. The load

[5] S.-X. Wu, *Eng. Fracture Mech.*, 19 (1984) 221.

[6] S.-X. Wu, *Chevron-Notched Specimens: Testing and Stress Analysis*, eds. J. H. Underwood, S. W. Freiman, and F. I. Baratta (Philadelphia: ASTM, 1984), p. 176.

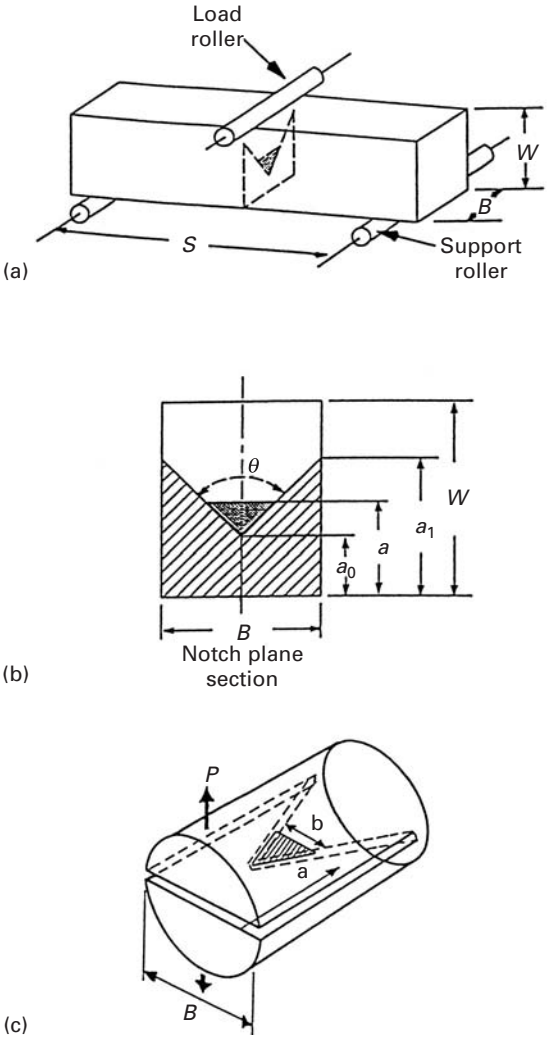

Fig. 9.21 Chevron notch test. (a) Schematic of the test arrangement and the details of the notch plane. (b) The chevron tip length, a_0, can be measured from optical micrographs of broken specimens. (c) Chevron short-rod specimen.

that opens the crack can be supplied by applying tension to the two sides or by an ingenious bladder mechanism. In this mechanism, a bag containing a fluid is inserted into the slit. The fluid is then pressurized, creating a crack opening force P. The fracture toughness of the specimen is determined from

$$K_{Ic} \approx 22 P_c B^{-3/2},$$

where P_c is the maximum load for crack propagation and B is the diameter of the short rod. This technique has also been extended to metals (with a different equation). This geometry of the specimen does not require any fatigue precracking; this is a considerable advantage, because fatigue precracking can be complicated and "tricky," especially in ceramics.

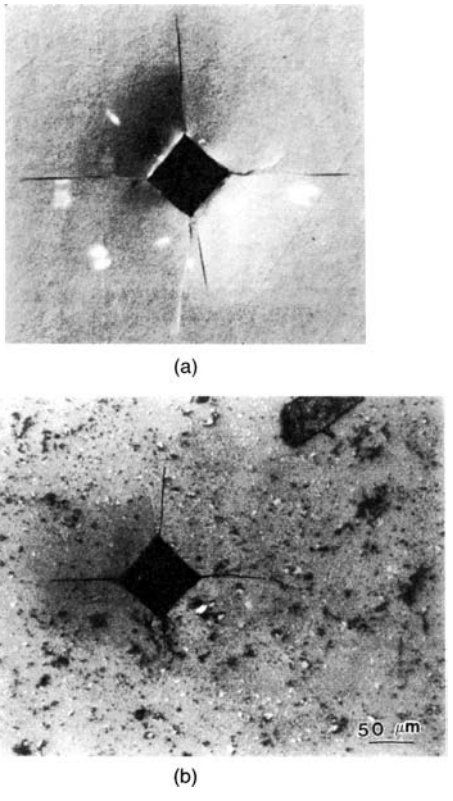

Fig. 9.22 Fractures produced by hardness indentations in (a) AsS_3 glass (courtesy of B. R. Lawn and B. J. Hockey) and (b) Al_2O_3.

9.7.2 Indentation Methods for Determining Toughness

Hardness indentations can generate cracks in brittle materials; two such examples are shown in Figure 9.22. Tensile stresses are generated under conical and pyramidal indentations. These tensile stresses can generate cracks, and the length of the cracks can be used to calculate a fracture toughness. A second use of such cracks is as initiation sites for fracture in the conventional bending test. The very attractive feature of these microhardness-induced cracks is that they are very small and on the same scale as cracks naturally occurring in ceramics (<1 mm).

Palmqvist was the first to recognize that indentation cracks could be used to obtain quantitative estimates of the fracture toughness of brittle materials.[7] Later, detailed studies by Lawn, Wilshaw, Evans, and coworkers laid the foundation for indentation fracture toughness tests.[8] A simple dimensional analysis shows that the hardness of a material (i.e., the material's resistance to plastic deformation) is given by

$$H = \frac{P}{\alpha c^2},$$

[7] S. Palmqvist, *Jernkontorets Ann*., 141 (1957) 300; *Arch. Eisenhuttenwies*., 33 (1962) 629.

[8] B. R. Lawn and T. R. Wilshaw, *J. Mater. Sci*., 10 (1975) 1049; A. G. Evans and T. R. Wilshaw, *Acta Met*., 24 (1976) 939; A. G. Evans and E. A. Charles, *J. Am. Cer. Soc*., 59 (1976) 371.

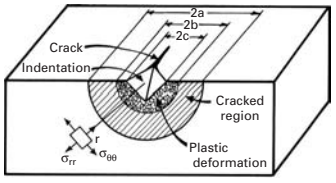

Fig. 9.23 Schematic representation of indentation generating a plastic deformation region and a semicircular crack.

where c is the diagonal of the impression and P is the load. The area of the impression is $0.5c^2$, setting the value of the parameter α to (1/1.854) for Vickers indentation. (See Section 3.8.1.) In a similar way, the toughness of the material is related to the load and crack size by

$$K_c = \frac{P}{\beta a^{3/2}}.$$

This gives the correct units for K_c: $\mathrm{Nm}^{-3/2}$ or $\mathrm{Pa\ m}^{1/2}$. The factor β incorporates a complex elasto–plastic interaction that will not be discussed here. It is important to emphasize that the crack is not always produced during the indentation period, but can be generated during unloading. There are elastic stresses caused by the indentation, producing compressive tangential components of stress; there is also plastic deformation, creating residual stresses on unloading. It is these residual stresses, with a tensile tangential component, that drive the crack. The problem can be analyzed as an internal cavity pressurized in an infinite body. This generates compressive radial stresses σ_{rr} and tensile tangential stresses $\sigma_{\theta\theta}$. The tangential stresses decay with $1/r^2$. On the other hand, a crack with length $2a$ forms, under ideal circumstances, a semicircle under the indentation, as shown in Figure 9.23. The residual stress intensity factor, in its turn, is given by

$$K_r = Y\sigma_{\theta\theta}\sqrt{\pi a}.$$

Since

$$\sigma_{\theta\theta} = \frac{kP}{a^2},$$

it follows that

$$K_r = \frac{kY\pi^{1/2}P}{a^{3/2}} = \frac{k'P}{a^{3/2}},$$

where k' is a parameter. It has been shown that the size of the indentation depends on the hardness of the material and on the Young's modulus E. The following functional relationship has been found:

$$k' = \delta\left(\frac{E}{H}\right)^{1/2},$$

where δ is a geometrical factor that depends on the indentation. Thus,

$$K_r = \delta\left(\frac{E}{H}\right)^{1/2}\frac{P}{a^{3/2}}$$

Anstis *et al.*[9] take $\delta = 0.016 \pm 0.004$ (for a Vickers indentation). The fracture toughness of the material is the residual stress intensity factor at which the crack stops growing. Hence,

$$\boxed{K_{Ic} = \delta\left(\frac{E}{H}\right)^{1/2}\frac{P}{a^{3/2}}.}$$

[9] G. R. Anstis, P. Chantikul, B. R. Lawn, and D. B. Marshall, *J. Am. Cer. Soc.*, 64 (1981) 533.

Sometimes, equilibrium conditions are not established until after the load is removed. Slow growth of the cracks can then take place, and the measurement of a depends on the time interval involved. Sometimes, no well-defined radial cracks are formed. In that case, the load P should be adjusted so that well-developed cracks are generated – that is, cracks for which $a > 2c$. Figure 9.24 compares conventional and indentation fracture toughnesses for a number of ceramics. The error bars show the variability of the measurements. It can be seen that the results agree within 30%. The great advantage of indentation fracture toughness tests over conventional tests is that comparative tests with various materials can be carried out readily, providing relative values.

A second manner in which indentation is used is to generate a "starter" crack for the three-point bending test. A Knoop indenter is preferred, and a sharp crack is generated at the center of the specimen and in the side opposite the one where P (the center load) is applied.

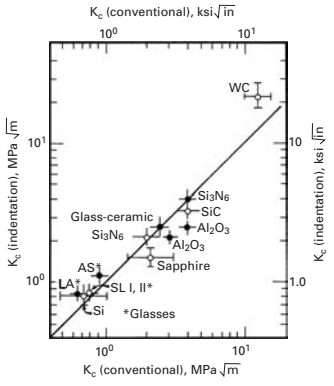

Fig. 9.24 Comparison between conventional and indentation fracture toughness determinations for glasses and ceramics. (From G. R. Anstis, P. Chankitul, B. R. Lawn, and D. B. Marshall, *J. Am. Cer. Soc.*, 64 (1981) 533.)

Example 9.4

Estimate the fracture toughness of the alumina specimen shown in Figure 9.22(b). The indentation was caused by a load of 10 kgf using a Vickers diamond indenter attached to a uniaxial testing machine. The alumina specification is AD 95.

Solution: We measure

$$2c = 14\,\text{mm},$$
$$2a = 36.5\,\text{mm}.$$

From the magnification marker, we establish the magnification: 160×. Thus,

$$2c = 0.087\,\text{mm},$$
$$2a = 0.228\,\text{mm},$$
$$P = 10\,\text{kgf} = 102\,\text{N},$$

and we have

$$K_r = 0.016\left(\frac{E}{H}\right)^{1/2}\frac{P}{a^{3/2}}.$$

From Table 2.8,

$$E = 365\,\text{GPa}.$$

H is the hardness in N/m^2. We have

$$H = \frac{10 \times 1.85}{7.6 \times 10^{-3}} = 2{,}434\,\text{kg/mm}^2$$
$$= 23.85\,\text{GPa}.$$

Also,

$$K_r = 0.016\left(\frac{365}{23.85}\right)^{1/2}\frac{10^2}{(0.114 \times 10^{-3})^{3/2}}$$
$$= 5.13\,\text{MPa m}^{1/2}.$$

9.8 Adhesion of Thin Films to Substrates

The reliability of many electronic components is dependent on the adherence of the thin film to the substrate. There are methods to determine the toughness of this adherence. The most common is the scratch test, in which an indenter is drawn over the thin films to different depths and the load is recorded. There is a depth at which the film detaches itself from the substrate. This is recognized by the load record, which shows a drop.

The indentation test is another alternative, providing quantitative estimates of the energy required to "peel off" the thin film from the substrate. There are two situations: (a) ductile film on brittle substrate; (b) brittle film on ductile substrate. The techniques used are slightly different. We describe the two methods below.

(a) Ductile film on brittle substrate. An indentation is made, typically with a micro or nanoindenter, in such a manner that it only penetrates the ductile thin film, pushing it aside as shown in Figure 9.25(a). The residual stresses caused by the deformed thin film cause delamination, once the indenter is removed, and if the deformation is sufficiently large. The diameter of the delam-

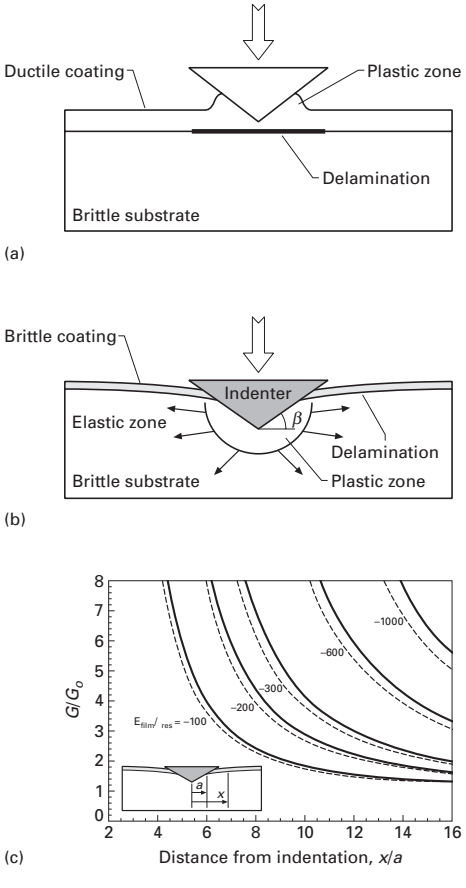

Fig. 9.25 Indentation tests for the determination of toughness of bond between substrate and thin film; (a) method used for ductile coating on brittle substrate (typical of electronic components); (b) method used for brittle coatings on ductile substrate; (c) calculated normalized energy release rate as a function of normalized crack diameter. (Adapted from J. J. Vlassak, M. D. Drory, and W. D. Nix, *J. Mater. Res.*, 12 (1997) 100.)

inated region can be related directly to the energy release rate for delamination.

(b) Brittle film on ductile substrate. This is the opposite situation. In this case, the analysis is quite different. We follow here the approach of Vlassak, Drory, and Nix.[10] Figure 9.25(b) shows the configuration used by them. The indenter is made to penetrate through the thin film, into the substrate, deforming it plastically. A crack of size x is formed along the interface. It is possible to determine the critical energy release rate by using the Vlassak–Drory–Nix analysis. Figure 9.25(c) shows the relationship between G/G_0 and the normalized crack diameter, x/a, for different values of $E_{\text{film}}/\sigma_{\text{res}}$. E_{film} is the Young's modulus of film and σ_{res} is the residual stress. G_0 is the energy release rate due to just the residual stress. It is given by:

$$G_0 = \frac{(1-\nu_{\text{film}}^2)}{2E_{\text{film}}}\sigma_{\text{res}}^2 t,$$

where t is the film thickness, and ν_{film} is Poisson's ratio of the film. σ_{res} has to be separately calculated or measured. This simple technique enables the determination of the toughness of the bond between substrate and film. An example is the toughness of the titanium–diamond interface. Vlassak, Drory, and Nix obtained a value of 51 J/m^2. Diamond coatings are used in many applications where a hard, wear-resistant surface is required.

Suggested Reading

T. L. Andersen. *Fracture Mechanics*, 2nd ed. Boca Raton, FL: CRC, 1995.

R. W. Hertzberg. *Deformation and Fracture Mechanics of Engineering Materials*, 4th ed. New York, NY: John Wiley, 1996.

B. Lawn. *Fracture of Brittle Solids*, 2nd ed. Cambridge, U.K.: Cambridge University Press, 1993.

S. T. Rolfe and J. M. Barsom. *Fracture and Fatigue Control in Structures*. Englewood Cliffs, NJ: Prentice-Hall, 1977.

Exercises

9.1 A Charpy machine with a hammer weighing 200 N has a 1-m-long arm. The initial height h_0 is equal to 1.2 m. The Charpy specimen, (see Figure 9.2), absorbs 80 J of energy in the fracturing process. Determine:

(a) The velocity of the hammer upon impact with the specimen.
(b) The velocity of the hammer after breaking the specimen.
(c) The average strain rate in the specimen.
(d) The final height attained by the hammer.

9.2 Estimate the fraction of cleavage area in the four specimens shown in Figure 9.3.

[10] J. J. Vlassak, M. D. Drory, and W. D. Nix, *J. Mater. Res.*, 12 (1997) 1900.

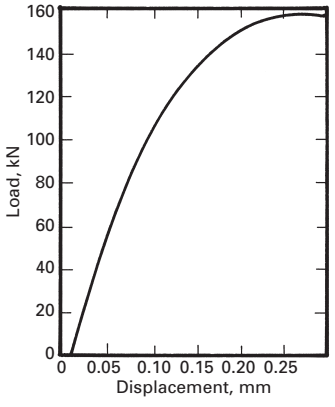

Fig. Ex9.5

9.3 Schematically show how the Charpy energy vs. temperature curve would be translated if the tests were carried at a low strain rate (approximately 10^{-2} s^{-1}).

9.4 If, instead of Charpy specimens with standard thickness equal to 10 mm, you were to test specimens with reduced thickness (e.g., 5 mm) and increased thickness (e.g., 30 mm) what changes would you expect in the Charpy energy value, normalized to the thickness of the specimen.

9.5 The load–displacement curve, obtained from a fracture toughness test on metal sample is shown in Figure Ex9.5. The dimensions etc. are as follows:

Crack length $a = 10$ mm,
Specimen thickness $B = 15$ mm,
Specimen width $W = 25$ mm,
Span $S = 50$ mm,
Yield stress, $\sigma_y = 300$ MPa.

Use the recommended procedure to determine the K_{Ic} from this curve. Check whether this is a valid K_{Ic} test.

9.6 A thermoplastic polymer has a plane-strain fracture toughness $K_{Ic} = 15$ MPa $m^{1/2}$ and a yield stress $\sigma_y = 80$ MPa. Estimate the requirements for dimensions of a fracture toughness specimen for this material.

9.7 Two samples of 0.45% C steel, one quenched and the other normalized, were tested for fracture toughness in a three-point bend test. The dimensions of the sample and the load–deflection curves for the two are shown in Figure Ex9.7 Determine K_{Ic} for the two samples, and establish whether the tests are valid. Verify whether the plane-strain conditions are met. Which steel would you expect to show a higher toughness? Does the result match your expectation?

Given:

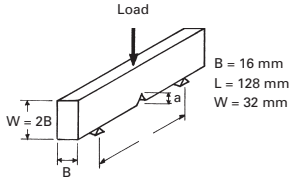

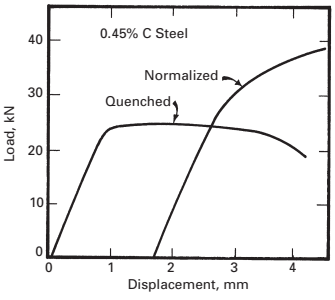

Fig. Ex9.7

	QUENCHED	NORMALIZED
	$\sigma_y = 1{,}050$ MN/m^2	$\sigma_y = 620$ MN/m^2
	$a_1 = 13.7$ mm	$a_1 = 9.3$ mm
Precrack	$a_2 = 11.6$ mm	$a_2 = 8.9$ mm
lengths:	$a_3 = 9.6$ mm	$a_3 = 9.4$ mm

9.8 A notched polymer specimen was tested for fracture toughness in a three-point bend test. The relevant dimensions of the specimen are:

Thickness $B = 5$ mm,
Width $W = 15$ mm,
Crack length $a = 1$ mm,
$S = 3.5W$

The load–deflection curve was linear until fracture occurred at 150 N. Compute K_{Ic} for this material.

9.9 A compact tension specimen of a polymer with the following dimensions was used in a fracture toughness test:

Thickness $B = 5$ mm,
Width $W = 50$ mm,
Crack length $a = 20$ mm.

Assuming a linear displacement curve to failure at a load of 200 N, compute K_{Ic} for this polymer.

9.10 A rectangular bar of ceramic 3 mm thick, 4 mm wide, and 60 mm long fractures in a four-point bend test at a load of 310 N. If the span of fixture is 50 mm, what is the flexure strength of the bar?

9.11 Norton NC-132 hot pressed Si_3N_4 has the following strengths for the given tests:

Three-point bending: 930 MPa,
Four-point bending: 720 MPa,
Uniaxial tension: 550 MPa.

Comment on the flaw sizes necessary to produce these failure stresses.

9.12 Calculate the tensile stresses generated by a load of 200 N acting on a specimen of SiC (a rectangular section of 5 mm height and 10 mm width) subjected to (a) three-point and (b) four-point bending. The span width is 50 mm and, for the four-point bending setup, the inner span is 25 mm. If the specimens are prenotched, with a notch depth of 1 mm, what are the stress intensity factors?

9.13 A cylindrical structural component with diameter 100 mm is subjected to a force of 100 kN at a distance of 500 mm from the clamp. The material used for the cylinder has a yield stress of 600 MPa. Will it yield plastically under the loading configuration shown in Figure Ex9.13? Use $I = \pi r^4/4$ for the moment of inertia of a cylindrical shaft.

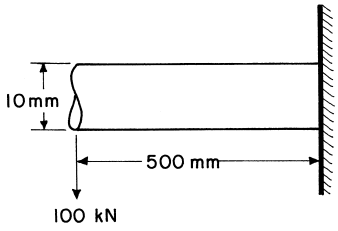

Fig. Ex9.13

9.14 In a sample of $MoSi_2$, an indentation made by a Vickers indenter gave the impression shown in Figure Ex9.14 under a load of 1 kN. Compute the hardness H of $MoSi_2$. Taking E for $MoSi_2$ to be 300 GPa, compute the fracture toughness of the sample.

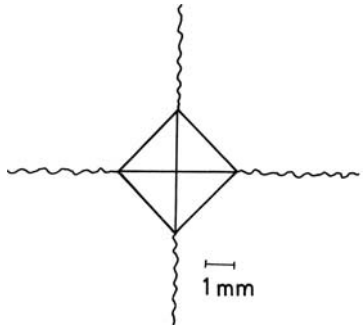

Fig. Ex9.14

9.15 Estimate the fracture toughness for AsS_3 glass shown in Figure 9.22a, knowing that the indentation was made with load $P = 10$ N. Young's modulus for this glass is $E = 75$ GPa. Assume same magnification for the two micrographs.

9.16 A chevron short-rod specimen with a diameter of 5 cm (Al_2O_3) was tested, and the critical load P_c was equal to 2,000 N. Determine the fracture toughness of the specimen.

9.17 Polymer specimens (PMMA (polymethyl methacrylate), PC (polycarbonate), and PP (polypropylene)) with the geometry shown in Figure Ex9.17 were tested.

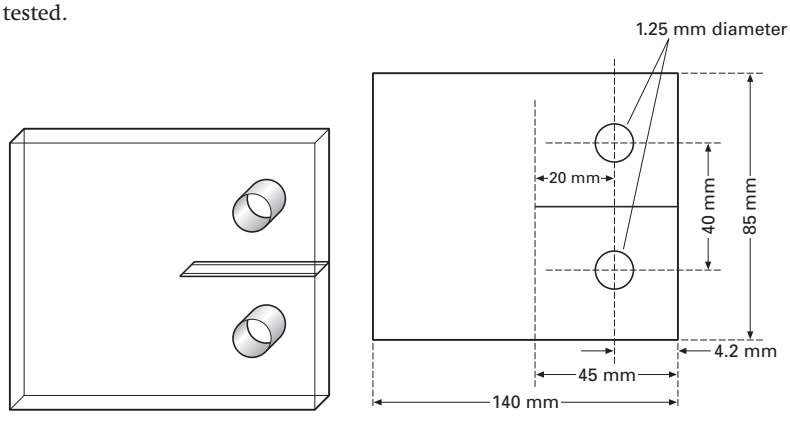

Fig. Ex9.17

The dimensions of specimens, crack, and load fracture for a number of tests are:

Test	Material	Crack Length, a (mm)	Width, W (mm)	Specimen thickness, B (mm)	Load, P (N)
1	PMMA	24.60	76.34	3.7	220.08
2	PMMA	24.80	75.88	5.92	421.00
3	PMMA	24.90	76.14	9.32	995.01
4	PMMA	23.88	76.24	11.54	1002.68
5	PMMA	13.52	76.18	11.38	1422.20
6	PMMA	19.72	76.14	11.63	1136.16
7	PMMA	37.86	76.24	11.58	621.80
8	PMMA	26.10	76.10	5.30	1184.15
9	PMMA	27.24	76.18	5.18	692.64
10	PMMA	27.72	76.20	5.32	1838.86
11	PMMA	28.68	76.16	5.84	1380.00
12	PC	25.04	76.10	5.82	2980.00
13	PP	24.28	76.14	6.36	1417.86

Calculate the fracture toughness for the specimens. Use the following equations:

$$K = \frac{P}{BW^{1/2}} f\,(a/W)$$

$$f(a/W) = \frac{[2 + (a/W)]}{[1 - (a/W)]^{3/2}} \left[0.886 + 4.64(a/W) - 13.32(a/W)^2 + 14.72(a/W)^3 - 5.6(A/W)^4\right].$$

9.18 A compact tension specimen is used for the determination of fracture toughness. When it is loaded, the crack ($a = 45$ mm) starts to propagate at an applied force of 10^5 N. The specimen thickness is $B = 60$ mm. The dimension W is equal to 90 mm. Is this test valid? In other words, do we have a state of plane strain? The yield stress of the material is 500 MPa.

9.19 After Charpy testing, what is the correlation between the energy absorbed and the appearance of the fracture surface? How does this relate to ductile and brittle materials?

9.20 List the advantages and disadvantages of the Charpy test, drop-weight test, instrumented Charpy impact test, and plane-strain fracture toughness test.

9.21 Estimate the minimum specimen thickness for a valid plane-strain fracture toughness test for a material having the following properties: yield stress, $\sigma_y = 600$ MPa; fracture toughness, $K_{Ic} = 150$ MPa $m^{1/2}$.

9.22 A structural aluminum plate (7075-T561, $K_{Ic} = 29$ MPa $m^{1/2}$), part of an engineering design, has to support 200 MPa under tension. Determine the largest crack size that this plate can sustain.

9.23 A test sample undergoes a crack opening displacement (COD) test. The thickness of the specimen is 7 mm, and the clip gage thickness is 0.6 mm.

The critical displacement, Δ_c, of the clip gage is experimentally determined to be 1.5 mm, and the crack length is 1.4 mm. Compute the opening displacement, δ_c.

9.24 In a four-point bend test, the specimen has a span of 70 mm and a load, P, of 80 N. The width and height are 6 mm each. Draw the moment and shear diagrams. Find the maximum moment and maximum stress.

9.25 A number of Charpy impact tests were conducted on steels containing different levels of Ni. The energy levels (in J/m^2) are given in the table below:

Test Temperature (°C)	0% Ni	2% Ni	5% Ni	8% Ni
–200	2	2	5	28
–150	3	5	30	35
–100	6	15	55	37
–50	15	55	70	47
0	60	80	75	60
50	75	85	80	65
100	75	85	85	67

(a) Plot the curves for the different alloys.
(b) Find the DBTT for each alloy.
(c) What can you conclude from your analysis?

Chapter 10

Solid Solution, Precipitation, and Dispersion Strengthening

10.1 Introduction

A *solution* can be defined as a homogeneous mixture of two or more substances. Generally, one thinks of a solution as liquid, but gaseous or solid forms are possible as well. Indeed, we can have solutions of gases in a gas, gases in a liquid, liquids in a liquid, solids in a liquid, and solids in a solid. A solution can have one or more solutes dissolved in a solvent. The *solute* is the substance that is dissolved; the *solvent* is the substance in which the solute is dissolved. In a solution, there is always less solute than solvent. There are two kinds of solid solutions: substitutional and interstitial. Figure 10.1 shows examples of each in a schematic manner. Figure 10.1(a) is of brass, which is a substitutional solid solution of zinc (the solute) in copper (the solvent). We call such an alloy substitutional because the solute atoms merely substitute for the solvent atoms in their normal positions. In a substitutional solution, the atomic sizes of the solute and solvent atoms are fairly close. The maximum size difference is approximately 15%. When the atomic sizes of the solute and solvent are very different, as in the case of carbon or nitrogen in iron, we get an interstitial solid solution. Figure 10.1(b) shows such a solid solution of carbon in iron. We call these solutions interstitial solid solutions because the solute atoms occupy interstitial positions in the solvent lattice.

In this chapter, we first focus our attention on the phenomenon of *solid solution* and the *strengthening* that can be obtained by this process. Simply put, the phenomenon can be regarded as one form of restricting dislocation motion in crystalline materials, especially metals. We then extend this idea to precipitation and dispersion strengthening. Precipitates can be formed in certain alloys in the solid state. One starts with a solid solution at a high temperature, quenches it to a low temperature, and then ages it at an intermediate temperature to obtain a finely distributed precipitate. During aging, precipitates appear in a variety of sequences, depending on the alloy system under consideration. *Precipitation strengthening* has to do with the interaction of dislocations with precipitates, rather than with single atoms

of solutes. A logical extension of this idea is to artificially disperse hard ceramic phases in a soft metallic matrix, instead of obtaining them via a precipitation process. The mobility of dislocations is then restricted by these hard particles, and the alloy is strengthened. This process is called *dispersion strengthening*.

10.2 Solid-Solution Strengthening

Dislocations are quite mobile in pure metals, and plastic deformation occurs by means of dislocation motion (i.e., by shear). A very versatile method of obtaining high strength levels in metals would be to restrict this rather easy motion of dislocations. We saw earlier that grain boundaries (Chapter 5) and stress fields of other dislocations (Chapter 6) can play this restrictive role at low temperatures and increase the strength of the material. When the dislocation mobility in a solid is restricted by the introduction of solute atoms, the resultant strengthening is called *solid-solution-hardening*, and the alloy is called a *solid solution*. An example of the strengthening that can be achieved by solid solution is shown in Figure 10.2(a), in which we plot the increase in yield stress of steel as a function of the content of the solute. Note that solutes such as carbon and nitrogen, which go into interstitial positions of the iron lattice, have much larger strengthening effects than substitutional atoms such as manganese. We shall explain this shortly. In order to analyze the phenomenon of hardening due to the presence of solute atoms, we must consider the increase in the stress necessary to move a dislocation in its slip plane in the presence of discrete barriers to the motion of dislocations. Conceptually, it is useful and easier to think in terms of an energy of interaction between the dislocation and the barrier (e.g., a solute atom or a precipitate). In the case of substitutional solutions, for a stationary dislocation, the interaction energy is the change in energy of the system consisting of a crystal and a dislocation when a solvent atom is removed and substituted with a solute atom. Knowing the interaction energy U, we can calculate the force dU/dx necessary to move a dislocation a distance dx normal to its length. In ceramics, solutes can also exercise a strengthening effect, as demonstrated by Figure 10.2(b) for monocrystalline alumina with additions of chromium. This increase manifests itself at high temperatures, where the ceramics become relatively ductile.

A dislocation has a stress field associated with it. (See Chapter 4.) Solute atoms, especially when their sizes are too large or too small in relation to the size of the host atom, are also centers of elastic strain. A solute atom is said to be a *point source* of dilation. A vacancy (i.e., a vacant lattice site) can also be considered a point source of (negative) dilation. Consequently, the stress fields from these sources (dislocations and point defects) can interact and mutually exert forces. Such an interaction due to size difference is called the *elastic misfit interaction* or *dilational misfit interaction*. Other types of interactions,

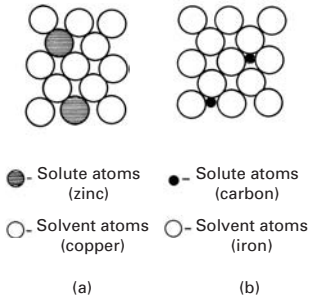

Fig. 10.1 The two basic forms of solid solutions. (a) Substitutional solid solution of zinc in copper to form brass. (b) Interstitial solid solution of carbon in iron to form steel. The interstitial solid-solution carbon atoms are shown in the face-centered cubic form of iron.

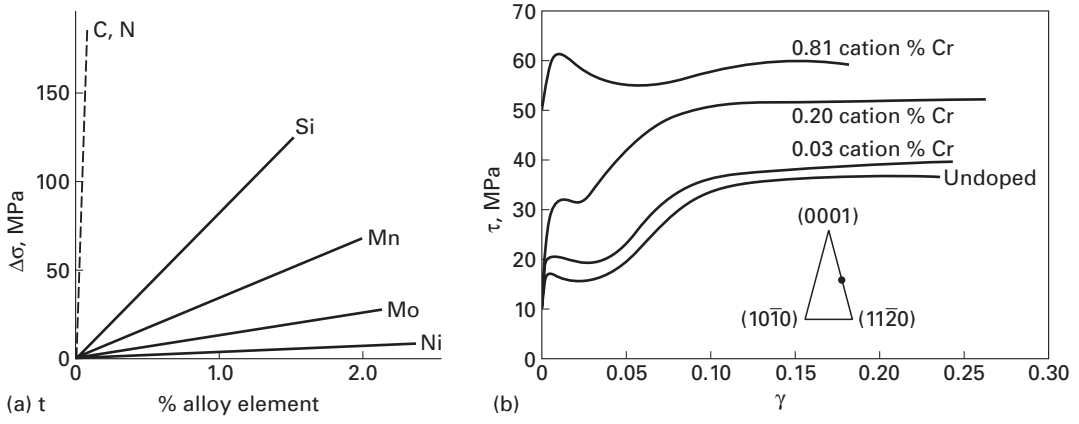

Fig. 10.2 (a) Increase in strength, $\Delta\sigma$, of steel as a function of content of solute. The solid lines represent substitutional solute additions, while the dashed line represents interstitial solute additions. (After F. B. Pickering and T. Gladman, ISI Special Report 81, Iron and Steel Inst., (London: 1963), p. 10). (b) Increase in strength of sapphire (monocrystalline alumina) with small additions of chromium at 1400 °C (Adapted from K. P. D. Lagerlof, B. J. Pletka, T. E. Mitchell, and A. H. Heuer, *Radiation Effects*, 74 (1983) 87.)

such as electrical and chemical elastic modulus mismatch, are also possible. Each of these interactions represents an energy barrier to dislocation motion.

10.2.1 Elastic Interaction

In the case of a positive edge dislocation, there is an extra half plane above the slip plane. Hence, there will be a compressive stress above the slip plane and a tensile stress under it (Chapter 4). Because a solute atom placed randomly in a crystal has a stress field around it, this stress field would be minimized if the solute atom were to move to the dislocation. For the case of an interstitial atom of carbon in iron, the minimum-energy position at an edge dislocation is the dilated region near the core. A substitutional atom that is smaller than the solvent atom will tend to move to the compressive side. On the other hand, if a solute atom is larger than the solvent atom, it will be expected to move to the tensile side. Substitutional atoms such as Zn in Cu give rise to a completely symmetrical spherical distortion in the lattice, which corresponds to the elastic misfit problem associated with inserting a ball in a bigger or smaller hole; that is, the substitutional solute atom acts as a point source of dilation of spherical symmetry. It is important to note that such spherically symmetric stress fields caused by substitutional impurity atoms can interact only with defects that have a hydrostatic component in their stress fields, as happens to be the case with an edge dislocation (see Equations 4.12a–c). Screw dislocations, by contrast, have a stress field of a pure shear character; that is, the hydrostatic component of a screw dislocation is zero (see Equations 4.11a and b). Therefore, to a first approximation, there is no interaction between screw dislocations and substitutional atoms, such as Zn in Cu or Mn in Fe. Interstitial atoms such as carbon or nitrogen in α-iron, however, not only produce a dilational misfit (in volume), but also induce a tetragonal distortion. Both carbon and nitrogen occupy interstitial positions at the face centers and/or the midpoints of the edges of the body-centered cubic structure (Figure 10.3). Carbon atoms occupy the midpoints of <001> edges. In Figure 10.3(a), we indicate the positions of the carbon atoms

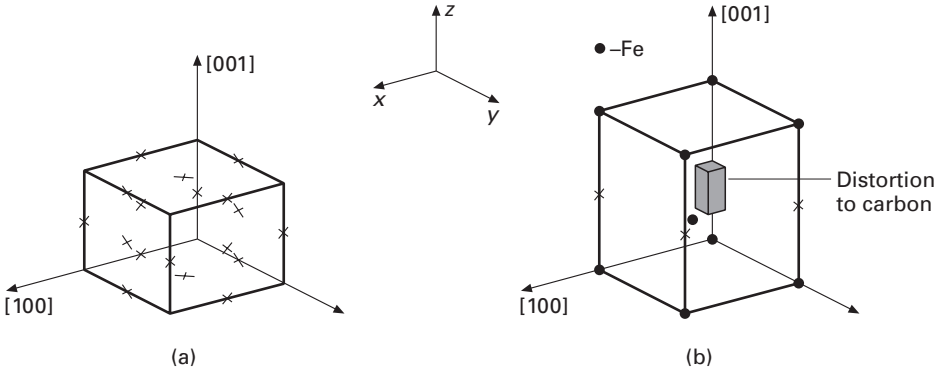

Fig. 10.3 (a) Positions of interstitial atoms in the cube. (b) Carbon atom shown as a producer of a tetragonal distortion.

by crosses. Figure 10.3(b) depicts the tetragonal distortion produced when a carbon atom moves to one of the cube edges of iron. The cubic shape changes to tetragonal, producing a tetragonal distortion along that particular <001> axis. Note that the figure shows the tetragonal distortion produced by a carbon atom in the iron cube; the carbon atom does not have an elongated form! The strain field attributed to this tetragonal distortion will interact with hydrostatic as well as shear stress fields. The important effect of the tetragonal distortion is that the interstitial atoms such as C and N in iron will interact and form atmospheres at both edge and screw dislocations and will lead to a more effective impediment to the movement of dislocations than in the case of substitutional atoms. (See Figure 10.2.)

We now derive an expression for the energy of interaction between an edge dislocation and a point source of expansion, such as an oversized (or undersized) solute atom. This was first done by Cottrell[1] and Bilby.[2] Let σ_ρ be the hydrostatic component of the stress field of a dislocation, and let ΔV be the change in volume induced by the introduction of a solute atom of radius $r_0\,(1+\varepsilon)$ in a cavity of radius r_0, where ε is positive. Then, for ε very small, we can write the change in volume as

$$\Delta V = \left(\frac{4}{3}\right)\pi r_0^3(1+\varepsilon)^3 - \frac{4}{3}\pi r_0^3 = \frac{4}{3}\pi r_0^3[(1+\varepsilon)^3 - 1],$$

so that

$$\Delta V \approx \frac{4}{3}\pi r_0^3\, 3\varepsilon,$$

or

$$\Delta V \approx 4\pi r_0^3 \varepsilon. \tag{10.1}$$

The stress field of an edge dislocation is given in rectangular coordinates in Chapter 4 (Equations 12a–c). In cylindrical coordinates, we

[1] A. H. Cottrell, in Proceedings of Conference on Strength of Solids, Physical Society, London, 1968, p. 30.
[2] B. A. Bilby, *Proc. Phys. Soc.*, A63 (1950) 191.

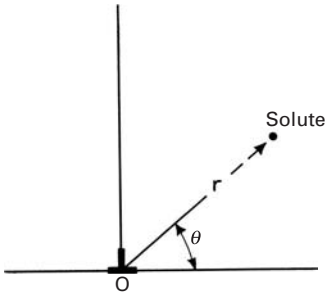

Fig. 10.4 (r, θ)-coordinates of a solute atom in the strain field of an edge dislocation.

have (the student can do this as an exercise):

$$\sigma_{rr} = \sigma_{\theta\theta} = -\frac{Gb}{2\pi(1-\nu)}\frac{\sin\theta}{r},$$
$$\sigma_{zz} = -\frac{\nu Gb}{\pi(1-\nu)}\frac{\sin\theta}{r},$$
$$\sigma_{r\theta} = -\frac{Gb}{2\pi(1-\nu)}\frac{\cos\theta}{r},$$
$$\sigma_{\theta z} = \sigma_{zr} = 0.$$

The hydrostatic pressure σ_p is, by definition, equal to $-1/3(\sigma_{rr} + \sigma_{\theta\theta} + \sigma_{zz})$. Thus, the hydrostatic stress associated with an edge dislocation, obtained from the preceding stress field, is

$$\sigma_p = \frac{1+\nu}{1-\nu}\frac{Gb}{3\pi}\frac{\sin\theta}{r}. \tag{10.2}$$

If we wish to convert this expression into rectangular coordinates, we need only use the relationship $r = (x^2 + y^2)^{1/2}$ and $\sin\theta = y/(x^2 + y^2)^{1/2}$.

The interaction energy (U_{int}) was defined by Eshelby[3] for a general ellipsoid of volume V in which both deviatoric and hydrostatic components of strain are generated and a general external stress field σ_{ij} as

$$U_{\text{int}} = V\sigma_{ij}(\varepsilon_{ij})_T,$$

where $(\varepsilon_{ij})_T$ is the strain tensor due to the transformation. For the simplified case of the solute atom, the stress is σ_p and the strain is ΔV per unit volume. We can calculate U_{int} in the following manner. Figure 10.4 shows the coordinates of a solute atom in the strain field of a dislocation. The elastic interaction energy due to misfit, U_{misfit}, for a solute atom at (r, θ) and at the dislocation origin (0, 0) can be obtained from Equations 10.1 and 10.2 as

$$U_{\text{misfit}} = \sigma_p\Delta V = \frac{1+\nu}{1-\nu}\frac{Gb}{3\pi}\frac{\sin\theta}{r}4\pi\varepsilon r_0^3 = A\frac{\sin\theta}{r}, \tag{10.3a}$$

where

$$A = \frac{4}{3}\frac{1+\nu}{1-\nu}Gb\varepsilon r_0^3.$$

The force exerted by the solute on the dislocation is

$$F = -\partial U_{\text{misfit}}/\partial r = A\sin\theta/r^2. \tag{10.3b}$$

Hence, solute atoms are attracted to dislocations and form what is called a "Cottrell atmosphere" around them, pinning them. This is especially true for interstitials, which tend to have a high mobility. Calculations similar to the foregoing can be carried out for interstitials that cause nonspherical distortions. Equation 10.3a is derived on the basis of linear elasticity theory; thus, it will not be valid at

[3] J. D. Eshelby, *Proc. Roy. Soc.*, A241 (1957) 376; A252 (1959) 561.

the dislocation core region, where linear elasticity does not apply. This is a great omission, as the binding energy will be a maximum precisely at the dislocation core. Therefore, the reader is forewarned that the interaction energy just determined is only an estimate. Consider again Equation 10.3a and Figure 10.4. The interaction energy U is positive in the region above the slip plane ($0 < \theta < \pi$) and is negative below the slip plane ($\pi < \theta < 2\pi$) for large solute atoms. This means that a solute atom larger in size than the matrix atom (i.e., ΔV positive) will be repelled by the compressive side of the edge dislocation and will be attracted by the tensile side, as the interaction energy will be negative there. For a solute atom of smaller size than the matrix atom (i.e., ΔV negative), the interaction energy will be negative in the upper part ($0 < \theta < \pi$) of the dislocation, and the solute will be attracted there. In both cases, solute atoms will migrate to the dislocation, which will result in a reduction in the free energy of the system.

It is possible to estimate the increase in stress required to move a dislocation from the number of solute atoms surrounding it. Let the maximum force $F_{\max}$ between a dislocation and a solute atom be given by Equation 10.3b. When r reaches a sufficiently low value, we have (from Peach–Koehler's equation, Equation 4.22c, Chapter 4)

$$\Delta\tau = F_{\max}/bL = A \sin\theta / r^2 bL,$$

where L is the spacing of solute atoms that "pin" a dislocation. A number of assumptions can be made to establish $F_{\max}$ and L. We shall make the very simple assumption that all solute atoms move to certain distance b from the dislocation. If C is the concentration of solute atoms per unit volume and ρ is the dislocation density (equal to the dislocation length per unit volume), then the spacing between solute atoms along a dislocation is

$$L = \rho / C.$$

Thus,

$$\Delta\tau = A \sin\theta \, C / r^2 b\rho.$$

If $r \approx b$ and $\sin\theta \approx 1$, we get

$$\Delta\tau = A \, C / b^3 \rho.$$

Figure 10.2 shows such dependence of change in yield stress on solute content. On the other hand, if the solute atoms form a rigid network in the lattice, the average spacing between solute atoms is

$$L' \approx C^{-1/3}.$$

The spacing L of solute atoms along the plane of a moving dislocation is determined by several factors, including the angle of bowing out of the dislocation between obstacles. The misfit interaction energy in such a case may be calculated by use of statistics.

The misfit energy for screw dislocations is given by

$$U_{\text{misfit}} = \varepsilon_{ij}\, \sigma_{ij}^{\text{screw}} \Omega,$$

where $\sigma_{ij}^{\text{screw}}$ represents the stress field associated with a screw dislocation and Ω is the specific volume given by $\Delta V = 3\Omega\varepsilon$, in which ε is the misfit parameter. The resultant force exerted by the interstitial atom on the dislocation has an equation similar to that in the case of a substitutional solute atom, but with the misfit parameter replaced by $(\varepsilon_{11} - \varepsilon_{22})/3$. A substitutional solute atom produces an isotropic strain field, i.e., $\varepsilon_{11} = \varepsilon_{22} = \varepsilon_{33}$, and it does not interact with a screw dislocation. However, for C in α-Fe, one has the extensional strain in the [100] direction, $\varepsilon_{11} = 0.38$, while the contractional strain along each of the two orthogonal directions, [010] and [001], is -0.026. Therefore, C in α-Fe hinders both edge and screw dislocations. It turns out that interstitial atoms with $(\varepsilon_{11} - \varepsilon_{22})$ as much as unity can show solubility in BCC metals. The reason for this is that metals can accommodate a greater uniaxial distortion than isotropic distortion by solute atoms, since the electron energy depends mainly on the specific volume.

10.2.2 Other Interactions

Besides the dilation and elastic misfit interactions there are other sources of dislocation–solute interactions: interactions due to a difference in modulus between the solute and the solvent, electrical interaction, chemical interaction, and local-order interaction due to the fact that a random atomic arrangement may not be the minimum-energy state in a solid solution. All these interactions will further hinder dislocation motion in a solid solution. Generally, however, their contributions are less important than the size effect described earlier.

10.3 Mechanical Effects Associated with Solid Solutions

Many important mechanical effects are associated with the phenomenon of solid solution. In the case of steels, solute-dislocation interaction leads to a migration of interstitial solute atoms to a dislocation, where they form an atmosphere around it. This solute atmosphere, called the *Cottrell atmosphere*, has the effect of locking-in the dislocation, making it necessary to apply more force to free the dislocation from the atmosphere. This results in the well-known phenomenon of a pronounced yield drop in annealed low-carbon steels. A word of caution is in order here. Temperature is an important variable in the migration of solute atoms to a dislocation. If the temperature is too low, the solute may not be able to diffuse to allow a redistribution of solute atoms to dislocations. Such a redistribution may be thermodynamically expected, but if the temperature is too low, it will not occur in a reasonable length of time. At very high

temperatures ($>0.5T_m$, where T_m is the melting point in kelvin), the mobility of foreign atoms will be much higher than that of dislocations, with the result that they will not restrict dislocation motion. In the range of temperatures where solute atoms and dislocations are about equally mobile, strong interactions with dislocations occur. The serrated stress–strain curve (or the Portevin–Le Chatelier effect) is another manifestation of this. We next describe some technologically important effects of solid-solution hardening.

Example 10.1

Why are substitutional solid solutions more common than interstitial solid solutions?

Solution: Substitutional solid solutions are more common than interstitial ones mainly because of the atomic size limitations. Substitutional solid solubility can be quite appreciable – up to a difference of 14% in the atomic diameters of two metals can be accomodated. Copper (atomic radius = 0.128 nm), for example, can dissolve up to about 35% of zinc (atomic radius = 0.1331 nm) atoms in a substitutional manner. Cu and Ni (atomic radius = 0.1246 nm) have complete miscibility, from 0 to 100%. In the case of interstitial solid solutions, a small atom (C, N, or H, for instance) has to lodge itself in the interstices of the solvent metal atoms. C in γ-Fe (FCC) has available larger sized interstices than it does in α-Fe (BCC), although there are more interstices available in the latter. This is the reason that C has a comparatively greater solubility in γ-Fe than in α-Fe. In general, however, the range of interstitial hole sizes available is not very large – hence, the less common occurrence of interstitial solid solutions.

10.3.1 Well-Defined Yield Point in the Stress–Strain Curves

A schematic stress–strain curve exhibiting a well-defined yield point is shown in Figure 10.5(a). Characteristically, annealed low-carbon steels show such stress–strain behavior. According to the theory of Cottrell and Bilby, the dislocations in annealed steels ($\rho \sim 10^7$ cm^{-2}) are locked–in by the interstitial solute atoms (carbon). When stress is applied to such a steel in a tensile test, it must exceed a certain critical value to unlock the dislocations. The stress necessary to move the dislocations is less than the stress required to unlock them – hence the phenomenon of a sharp yield drop and the appearance of an upper and lower yield point in the tensile stress–strain curve. Figure 10.5(b) shows how a steel containing 0.008% C reacts to one-hour aging treatments. The progressive formation of a yield point with a subsequent plateau is clearly seen After the dislocations have freed themselves from the Cottrell atmosphere, all the tensile curves in Figure 10.5(b) become identical. The solute atoms

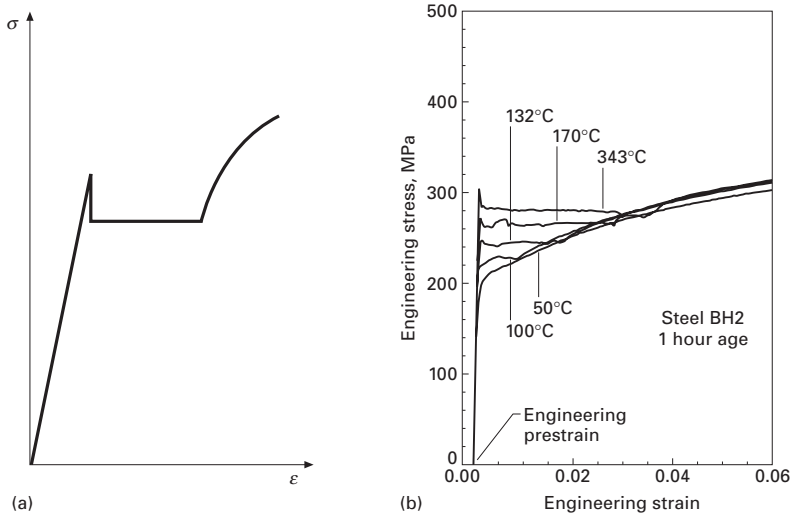

Fig. 10.5 (a) Schematic stress–strain curve of an annealed low-carbon steel showing the yield-point phenomenon. (b) Low-carbon steel in a temper-rolled condition and annealed for one hour between 100 °C and 343°C). (Courtesy of R. Foley.)

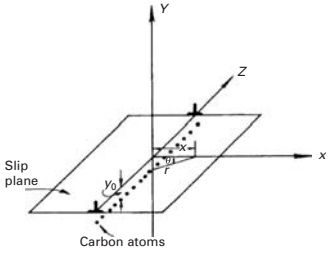

Fig. 10.6 Cottrell atmosphere in iron consisting of an edge dislocation and a row of carbon atoms.

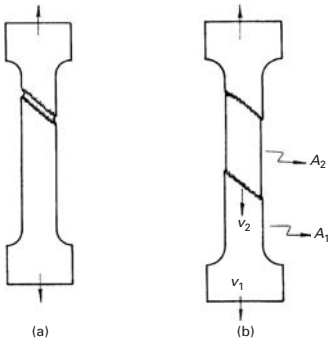

Fig. 10.7 Propagation of Lüders band in a tensile sample. v_1 and v_2 are the velocities of deformation of the specimen and the Lüders band, respectively.

segregate to the dislocations because this results in a decrease in the free energy. Given proper conditions for atomic diffusion, one would expect complete segregation of solute atoms to dislocations. Figure 10.6 shows schematically a Cottrell atmosphere of C atoms at a dislocation core in iron. In iron, atoms of carbon and nitrogen diffuse easily at ambient temperatures, but in many substitutional alloys one has to resort to treatments at higher temperatures.

10.3.2 Plateau in the Stress–Strain Curve and Lüders Band

After the load drop corresponding to the upper yield point, there follows a plateau region in which the stress fluctuates around a certain value. The elongation that occurs in this plateau is called the *yield-point elongation*. (See Figure 10.5.) It corresponds to a region of nonhomogeneous deformation. In a portion of the tensile sample where there is a stress concentration, a deformation band appears such as that indicated in Figure 10.7(a). As the material is deformed, this band propagates through the test sample. An intermediate position is indicated in Figure 10.7(b). The deformation is restricted to the interface. This deformation band is known as the *Lüders band*. In the plateau region of the stress–strain curve, there could be two or more such bands. Sometimes Lüders bands are visible to the naked eye. After the formation of the last band, the stress–strain curve resumes its normal trajectory of strain-hardening. Knowing the cross-sectional areas A_1 and A_2 in Figure 10.7(b), one can determine the number of Lüders bands from the yield-point elongation. One can also determine, from the strain rate of the sample, the speed of propagation of these bands. An aspect of great technological importance is the formation of Lüders bands during the stamping of low-carbon steels, with the consequent irregularities in the final thickness of the sheet (see Section 3.9.2). This problem is tackled, in practice, in two ways:

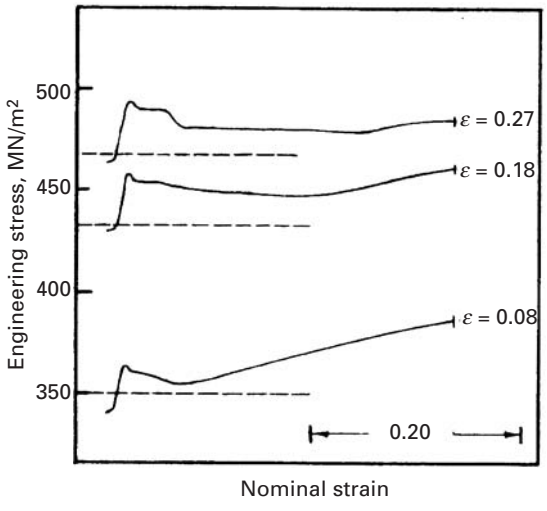

Fig. 10.8 Reloading curves after stopping a test for three hours at nominal strains of 0.08, 0.18, and 0.27. The dashed lines indicate the stresses at which the test was stopped. Note the formation of a well-defined yield point in the three cases (Reprinted with permission from M. A. Meyers and J. R. C. Guimarães, *Metalurgia – ABM*, 34 (1978) 707.)

1. By changing the composition of the alloy to eliminate the yield point. The addition of aluminum, vanadium, titanium, niobium, or boron to steel leads to the formation of carbides and nitrides as precipitates, which serve to remove the interstitial atoms from the solid solution.
2. By prestraining the sheet to a strain greater than the yield point strain such that the strains during the stamping operations occur in the strain-hardening region.

The explanation for the formation of Lüders bands is intimately related to the cause of the appearance of the well-defined yield point. The unlocking of dislocations that occurs at the upper yield point is, initially, a localized phenomenon. The unlocked dislocations move at a very high speed, because the stress required to unlock them is much higher than the stress required to move them, until they are stopped at grain boundaries. The stress concentration due to the dislocations that accumulate at grain boundaries unlocks the dislocations in the neighboring grains.

10.3.3 Strain Aging

As pointed out in the preceding sections, prestraining the steel to a strain greater than the yield strain will result in the removal of the yield point. However, if we let the sample rest before retesting, the yield point will return. This phenomenon is known as *strain aging*. Figure 10.8 shows the result of experiments done with an annealed austenitic alloy of composition Fe − 31% Ni − 0.1% C. The tensile test was stopped three times, each time for 3 hours, after three different strains: $\varepsilon = 0.08$, 0.18, and 0.27. The test was stopped simply by turning off the machine. Initially, the sample did not show a well-defined yield point. However, on reloading after the three-hour rest, the stress–strain curve showed clearly the appearance of a yield point followed by a plateau – i.e., a horizontal load-drop region – and, finally, a return to the original trajectory. The dashed lines indicate the

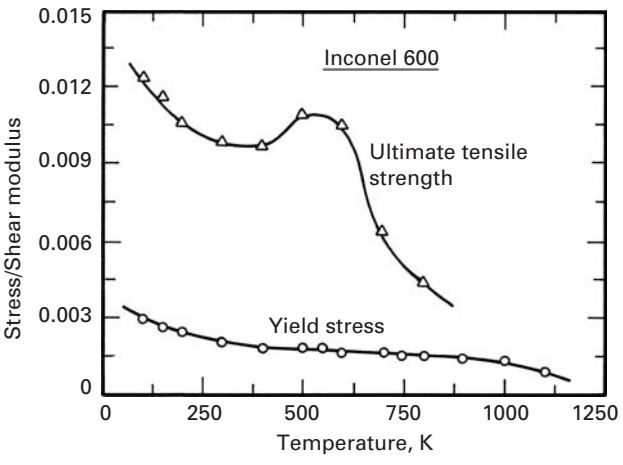

Fig. 10.9 Dependence of yield stress and ultimate tensile stress on temperature for Inconel 600, a nickel-based superalloy. The hump in the curve due to dynamic strain aging is usually evident only at large strains. (After R. A. Mulford and U. F. Kocks, *Acta Met.*, 27 (1979) 1125.)

values of stress at which the test was stopped. Note that, on reloading, the yield stress of the alloy increased for the three strains. The term "aging" is normally used when a precipitate forms. (See Section 10.4.) However, this is not the case in the example at hand. As the test was alternately carried out and interrupted at ambient temperature, interstitial atoms would migrate to dislocations during the interruptions, locking the dislocations. On reloading, the dislocations were unlocked, and a well-defined yield point appeared. The experiments were carried out under identical conditions, but keeping the test sample unloaded for three hours. The well-defined yield point reappeared, but it was less marked. The above experiment indicates that the applied stress has an accelerating effect on the strain-aging process. Generally, low-carbon steels show strain aging.

Another commonly observed effect due to strain aging is an enhancement of the work-hardening rate, leading to an increase in the ultimate tensile strength of the material. This effect is sometimes referred to as *dynamic strain aging*, because it occurs concurrently with plastic deformation. In some cases, the plot of flow stress vs. temperature shows a hump. The hump in the curve of ultimate tensile strength (UTS) vs. temperature for a nickel-based superalloy, Inconel 600, is shown in Figure 10.9. This hump is caused by solute atoms that have a mobility higher than the dislocations and that, therefore, can continue to "drag" them, leading to increased work-hardening. This enhanced work-hardening leads to a higher UTS. Note that the yield stress does not show such a hump.

10.3.4 Serrated Stress–Strain Curve

Under certain conditions, some metallic alloys show irregularities in their stress–strain curves that can be caused by the interaction of solute atoms with dislocations, by mechanical twinning, or by stress-assisted ("burst"-type) martensitic transformations. The first type (i.e., due to solute–dislocation interaction) has been called the *Portevin–Le Chatelier* effect. It generally occurs within a specific range of

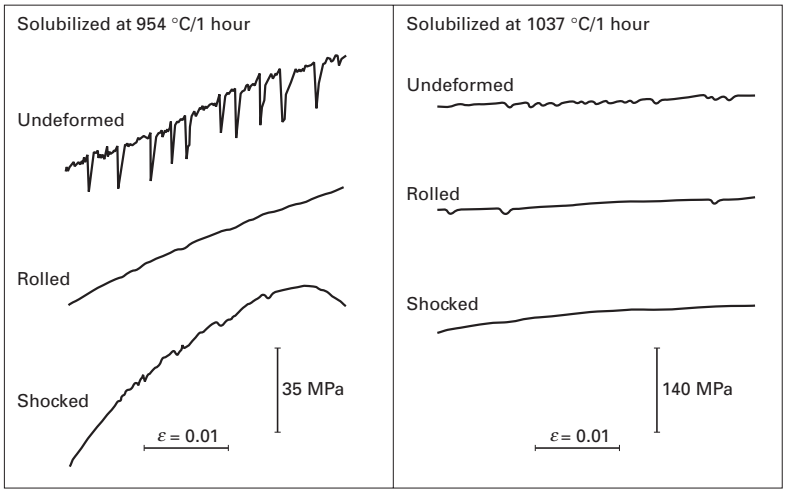

Fig. 10.10 Serrated flow observed in tensile test performed at 650 °C in Inconel 718 (a nickel–iron-based superalloy) solubilized at two temperatures. The undeformed, cold-rolled (19.1% reduction) and shock-loaded (51 GPa peak pressure) conditions are shown. (From M. A. Meyers, Ph.D. dissertation, 1974.)

temperatures and strain rates. The solute atoms, being able to diffuse through the test sample at a speed greater than the displacement speed of the dislocations (imposed by the applied strain rate), "chase" the dislocations, eventually locking them. With increasing load, the unlocking of dislocations causes a load drop with the formation of small irregularities in the stress–strain curve.

Irregularities in the stress–strain curves of a nickel–iron-based superalloy, Inconel 718, tested in tension at 650 °C after different processing schedules, are shown in Figure 10.10. Interactions between the solute atoms are more intense in the metal's undeformed condition. The stabilization treatment of 554 °C for one hour produced more pronounced load drops. The Portevin–Le Chatelier effect is dependent on the density of dislocations, strain rate, concentration and mobility of solute atoms, and other factors. The effect occurs in a region where there is inverse strain-rate sensitivity (i.e., if the strain is increased, the flow stress decreases). This relationship is attributed to the interplay between solute atoms and dislocations. Under normal conditions – that is, in the absence of solute – the flow stress increases with strain rate. In the Portevin–Le Chatelier regimen, an increase in strain rate frees the dislocations from the solute atoms.

10.3.5 Snoek Effect

Interstitial solute atoms such as carbon and nitrogen can, under the action of an applied stress, migrate in the α-Fe lattice. Such short-range migrations of C or N can result in an anelastic or internal friction effect, called the Snoek effect after the person who discovered it. As mentioned earlier, carbon or nitrogen atoms occupy the octahedral interstices located at the midpoints of the cube edges and at the centers of the cube faces. If we apply a stress along the z, or [001], direction, the octahedral interstices along the x- and y-axes will contract, while the ones in the z-direction will expand. Given the right time and temperature, the interstitial atoms will move to sites

along the *z*-axis. Such a change of site leads to a reduction in strain energy. On the other hand, a stress applied in the [111] direction will not result in a change of site, because all three of the cube's directions will be equally stressed and, on average, equally occupied by the carbon atoms. Such a movement of interstitials, when stress is applied along a cube direction and at levels less than the yield stress, can cause strain to lag behind stress; that is, the material will show the phenomenon of *internal friction*. The effect of this internal friction is commonly measured by a torsional pendulum. The angle of lag is called δ, and tan δ is taken as a measure of the internal friction. Mathematically,

$$\tan\delta = \frac{\text{log decrement}}{\pi} = Q^{-1},$$

where the logarithmic decrement is the ratio of successive amplitudes of the swing of the pendulum. If the amplitude decays to $1/n$ of its original value in time t, then

$$\tan\,\delta = Q^{-1} = \frac{\ln(1/n)}{\pi\nu t},$$

where ν is the vibrational frequency of the pendulum.

Only the interstitials that occupy the normal sites in an undistorted lattice will contribute to internal friction. Interstitials in the strain fields of a dislocation or a substitutional solute atom, or those at a grain boundary, will have their behavior altered. Thus, the Snoek effect can be used to measure C or N concentration in *high-purity* ferrite, i.e., BCC α-Fe. Would you expect to observe the Snoek effect in γ-Fe?

10.3.6 Blue Brittleness

Carbon steels heated in the temperature range of 230 and 370 °C show a notable reduction in elongation. This phenomenon is due to the interaction of dislocations in motion with the solute atoms (carbon or nitrogen) and is intimately connected with the Portevin–Le Chatelier effect. We classify it separately because of its distinct importance. When the temperature and the strain rate are such that the speed of the interstitial atoms is more than that of the dislocations, the dislocations are continually captured by the interstitials. This results in a very high strain-hardening rate and strength with a reduction in elongation. With increasing strain rates, the effect occurs at higher temperatures, as diffusivity increases with temperature. Called *blue brittleness*, this effect refers to the coloration that the steel acquires due to the oxide layer formed in the given temperature range. In the range of temperature and strain rate in which the material is subjected to dynamic aging, the strain-rate sensitivity is also affected, tending to increase linearly with temperature. However, in the presence of dynamic aging, the strain-rate sensitivity becomes very small, and the yield stress becomes practically independent of the strain rate.

10.4 Precipitation- and Dispersion-Hardening

Precipitation-hardening, or age-hardening, is a very versatile method of strengthening certain metallic alloys. Two important alloy systems that exploit this strengthening technique are aluminum alloys and nickel-based superalloys. Figure 10.11 shows examples of precipitates in some systems. Figure 10.11 (a) shows a typical example of an Al–Cu alloy, with θ ($CuAl_2$) precipitates at the grain boundaries and θ' (Cu_2Al) precipitates in the grain interiors, Figure 10.11(b) shows Al_3Li precipitates in an Al–Li alloy, and Figure 10.11(c) shows γ' (Ni_3Al)

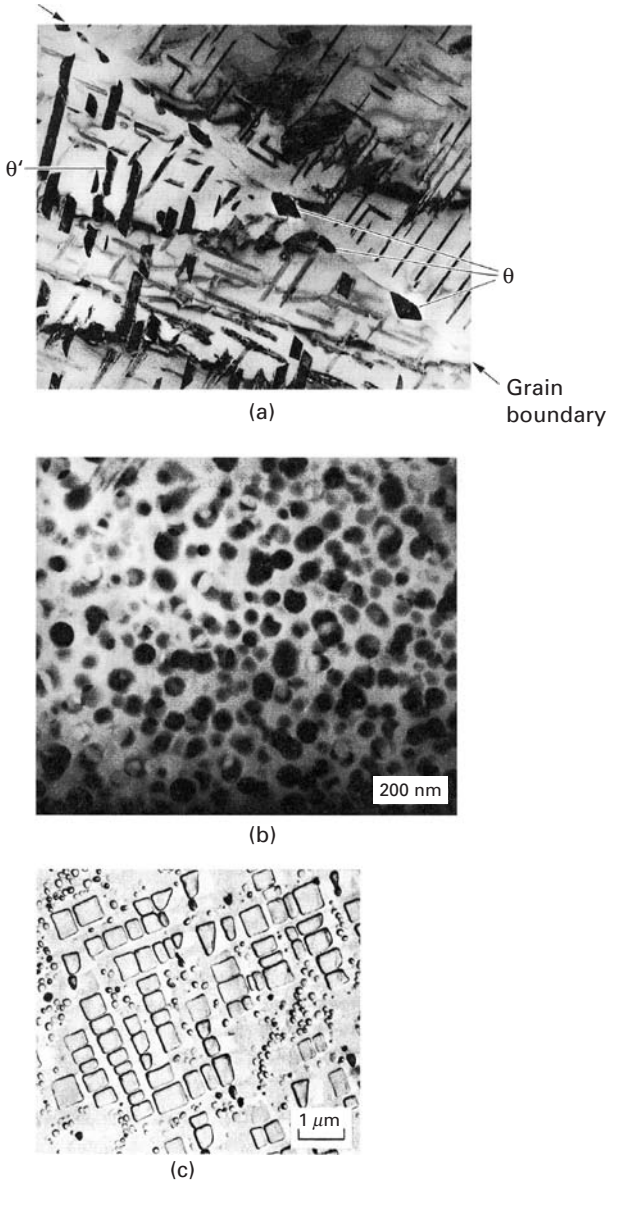

Fig. 10.11 (a) θ precipitates (at grain boundaries) and θ' precipitates (in grain interior) in Al–Cu alloy. (Courtesy of K. S. Vecchio.) (b) Al_3Li precipitates in Al–Li alloy (TEM, dark field). (Courtesy of K. S. Vecchio.) (c) γ' precipitates and aged carbides in a superalloy. (Courtesy of R. N. Orava.)

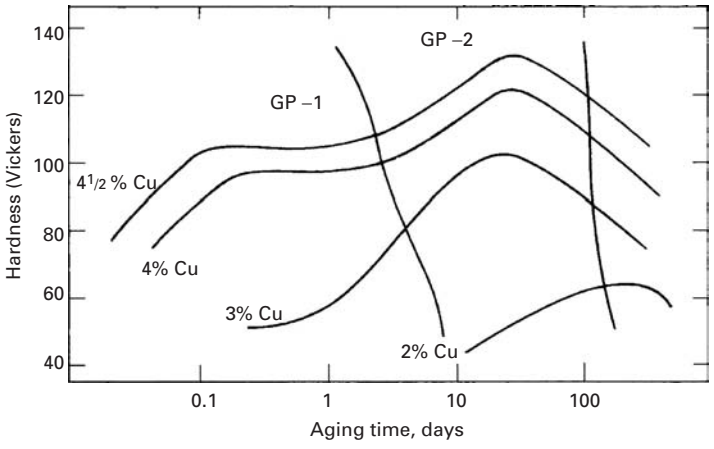

Fig. 10.12 Change in hardness with time of various Al–Cu alloys aged at 130 °C. (Adapted with permission from H. K. Hardy and T. J. Heal, *Prog. Metal Phy.*, 5 (1954) 195.)

precipitates and aged carbides in a nickel-based superalloy. The aging treatment involves the precipitation of a series of metastable and stable precipitates out of a homogeneous, supersaturated solid solution. Various metastable structures offer different levels of resistance to dislocation motion. Figure 10.12 shows the variation in hardness with aging time in the aluminum–copper system. Also shown are the different types of precipitate that occur during the aging treatment. Peak hardness or strength corresponds to a critical distribution of coherent or semicoherent precipitates.

In dispersion-hardening, we incorporate hard, insoluble second phases in a soft metallic matrix. Here, it is important to distinguish dispersion-strengthened metals from particle-reinforced metallic composites. The volume fraction of dispersoids in dispersion-strengthened metals is generally low, 3–4% maximum. The idea is to use these small, but hard, particles as obstacles to dislocation motion in the metal and thus strengthen the metal or alloy without affecting its stiffness is any significant way. In the case of metallic particulate composites, the objective is to make use of the high stiffness of particles such as alumina to produce a composite that is stiffer than the metal alone. Improvements in strength, especially at high temperatures, also result, but at the expense of ductility and toughness. Examples of dispersion-strengthened systems include Al_2O_3 in Al or Cu, ThO_2 in Ni, and more. TD Nickel is the name of an oxide-dispersion-strengthened nickel. Very small spherical particles (20–30 nm in diameter) of thorium dioxide (ThO_2) are dispersed in nickel matrix by powder metallurgical processing. Dispersion-strengthened copper is made by an internal oxidation technique. An alloy of copper and a small amount of aluminum is melted and atomized into a fine powder. Heating the powder under oxidizing conditions leads to an in situ conversion of aluminum into alumina. Any excess oxygen in the copper is removed by heating the powder in a reducing atmosphere. The powder is then consolidated, followed by conventional metalworking. We give some examples of dispersion-hardened systems later in this chapter. Suffice it here merely to point out

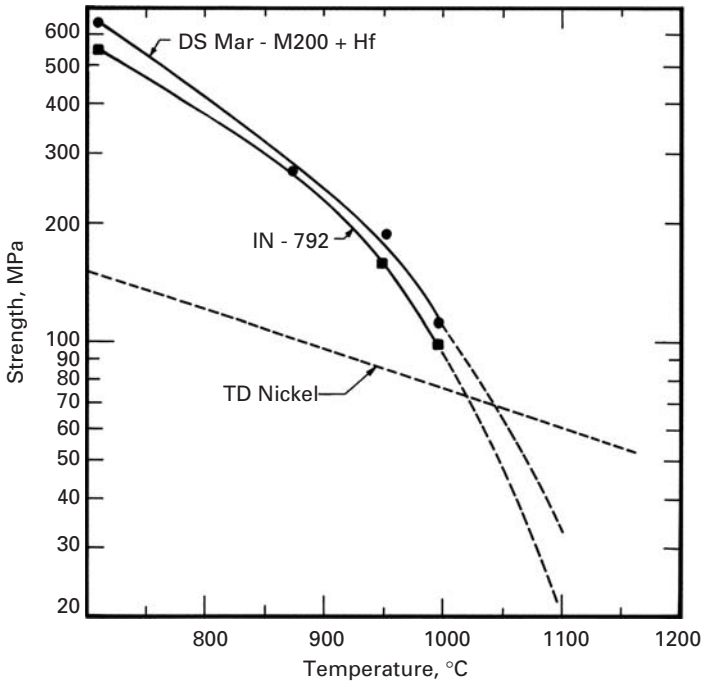

Fig. 10.13 Comparison of yield strength of dispersion-hardened thoria-dispersed (TD) nickel with two nickel-based superalloys strengthened by precipitates (IN-792) and directionally solidified (DS) MAR M 200.

that dispersion-hardened systems have one great advantage over those hardened by precipitation, viz., the stability of the dispersoids. Thus, dispersion-hardened systems maintain high strength at high temperatures, at which precipitates tend to dissolve in the matrix. Figure 10.13 illustrates the differences between strengthening by precipitation and by dispersion-hardening. Nickel-based superalloys IN792 and MAR M-200 are precipitation-hardened by γ'' or γ' precipitates having compositions of Ni_3Nb and Ni_3Al, respectively. The TD nickel, on the other hand, contains a fine dispersion of ThO_2, a high-melting-point oxide that is insoluble in the matrix. At lower temperatures (up to 1,000 °C), precipitation hardening is more effective; however, at approximately 1,100 °C, the precipitates dissolve in the matrix and the strength is drastically reduced. The dispersoids continue to be effective strengtheners at still higher temperatures.

The strengthening in these systems, hardened by either precipitates or dispersoids, has its origin in the interaction of dislocations with the particles. In general, the interaction depends on the dimensions, strength, spacing, and amount of the precipitate. The detailed behavior, of course, differs from system to system. Let us first describe the phenomenon of precipitation-, or age-, hardening. The supersaturated solid solution is obtained by sudden cooling from a sufficiently high temperature at which the alloy has a single phase. The heat treatment that causes precipitation of the solute is called *aging*. The process may be applied to a number of alloy systems. Although the specific behavior varies with the alloy, the alloy must, at least:

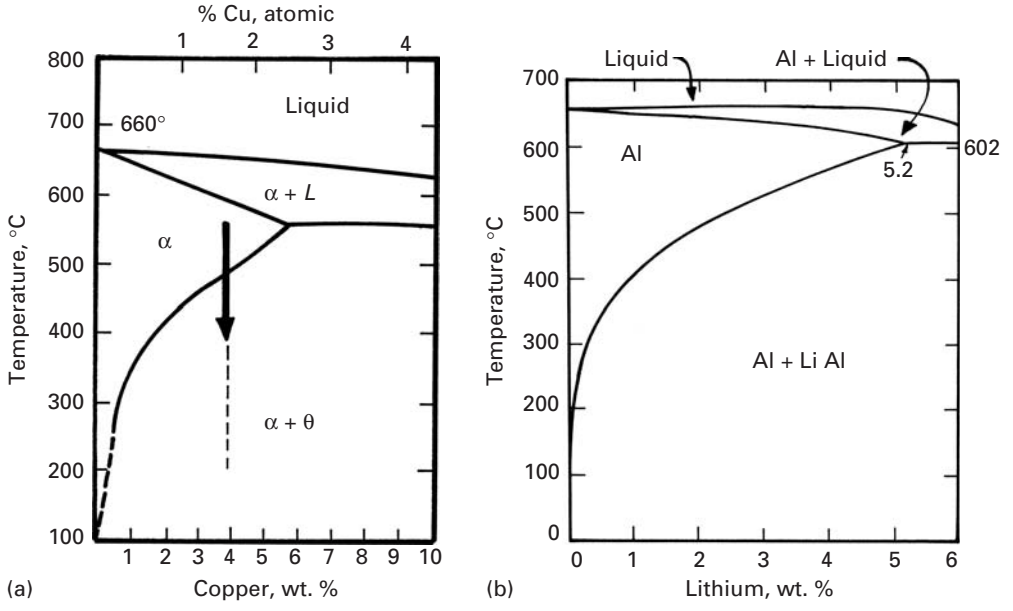

Fig. 10.14 (a) Phase diagram of the Al-rich end of the Al–Cu system. (b) Phase diagram of the Al-rich end of Al–Li system.

1. Form a monophase solid solution at high temperatures.
2. Reject a finely dispersed precipitate during aging, i.e., the phase diagram must show a declining solvus line.[4]

Figure 10.14(a) shows a part of the phase diagram of the Al–Cu system in which precipitation-hardening can occur, while Figure 10.14(b) shows the phase diagram of the Al–Li system. Lithium is interesting in that its addition to aluminum results in a lowering of the density, as well as a substantial increase in the modulus of the alloy. Both of the systems shown in Figure 10.14 fulfill the prerequisites for precipitation-hardening to occur. The precipitation treatment consists of the following steps:

1. *Solubilization*. This involves heating the alloy to the monophase region and maintaining it there for a sufficiently long time to dissolve any soluble precipitates.
2. *Quenching*. This involves cooling the single-phase alloy very rapidly to room temperature or lower so that the formation of stable precipitates is avoided. Thus, one obtains a supersaturated solid solution.
3. *Aging*. This treatment consists of leaving the supersaturated solid solution at room temperature or at a slightly higher temperature. It results in the appearance of fine-scale precipitates.

Table 10.1 presents some precipitation-hardening systems, with the precipitation sequence and the equilibrium precipitates. Although the behavior of different systems varies in detail, one may write the

[4] The solvus line is the locus of points representing the limit of solid solubility as a function of temperature.